KEK-ES171 Internal Report:

Reanalysis of photon detection inefficiencies for the KEK-CsI and 1mm-Pb/3mm-Scinti calorimeters.

H. Watanabe *
Department of Physics, Saga University

Abstract

The analysis of the KEK-CsI and 1mm-Pb/3mm-Scinti calorimeters using 2 neutron method is reported with several comments on the publication.

1 Neutron identification

Neutron identification is a most important part of our experiment. We make use of the difference in the pulse shape between neutrons and photons. Neutrons produce slower component of the scintillation pulses than photons in the liquid scintillators(LS). We use the dual gate, a wide(200nsec) and a narrow(35nsec) gate, in order to collect a total component and a fast component of the scintillation pulses. K. Mori introduced the "AUN" method to discriminate neutrons and photons using the LS energy information and applied the method to the analysis of the KTeV-CsI and 1mm-Pb/5mm-Scinti calorimeters[2][3]. In the case of the KEK-CsI and 1mm-Pb/3mm-Scinti calorimeter, a simple method to discriminate neutrons and photons was applied[1]. Then we have tried a consistent analysis for all samples using the same method of "AUN" for publication. Figure 1 shows the AUN distribution for the 1mm-Pb/3mm-Scinti calorimeter in tail region(Esample/Eγ <0.5).

Timing information is also effective to discriminate neutrons and photons. Figure 2 shows the "time-of-flight(TOF)" for the 1mm-Pb/3mm-Scinti calorimeter in the 750 MeV run.

Figure 3 shows the scatter plots of the AUN and TOF for the 1mm-Pb/3mm-Scinti calorimeter in the 750 MeV run. Neutrons and photons are clearly separated by the AUN and TOF method. The region for neutrons is shown by a box in Figure 3.

- $3\sigma_\gamma <$ AUN $< 2\sigma_{neutron}$.
- $4\sigma_\gamma <$ TOF $< 2\sigma_{neutron}$.

*electric address: nabe@hep.phys.saga-u.ac.jp

2 Neutron detection efficiency

The neutron detection efficiency, η_{LS}, is estimated from the multiplicity(m_{LS}) distribution of neutron hits in liquid scintillators(LS). The multiplicity more than two($m_{LS} \geq 2$) is used for a fitting by a Poisson distribution as shown in Figures 4, 5, 6 and 7. The zero and one multiplicity are estimated from the fit by a Poisson distribution. The E_γ dependence of the mean value(μ) of a Poisson distribution are shown in Figures 8 and 9. In these figures the μ obtained from the fit using the $m_{LS} \geq 1$ data are also plotted as reference. They are consistent with each other, but the error for the $m_{LS} \geq 2$ are larger than those for the $m_{LS} \geq 1$ especially at the low energy.

For the $m_{LS} \geq 2$, η_{LS} is given as $1 - exp(-\mu) - \mu \cdot exp(-\mu)$, and for the $m_{LS} \geq 1$ it is given as $1 - exp(-\mu)$ where the μ is the mean value of a Poisson distribution.

3 The photon detection inefficiency

The event of the small energy deposit below thresholds, 1 MeV, 3 MeV, 5 MeV, 10 MeV and 30 MeV in the calorimeters is taken as inefficient-event.

The inefficiency due to the photonuclear interaction is calculated as a ratio between the number of events below thresholds with a requirement of $m_{LS} \geq 1$ or $m_{LS} \geq 2$;

$$Ineff = \frac{N(E_{sample} < Threshold)}{N(all)} \cdot \frac{1}{\eta_{LS}}. \tag{1}$$

where η_{LS} is the neutron detection efficiency. Figures 10 and 12 show the detection inefficiency in the case of $m_{LS} \geq 2$ for the 1mm-Pb/3mm-Scinti and KEK-CsI calorimeter in a 40 MeV-bin for E_γ. The same data plotted in a 80 MeV-bin is shown in Figures 11 and 13.

Figures 14 and 15 are the detection inefficiency with a requirement of $m_{LS} \geq 1$. The comparisons of inefficiencies with each conditions are shown in Figures 16, 17, 18, 19, 20, 21, 22, 23, 24 and 25.

4 Check the result

The E_{sample}/E_γ dependence of μ are examined and found that μ is not significantly dependent on E_{sample}/E_γ within error in shown as Figures 26, 28, 30 and 32 for the $m_{LS} \geq 2$, and Figures 27, 29, 31 and 33 for the $m_{LS} \geq 1$.

We take a ratio between a number of events in region of E_{sample}/E_γ below 0.1∼0.6 with the $m_{LS} \geq 1$ or $m_{LS} \geq 2$ to that of all the tagged events(tail-to-total ratio). Figures 34 and 36 show the E_γ dependence of the tail-to-total ratio with the $m_{LS} \geq 1$ by the η_{LS}, and Figures 35 and 37 show that for the $m_{LS} \geq 2$. Figures 38 and 39 show that for the $m_{LS} \geq 1$ in the log scale.

The curve in figures represents a ratio between the cross sections of the photonuclear interaction and the electromagnetic shower process for the KEK-CsI calorimeter. The tail-to-total ratio has same tendency as a ratio of cross section, but no bump for the second nucleon resonance is observed. It notes that the number of tail events below 240 MeV is suppressed by a trigger as shown in Figures 40, 41, 42 and 43.

5 Comments on further analysis of other samples

Figures 44, 45, 46 and 47 show the distribution of the sample energy deposit in both case of the $m_{LS} \geq 2$ and $m_{LS} \geq 1$ for comparison, and Figures 48, 49, 50, 51, 52, 53, 54 and 55 show them in the energy-deposit region below 10 MeV. As seen in Figures, the $m_{LS} \geq 1$ has the background in the high energy region, but in the low energy region it is not clear. The background at the higher energy can be suppress with the $m_{LS} \geq 2$(2 neutron method). However, a problem of 2 neutron method is the large error of μ in the energy region below 400 MeV where the multiplicity is very small.

After a discussion with Takao Inagaki, we would like to make following recommendations for further analysis of other samples.

(1) It seems to be better that the inefficiency should be calculated in the condition of $m_{LS} \geq 1$ for the 430 MeV run and $m_{LS} \geq 2$ for the other runs and that the bin width for the 1100 MeV run should be taken to be 80 MeV.

(2) The E_γ dependences of μ(Fig. 8 and 9) and of the tail/total (Fig. 34 and 36) are very important to justify our samples selected as photonuclear interaction. Since the largest sample of data are those of the KTeV-CsI and 1mm-Pb/5mm-Scinti, similar plots for them are very desirable.

Of course, the background estimation which has been done by Tkashi Nakano based on Ref. [4] is crucial.

Inefficiencies calculated with the principle of the recommendation 1 are shown in Figures 56, 57, 58, 59, 60, 61, 62, 63, 64 and 65.

References

[1] H. Watanabe, Master thesis (1999)

[2] K. Mori, Master thesis (1999)

[3] K. Kurebayashi, Master thesis (1999)

[4] T. Matsumura, Master thesis (1999)

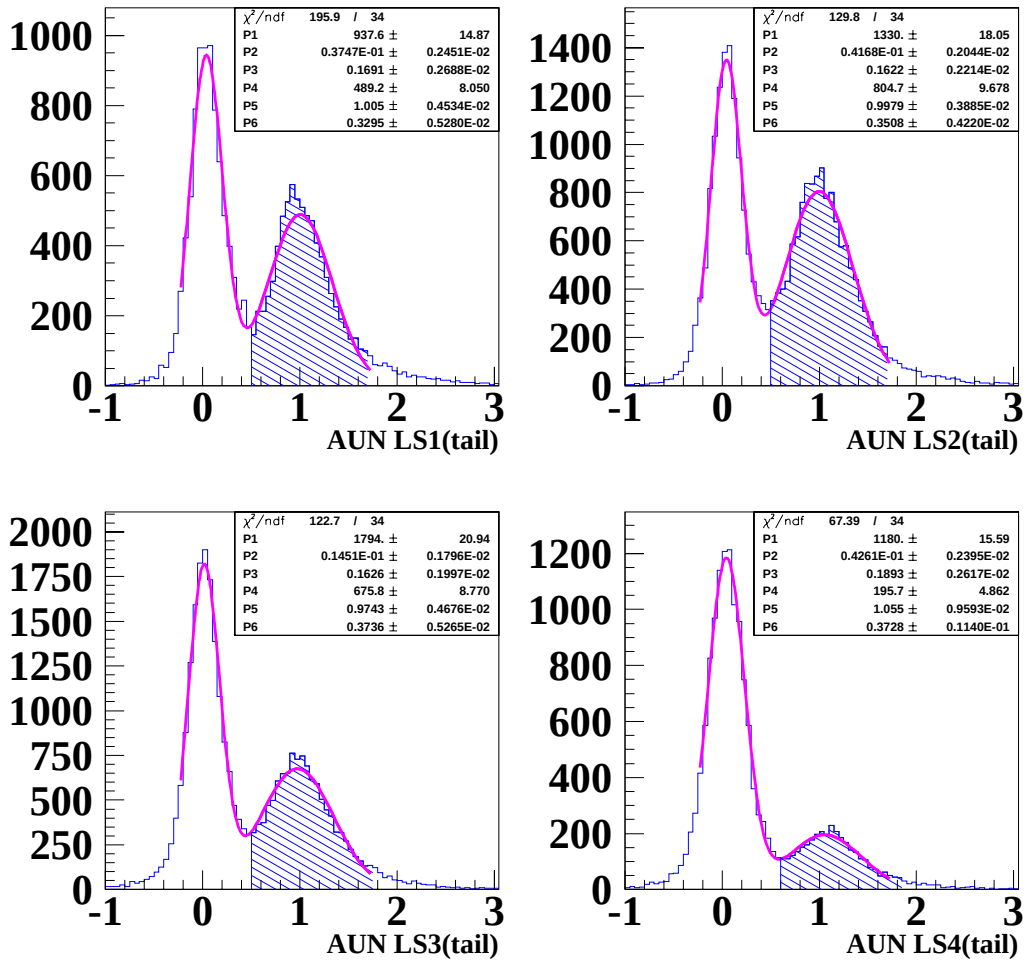

Figure 1: The AUN distribution for the 1mm-Pb/3mm-Scinti calorimeter in 750 MeV. Neutrons and photons are clearly separated by The AUN method. A diagonal part are a region for neutrons, $3\sigma_\gamma < AUN < 2\sigma_{neutron}$. The conditions of cut are determined by the fit with a double Gaussian.

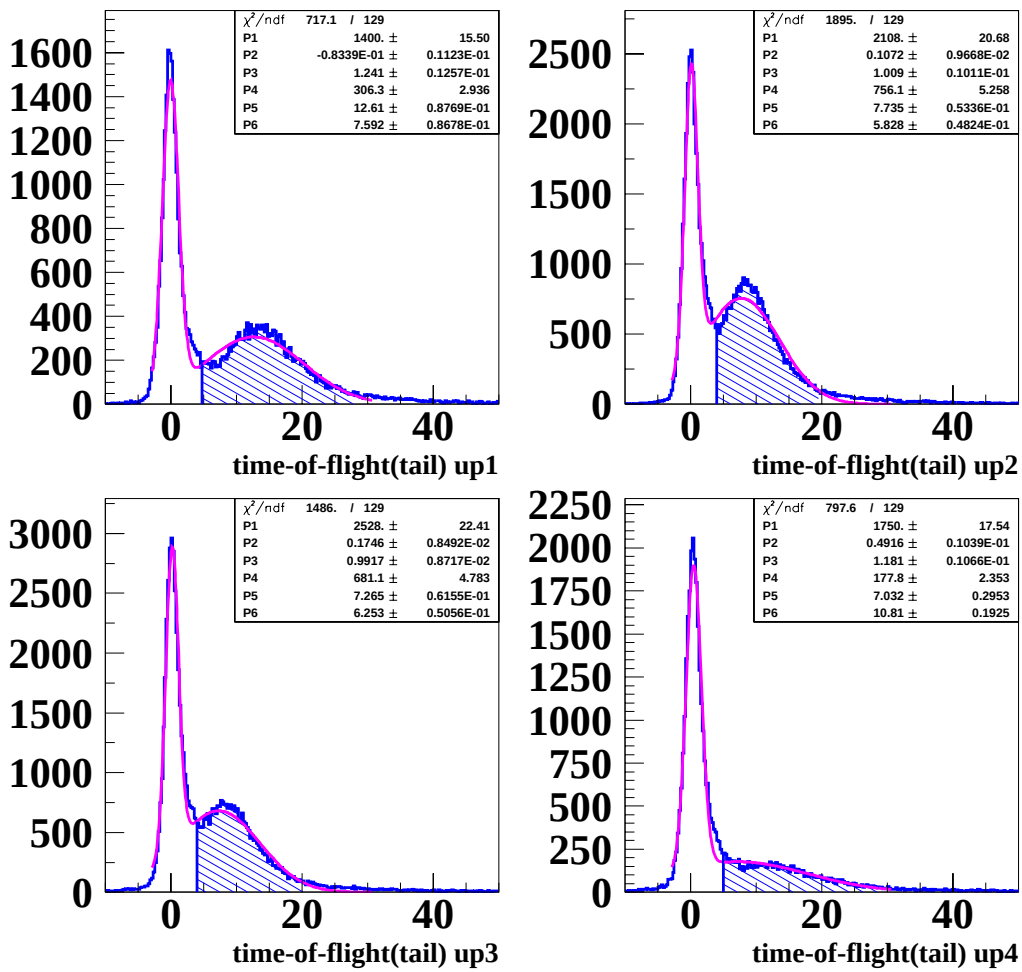

Figure 2: The Time of flight(TOF) distributions for the 1mm-Pb/3mm-Scinti calorimeter in the 750 MeV run. Neutrons and photons are clearly separated by The TOF method. A diagonal part is a region for neutrons, $4\sigma_\gamma < TOF < 2\sigma_{neutron}$.

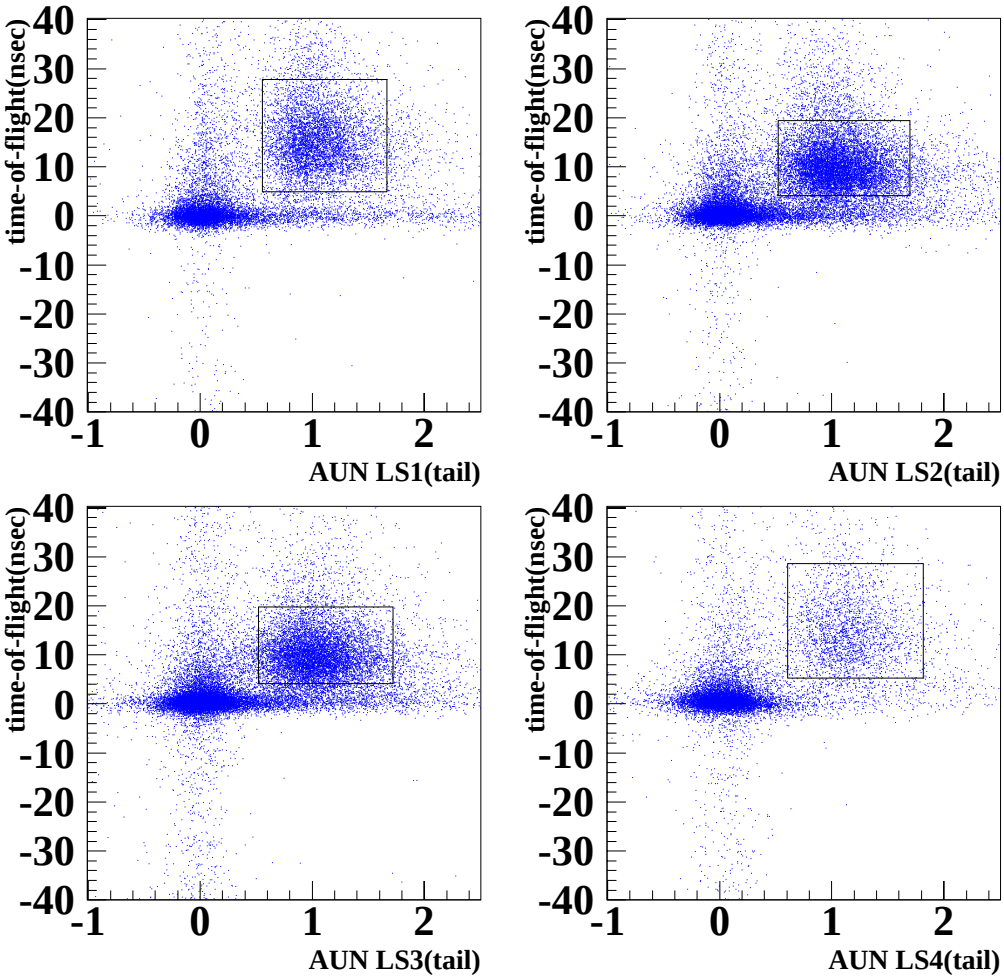

Figure 3: The AUN vs TOF for the 1mm-Pb/3mm-Scinti calorimeter in the 750 MeV run. A box are a region for neutrons.

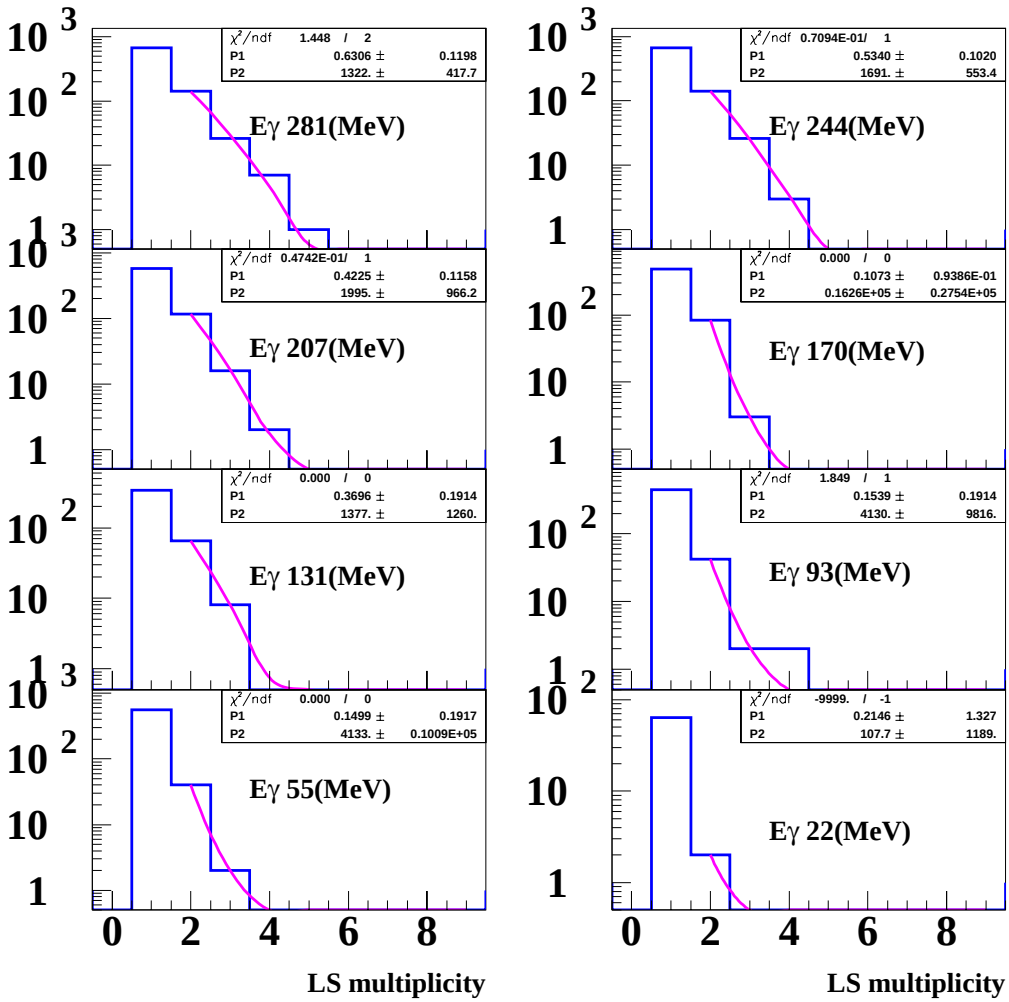

Figure 4: The multiplicity distributions of neutrons in liquid scintillators for the 1mm-Pb/3mm-Scinti calorimeter in 430 MeV.

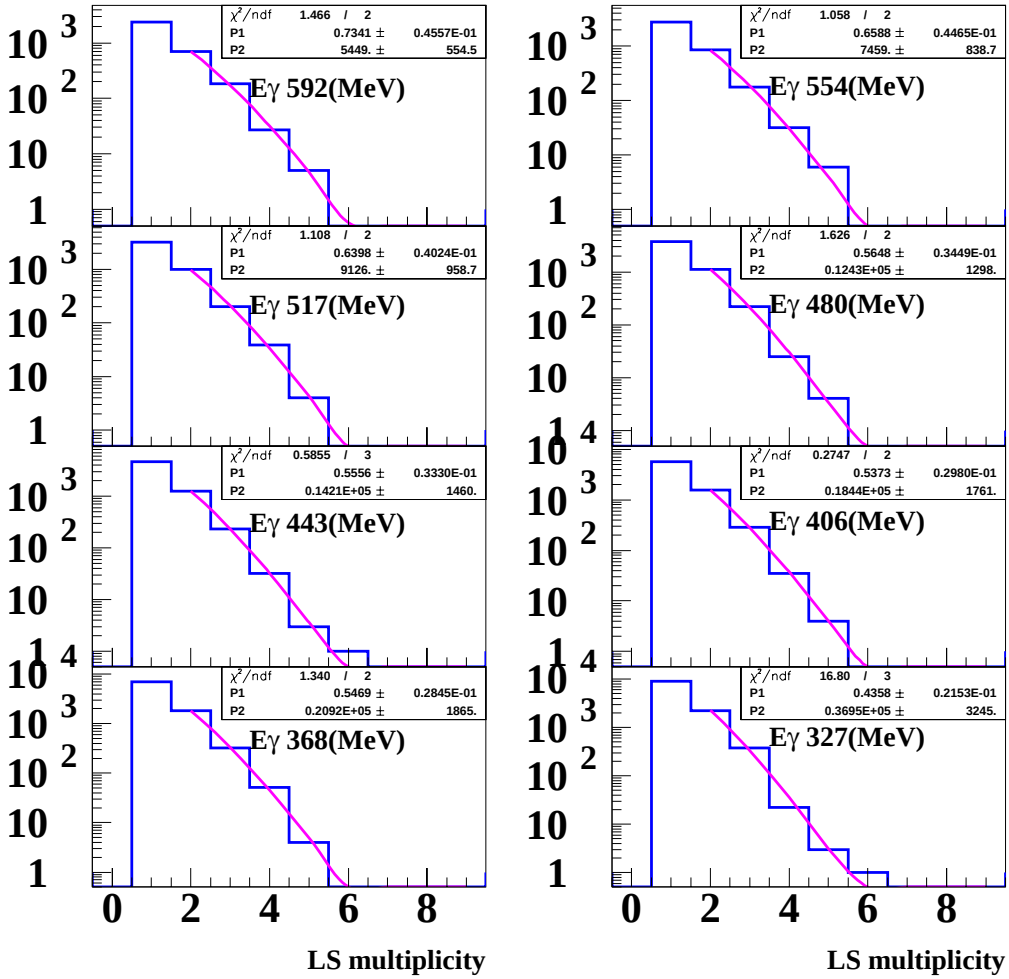

Figure 5: The multiplicity distributions of neutrons in liquid scintillators for the 1mm-Pb/3mm-Scinti calorimeter in the 750 MeV run.

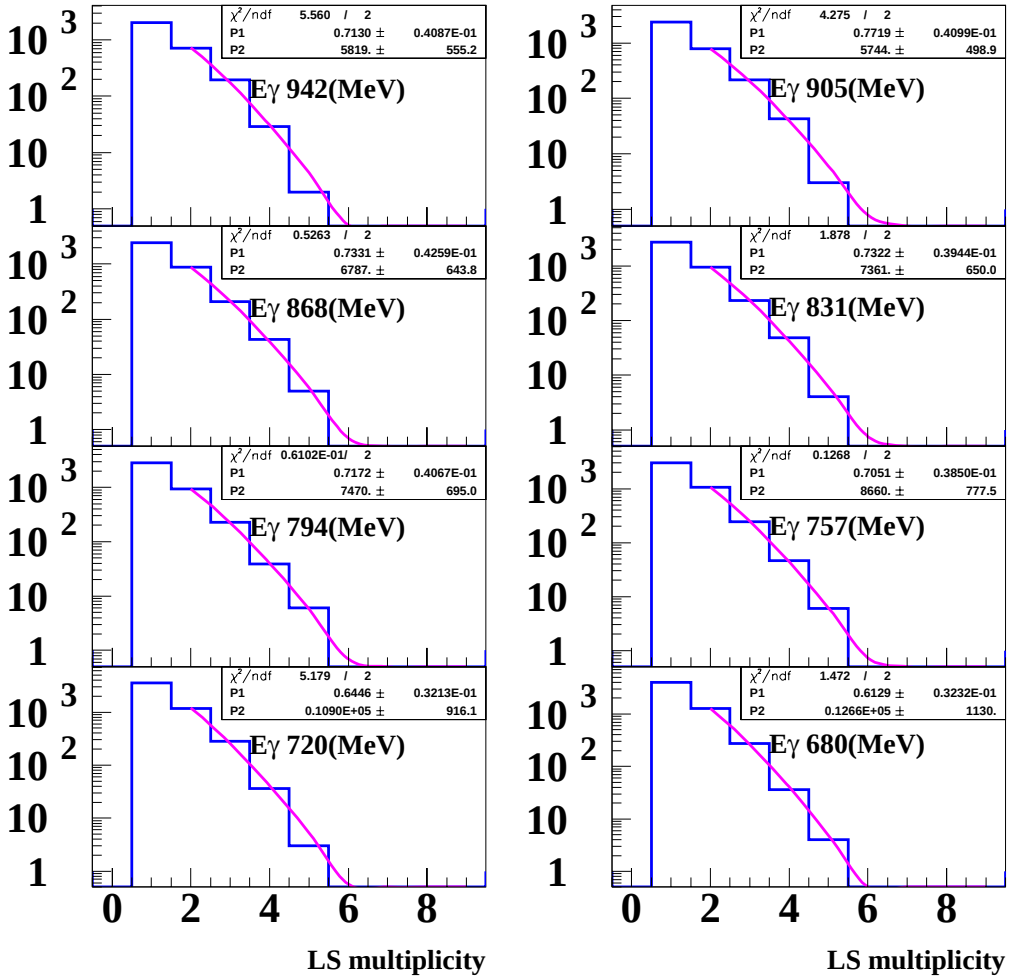

Figure 6: The multiplicity distributions of neutrons in liquid scintillators for the 1mm-Pb/3mm-Scinti calorimeter in the 1100 MeV run.

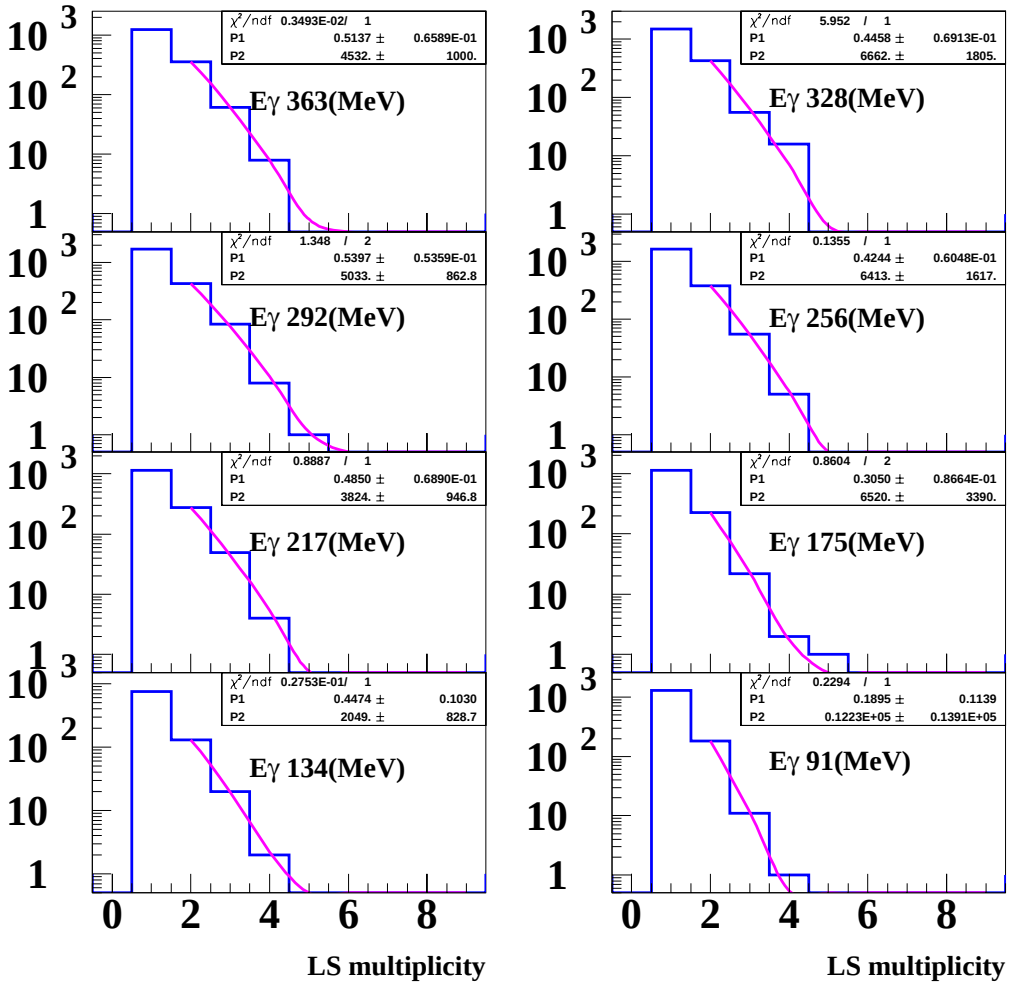

Figure 7: The multiplicity distributions of neutrons in liquid scintillators for the KEK-CsI calorimeter in the 500 MeV run.

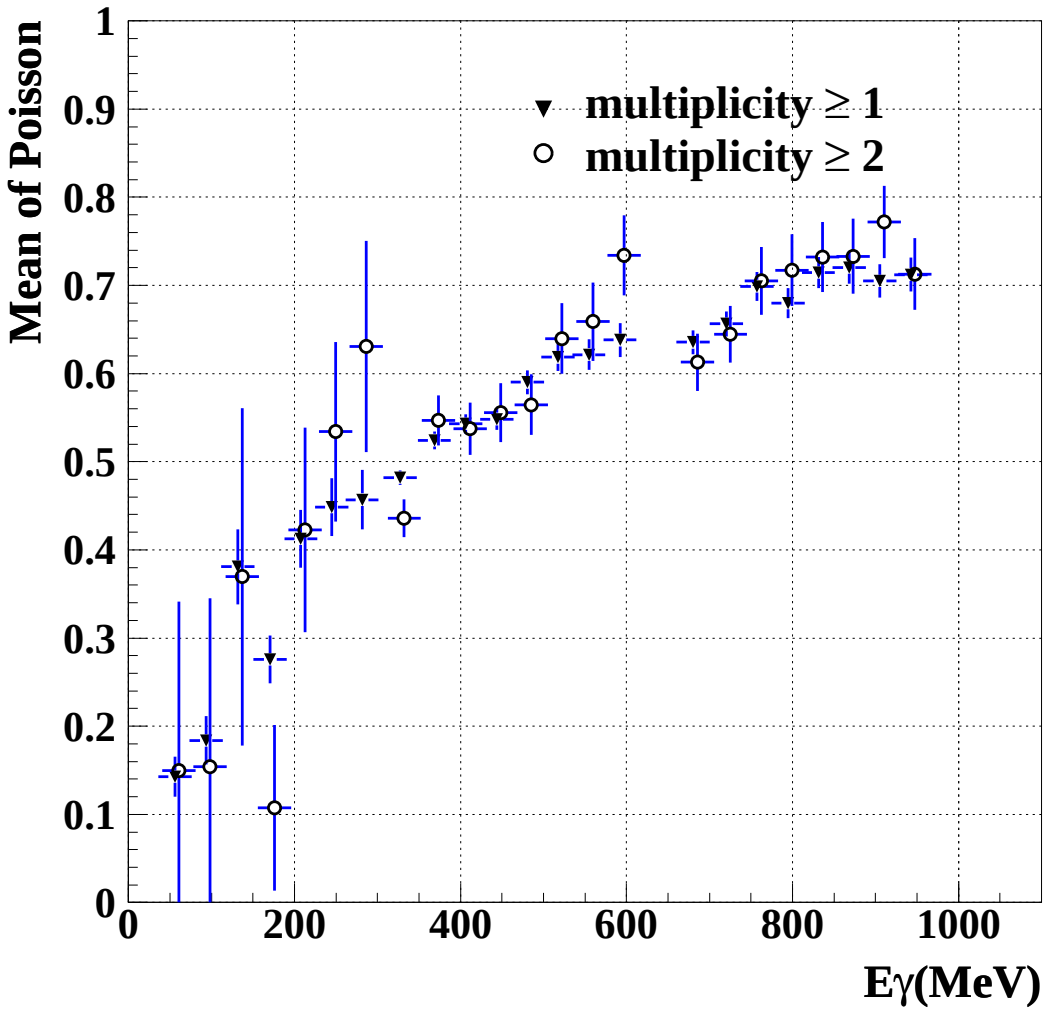

Figure 8: The energy dependence of the mean value of a Poisson distribution for the 1mm-Pb/3mm-Scinti calorimeter. The symbols of circle and triangle are the mean values of a Poisson distribution from the fit with the $m_{LS} \geq 1$ and 2.

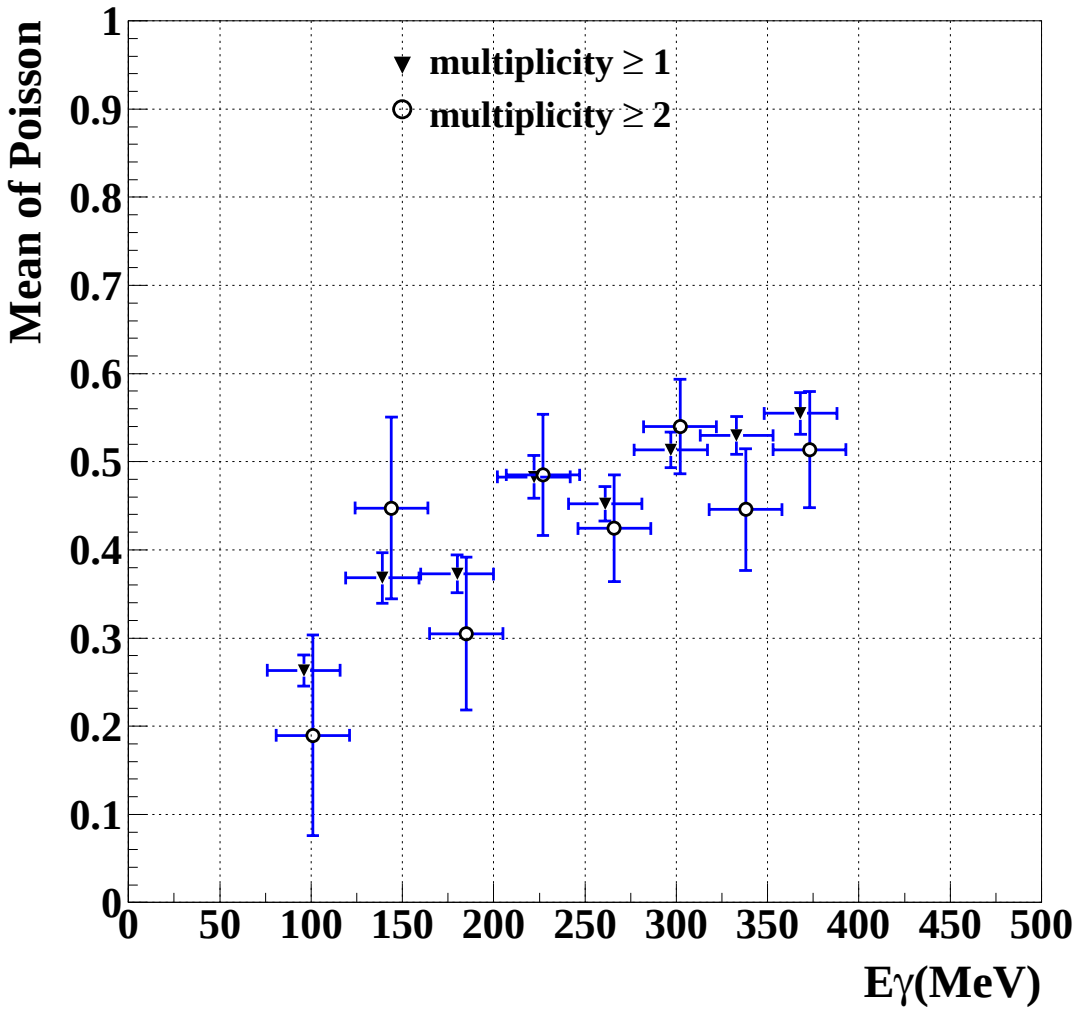

Figure 9: The energy dependence of a mean value of a Poisson distribution for KEK-CsI calorimeter. The symbols of circle and triangle are the mean values of a Poisson distribution from the fit with the $m_{LS} \geq 1$ and 2.

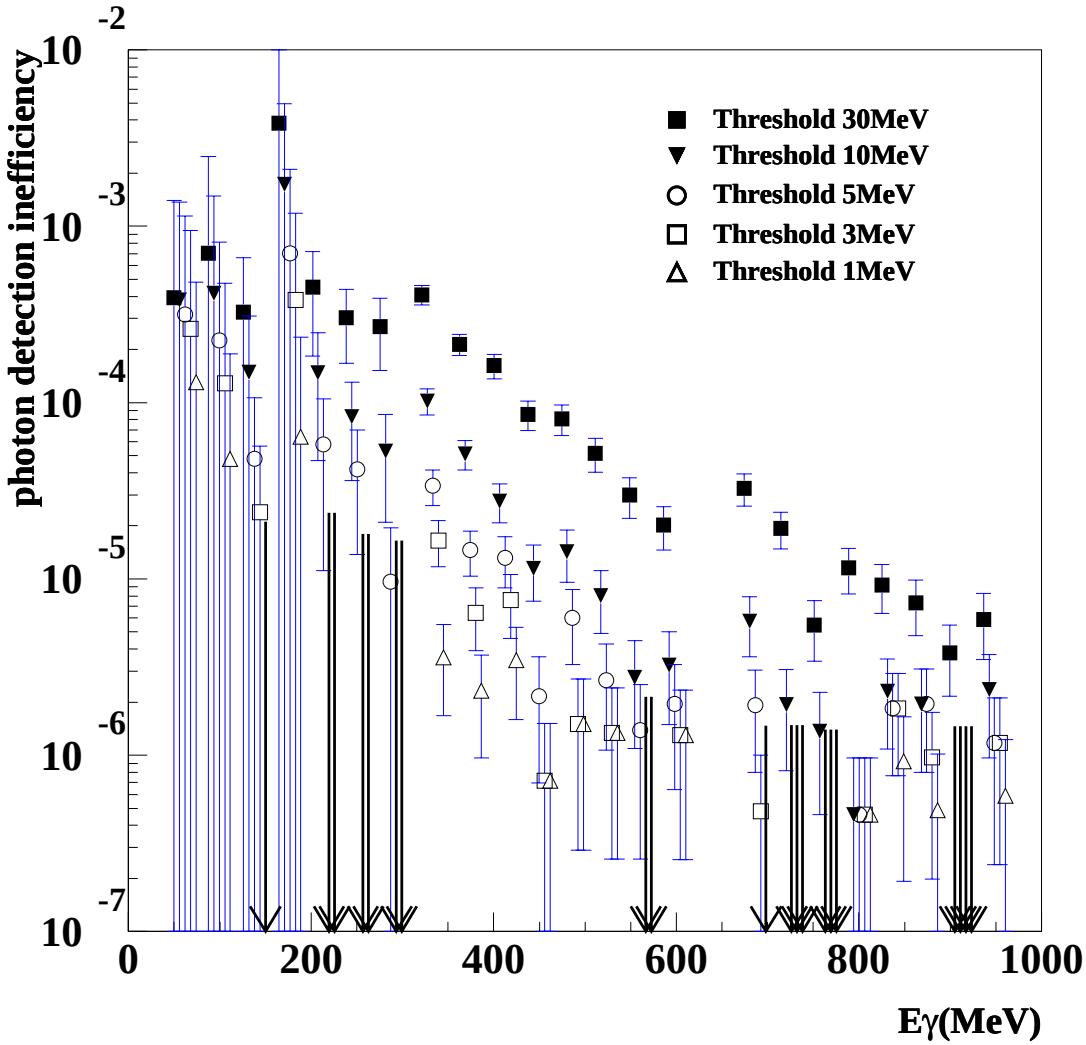

Figure 10: The detection inefficiency due to photonuclear interaction for the 1mm-Pb/3mm-Scinti calorimeter with a requirement of $m_{LS} \geq 2$. The arrow indicates the upper limit at the 90% confidence level.

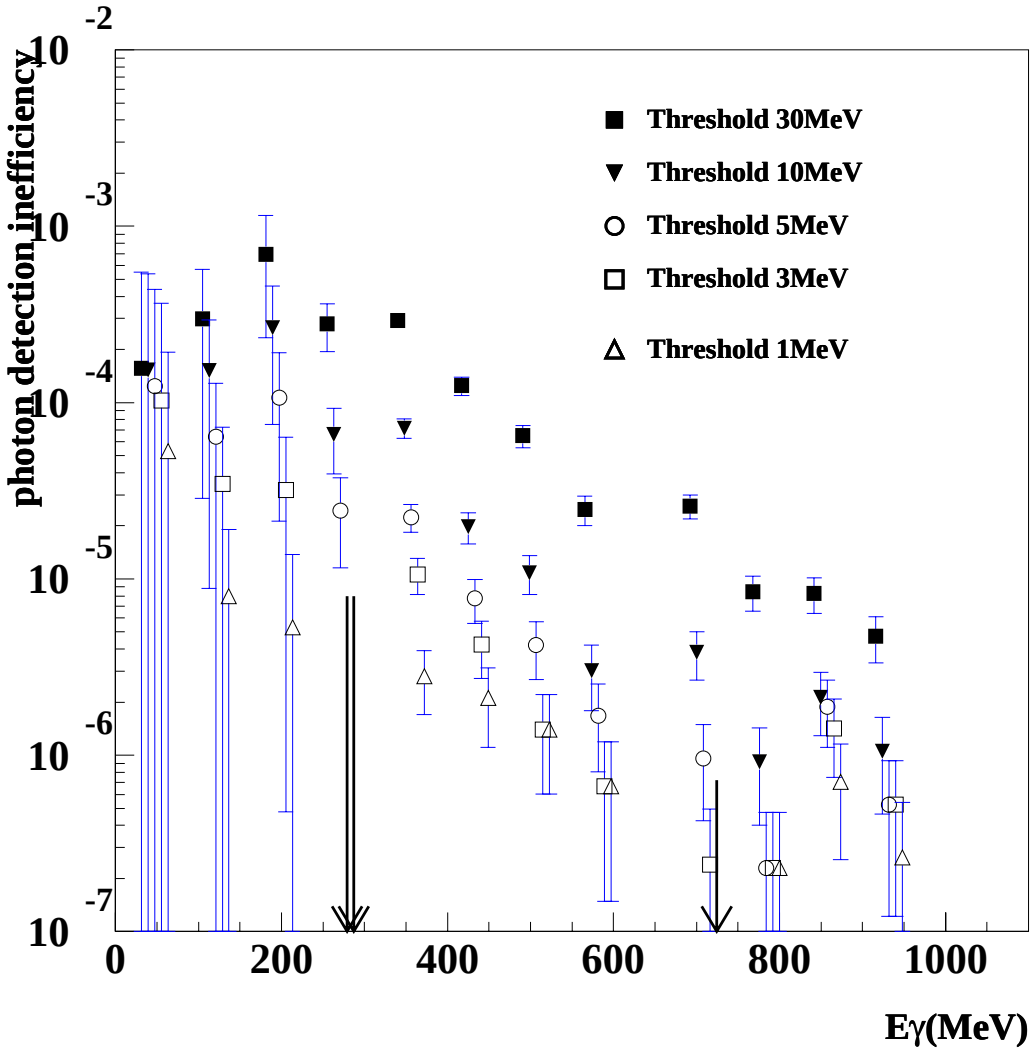

Figure 11: The detection inefficiency due to photonuclear interaction for the 1mm-Pb/3mm-Scinti calorimeter with a requirement of $m_{LS} \geq 2$ in 80 MeV-bin. The arrow indicates the upper limit at the 90% confidence level.

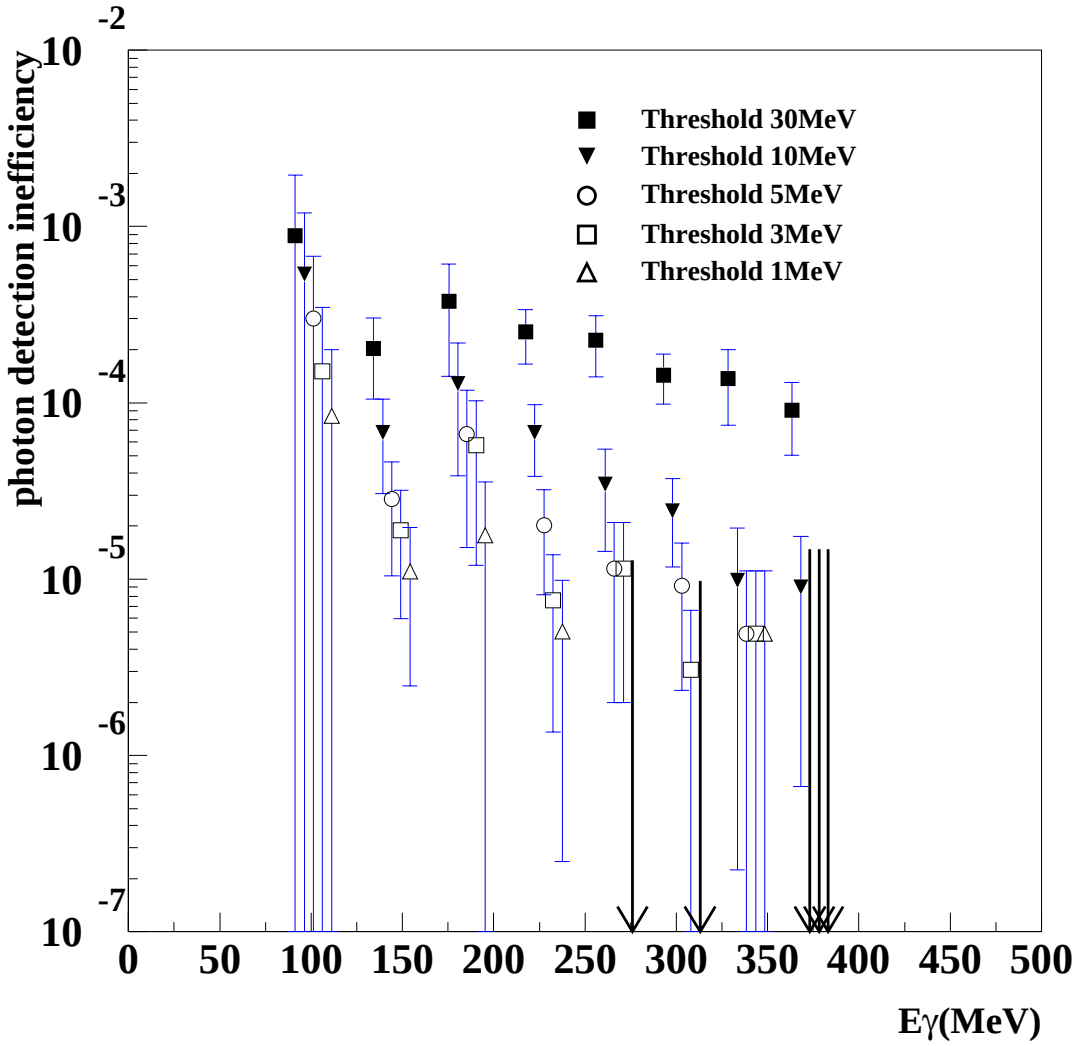

Figure 12: The detection inefficiency due to photonuclear interaction for the KEK-CsI calorimeter with a requirement of $m_{LS} \geq 2$. The arrow indicates the upper limit at the 90% confidence level.

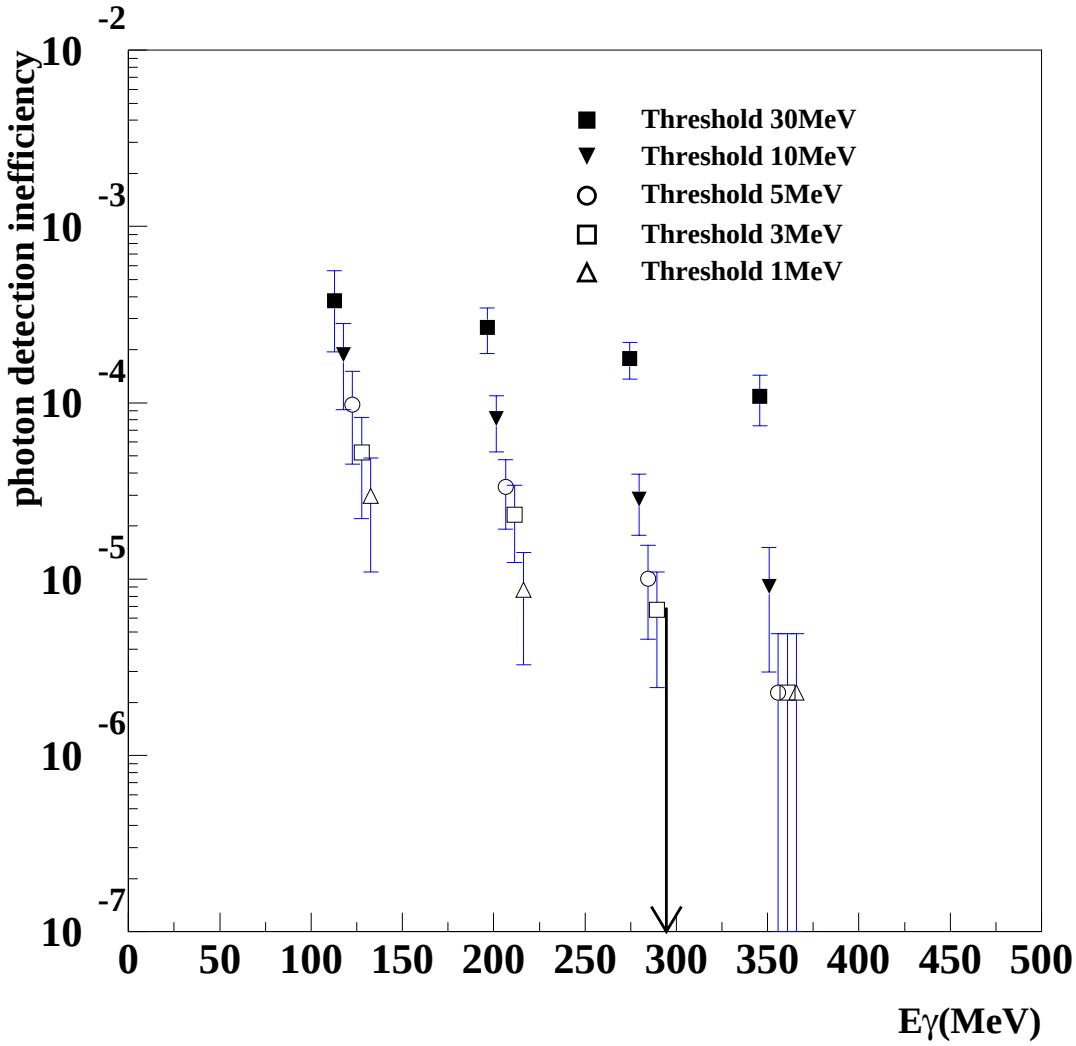

Figure 13: The detection inefficiency due to photonuclear interaction for the KEK-CsI calorimeter with a requirement of $m_{LS} \geq 2$ in 80 MeV-bin. The arrow indicates the upper limit at the 90% confidence level.

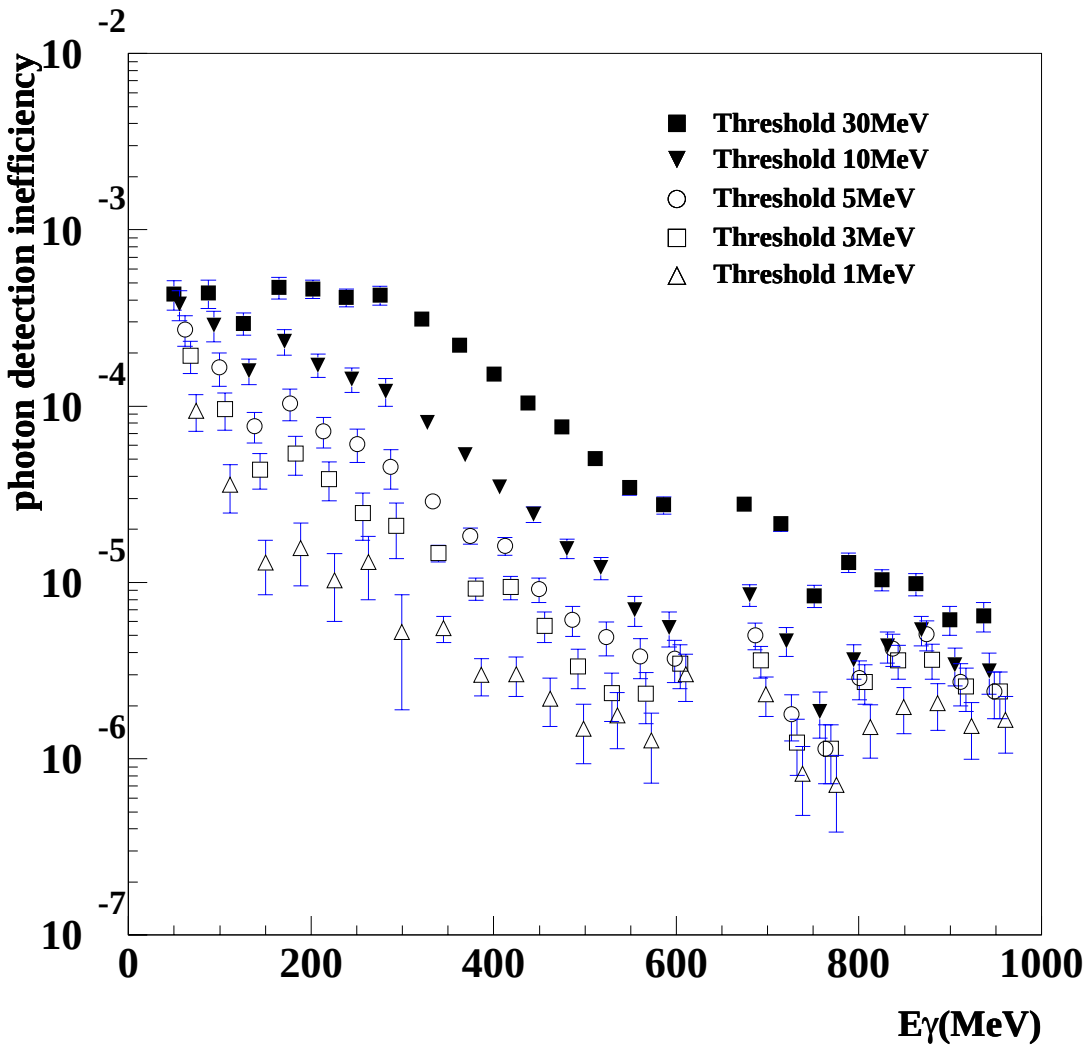

Figure 14: The detection inefficiency due to photonuclear interaction for the 1mm-Pb/3mm-Scinti calorimeter with a requirement of $m_{LS} \geq 1$.

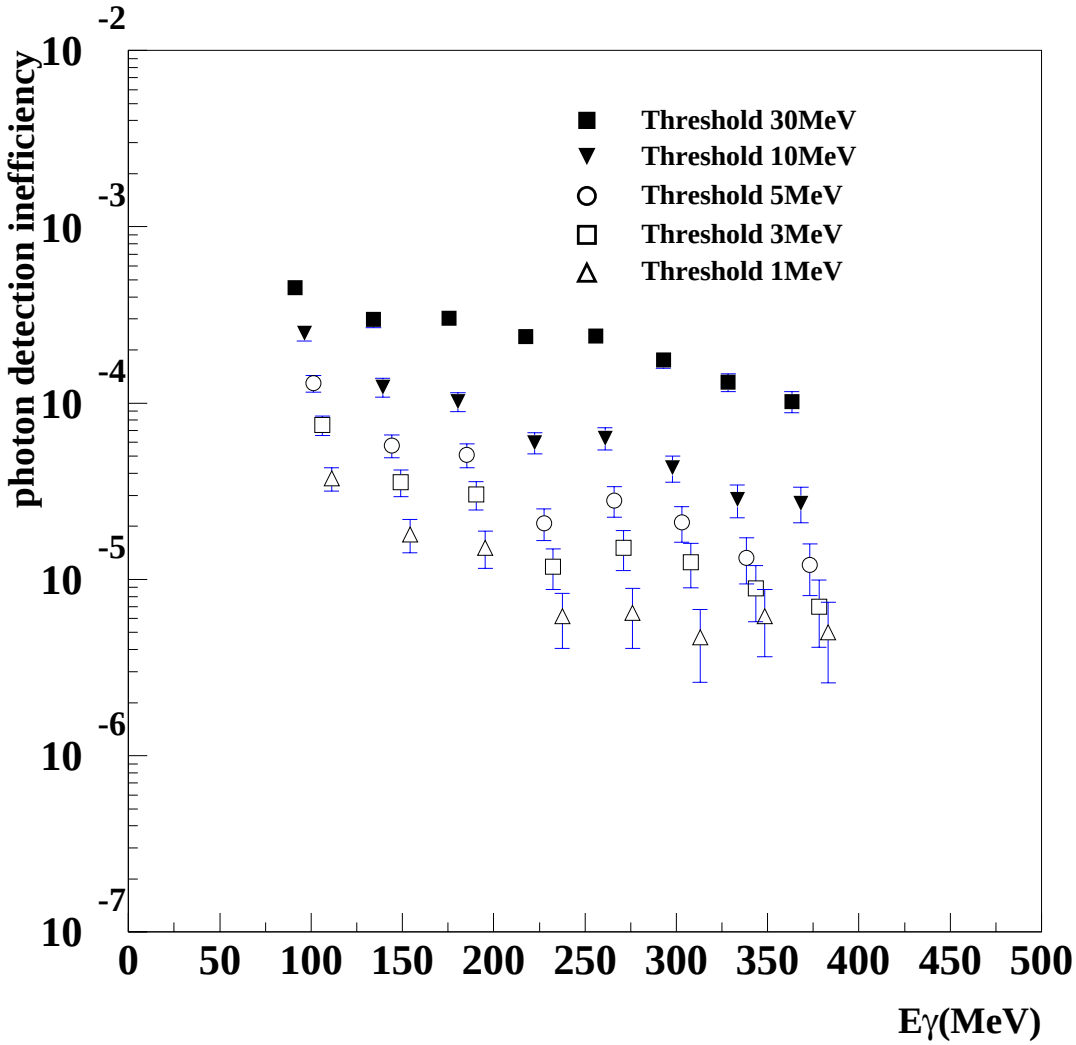

Figure 15: The detection inefficiency due to photonuclear interaction for the KEK-CsI calorimeter with a requirement of $m_{LS} \geq 1$.

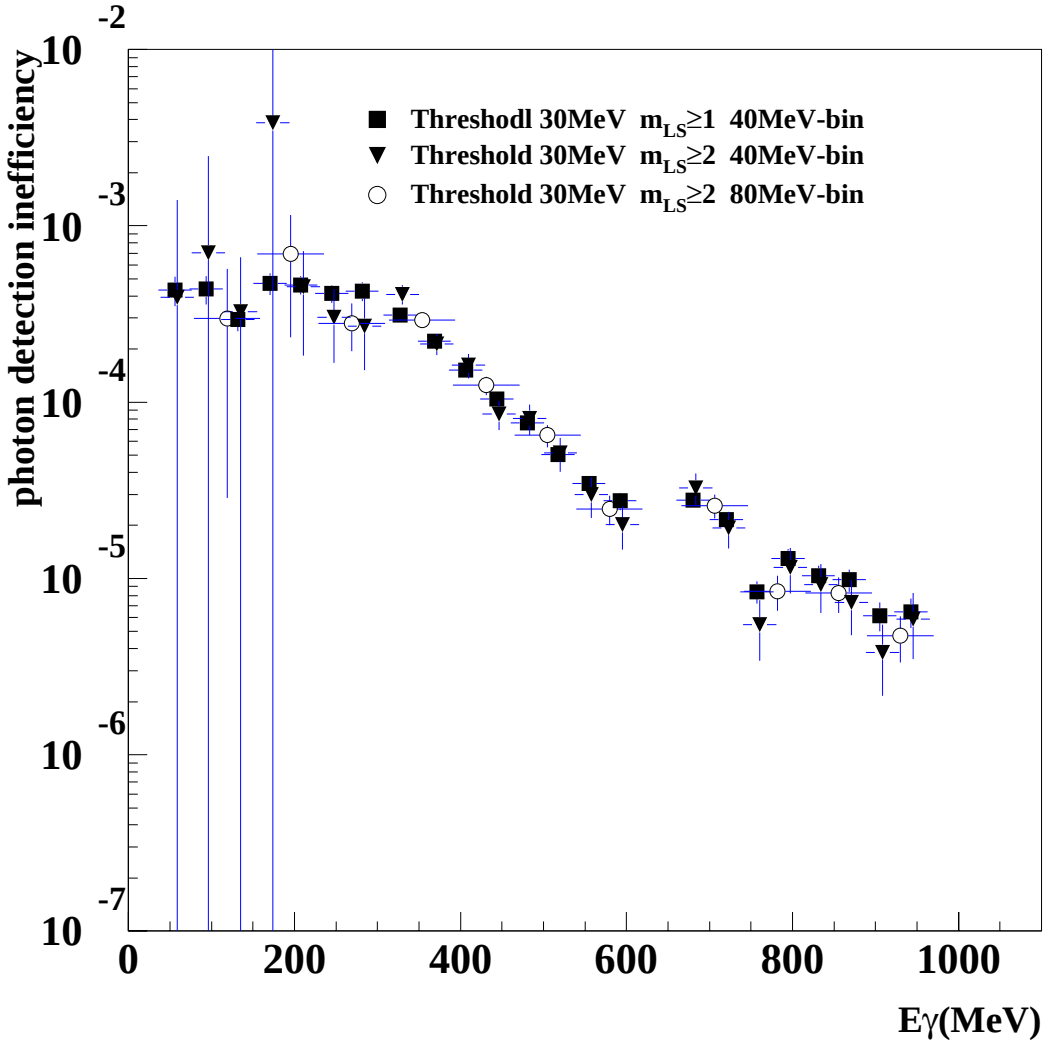

Figure 16: The detection inefficiency due to photonuclear interaction for the 1mm-Pb/3mm-Scinti calorimeter with each conditions for the 30 MeV threshold data.

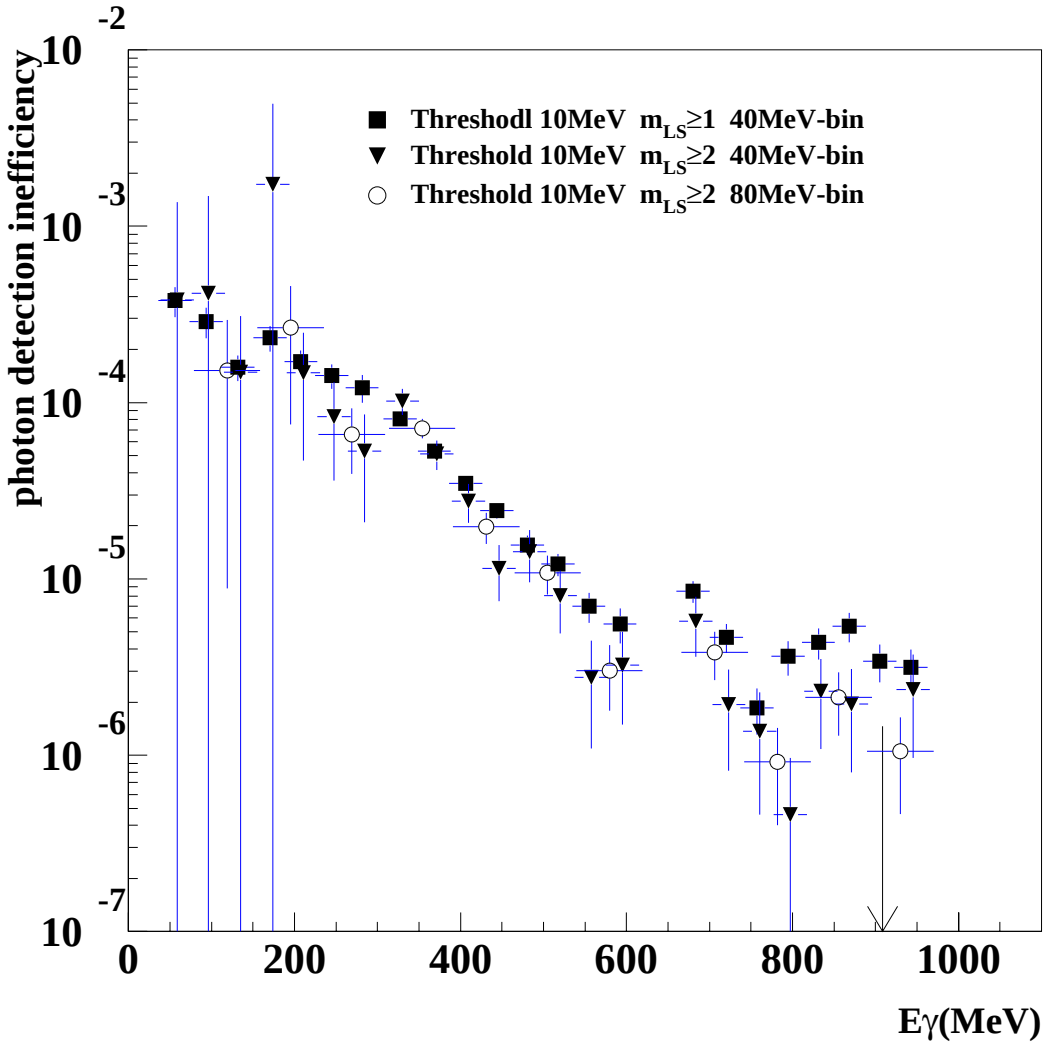

Figure 17: The detection inefficiency due to photonuclear interaction for the 1mm-Pb/3mm-Scinti calorimeter with each conditions for the 10MeV threshold data. The arrow indicates the upper limit at the 90% confidence level.

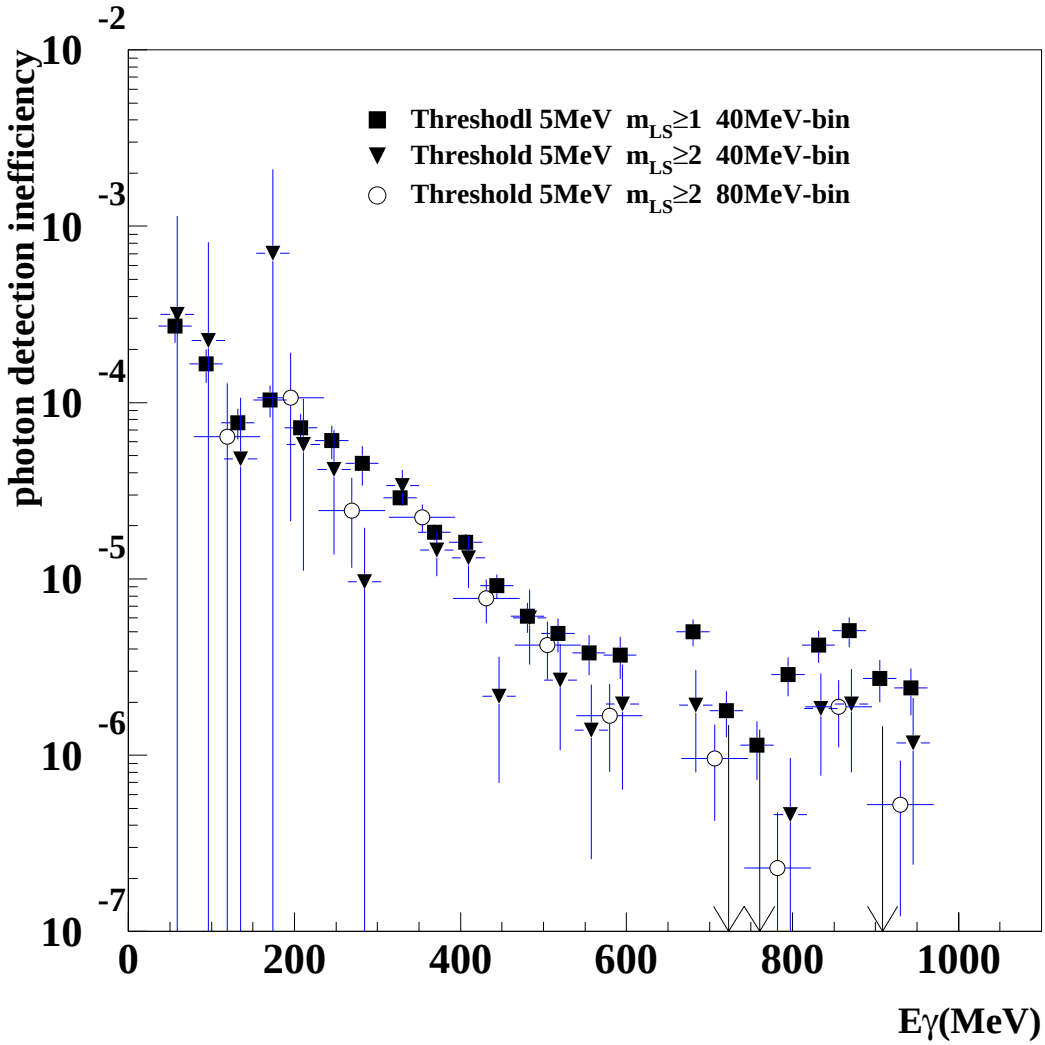

Figure 18: The detection inefficiency due to photonuclear interaction for the 1mm-Pb/3mm-Scinti calorimeter with each conditions for the 5 MeV threshold data. The arrow indicates the upper limit at the 90% confidence level.

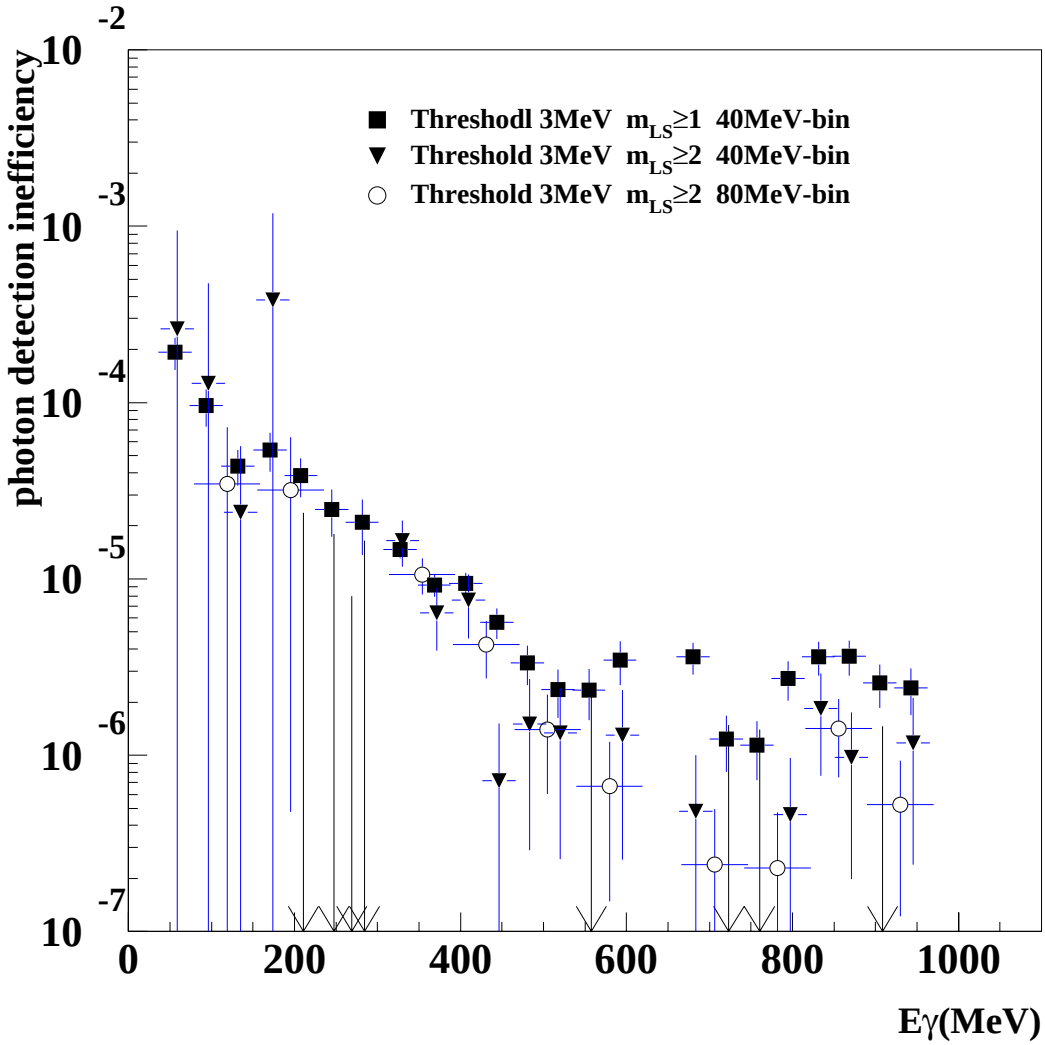

Figure 19: The detection inefficiency due to photonuclear interaction for the 1mm-Pb/3mm-Scinti calorimeter with each conditions for the 3 MeV threshold data. The arrow indicates the upper limit at the 90% confidence level.

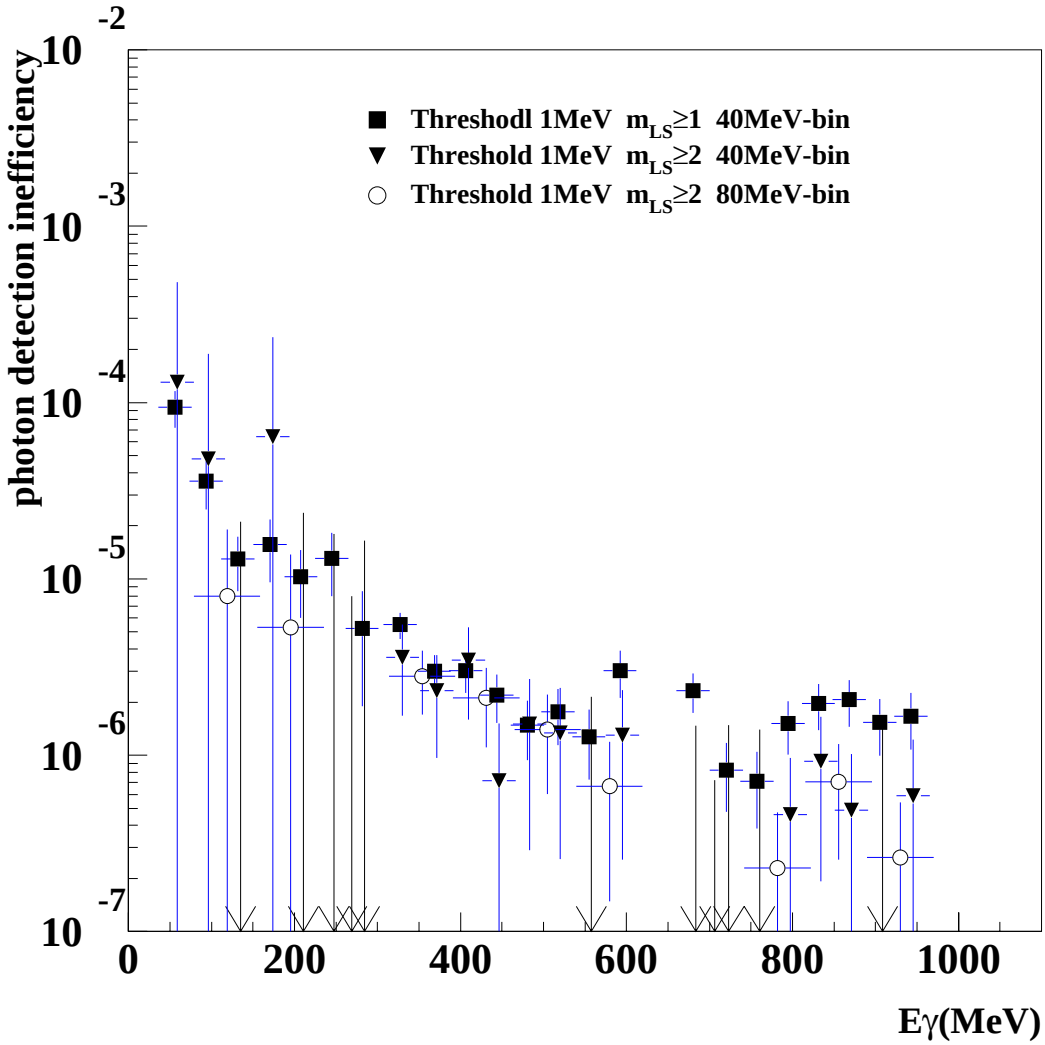

Figure 20: The detection inefficiency due to photonuclear interaction for the 1mm-Pb/3mm-Scinti calorimeter with each conditions for the 1 MeV threshold data. The arrow indicates the upper limit at the 90% confidence level.

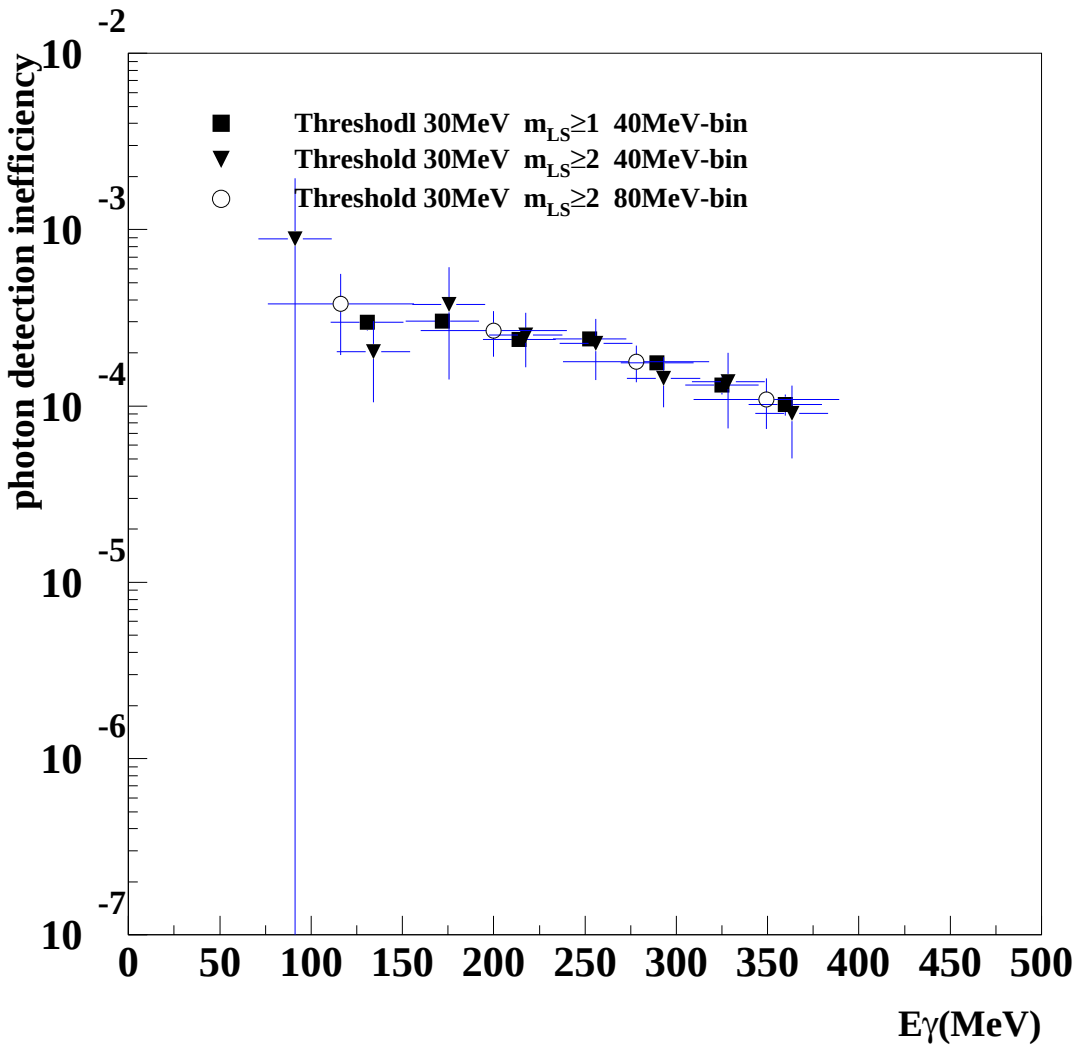

Figure 21: The detection inefficiency due to photonuclear interaction for the KEK-CsI calorimeter with each conditions for the 30 MeV threshold data.

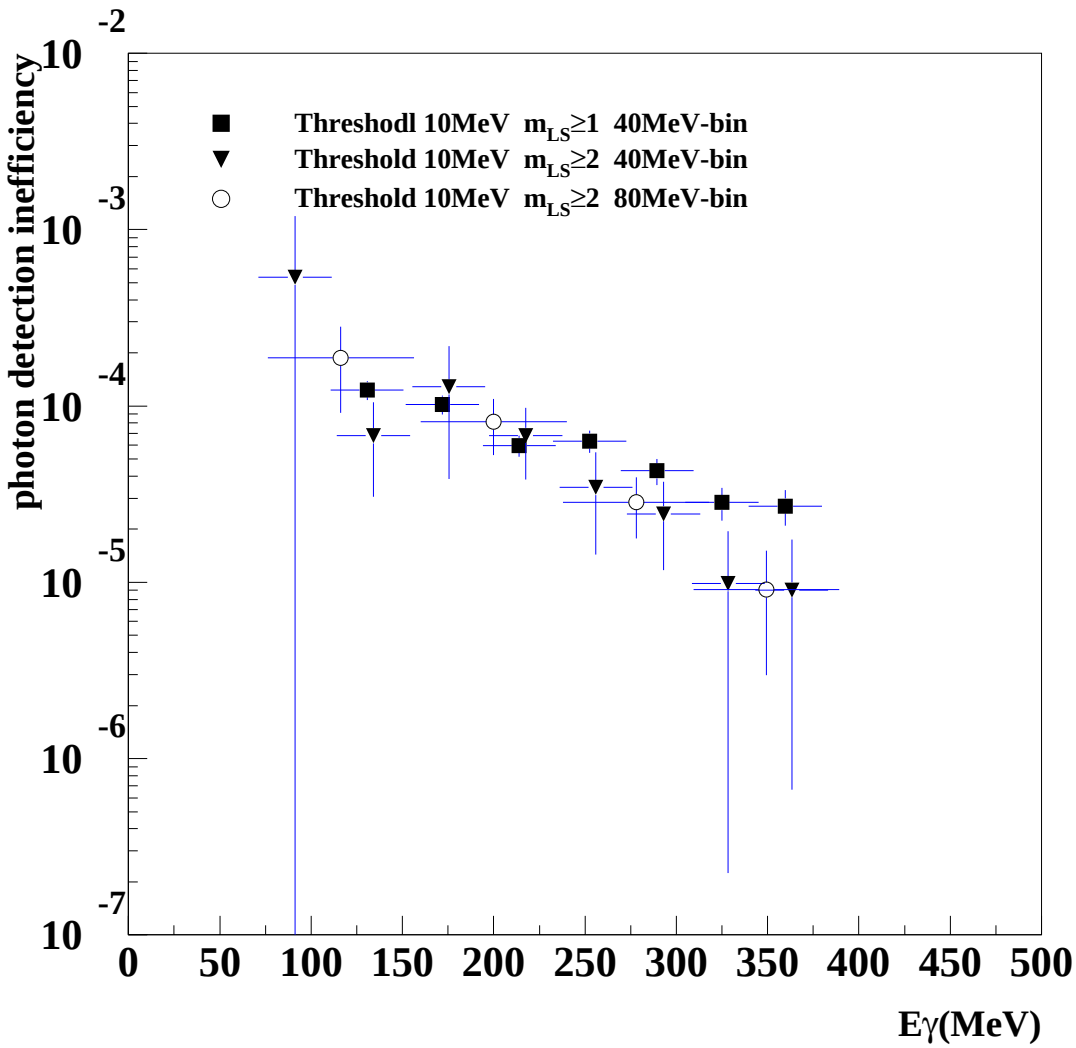

Figure 22: The detection inefficiency due to photonuclear interaction for the KEK-CsI calorimeter with each conditions for the 10 MeV threshold data.

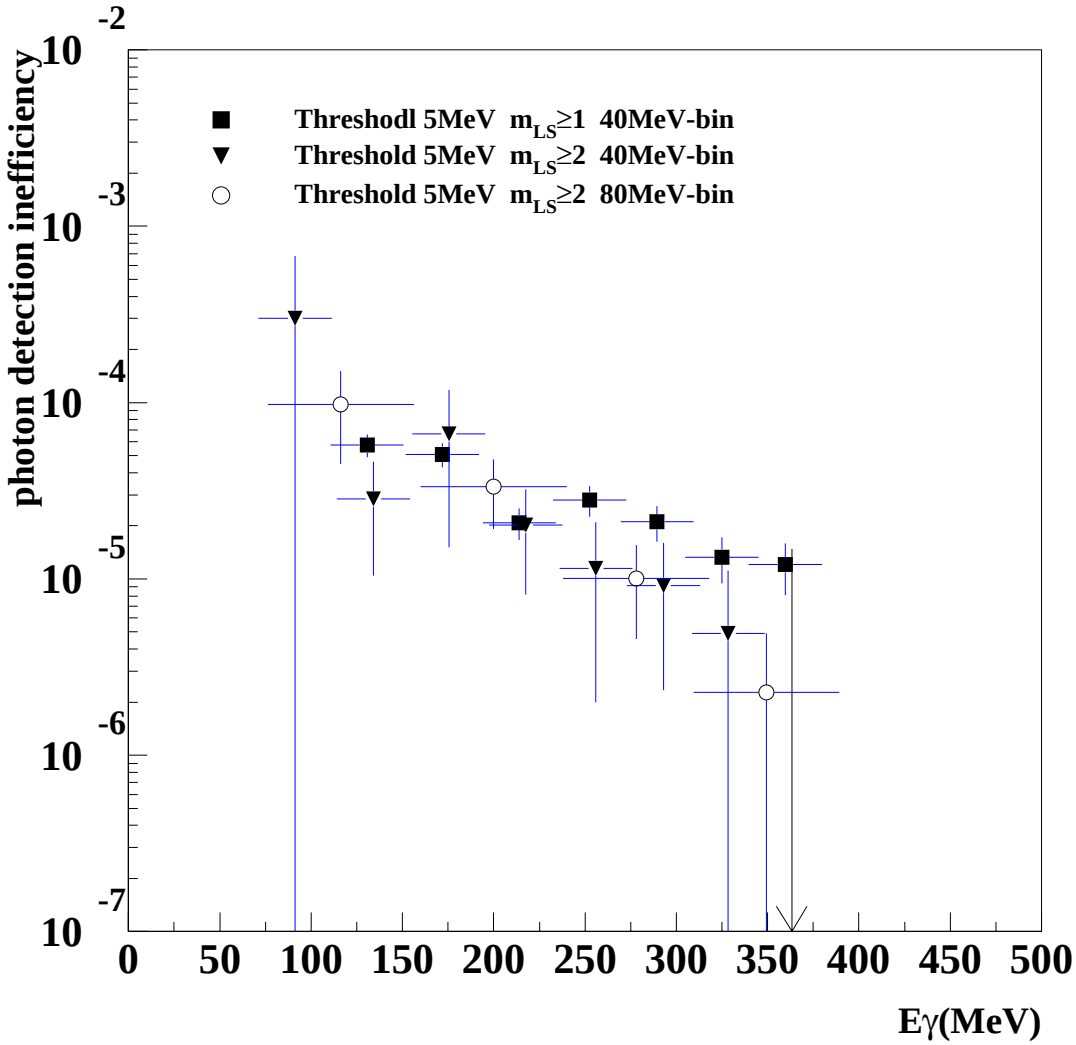

Figure 23: The detection inefficiency due to photonuclear interaction for the KEK-CsI calorimeter with each conditions with for the 5 MeV threshold data. The arrow indicates the upper limit at the 90% confidence level.

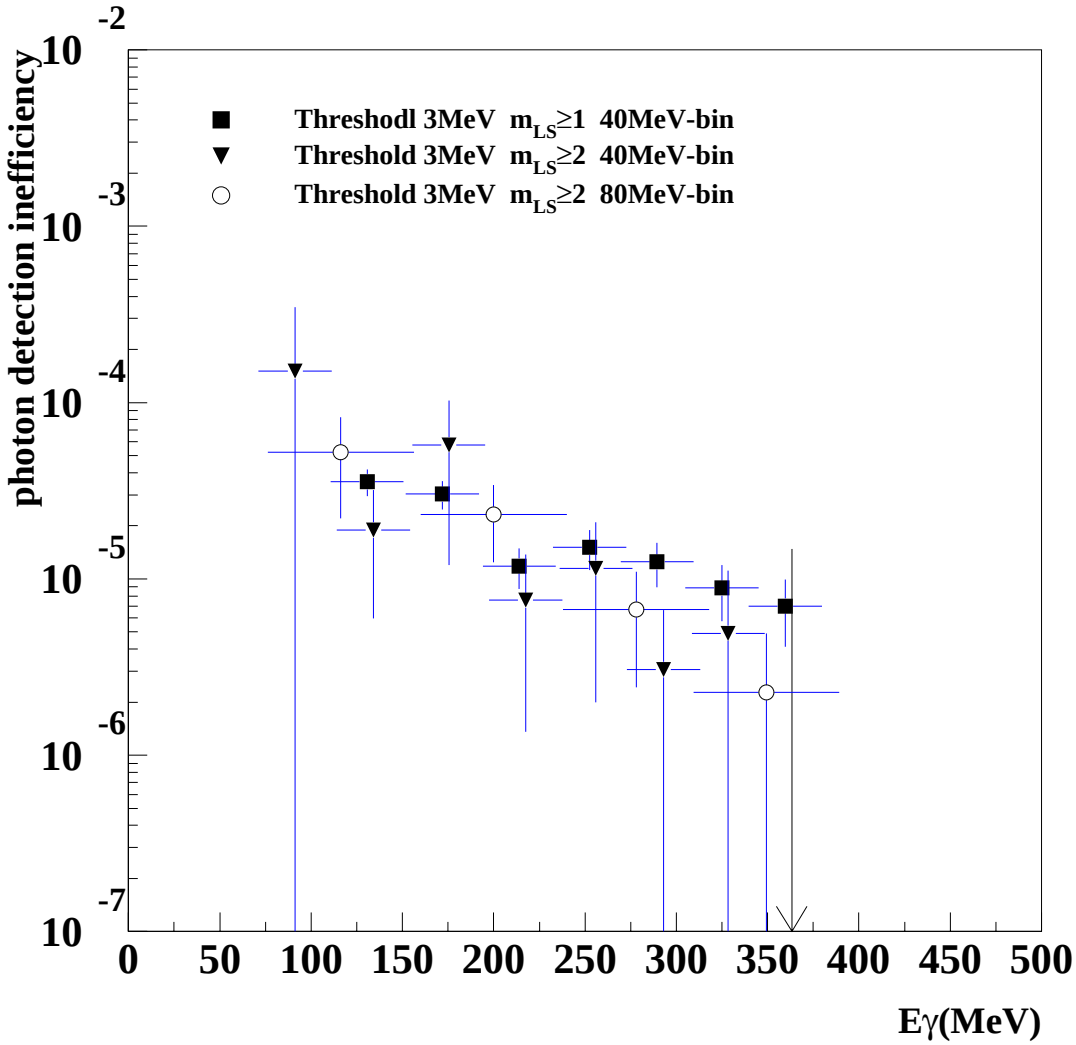

Figure 24: The detection inefficiency due to photonuclear interaction for the KEK-CsI calorimeter with each conditions for the 3 MeV threshold data. The arrow indicates the upper limit at the 90% confidence level.

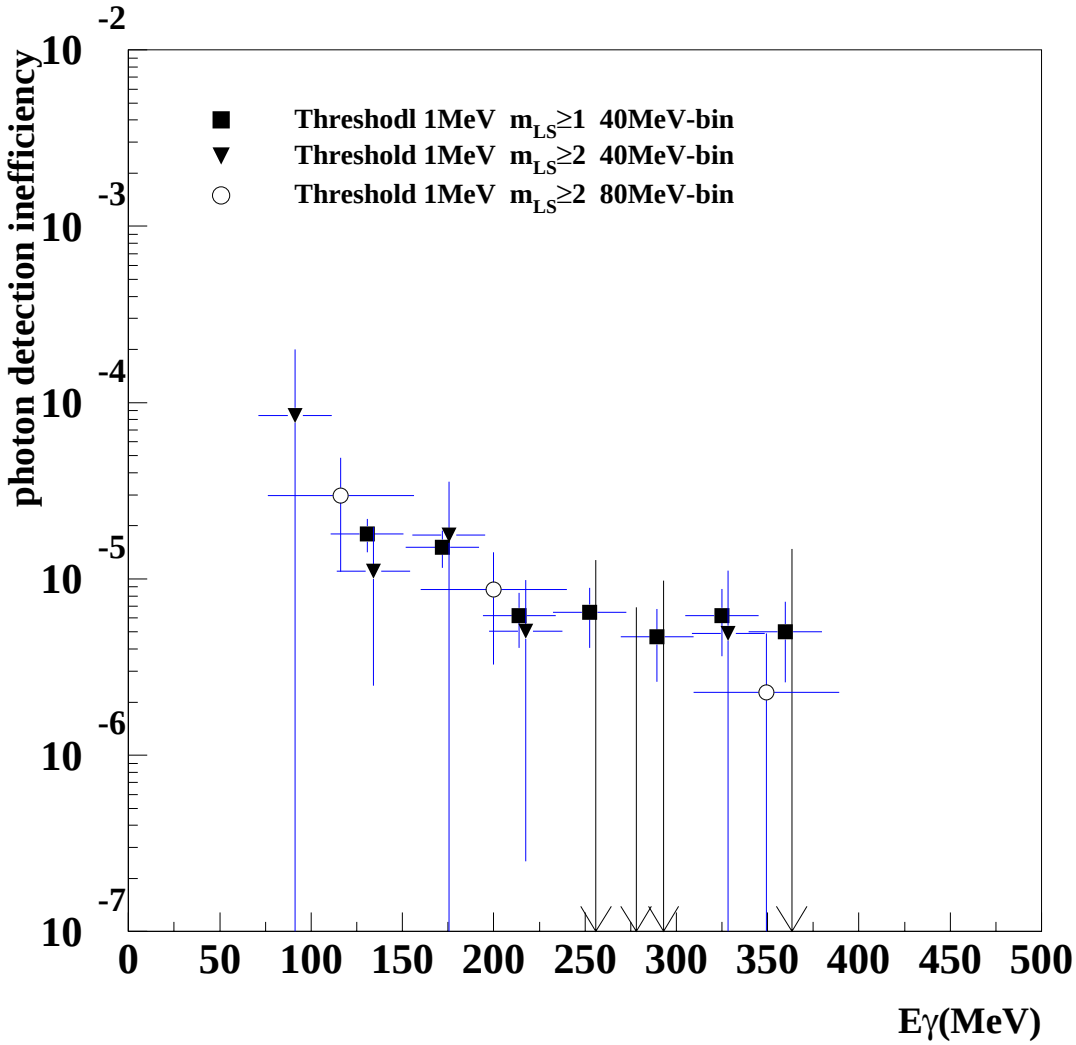

Figure 25: The detection inefficiency due to photonuclear interaction for the KEK-CsI calorimeter with each conditions for the 1 MeV threshold data. The arrow indicates the upper limit at the 90% confidence level.

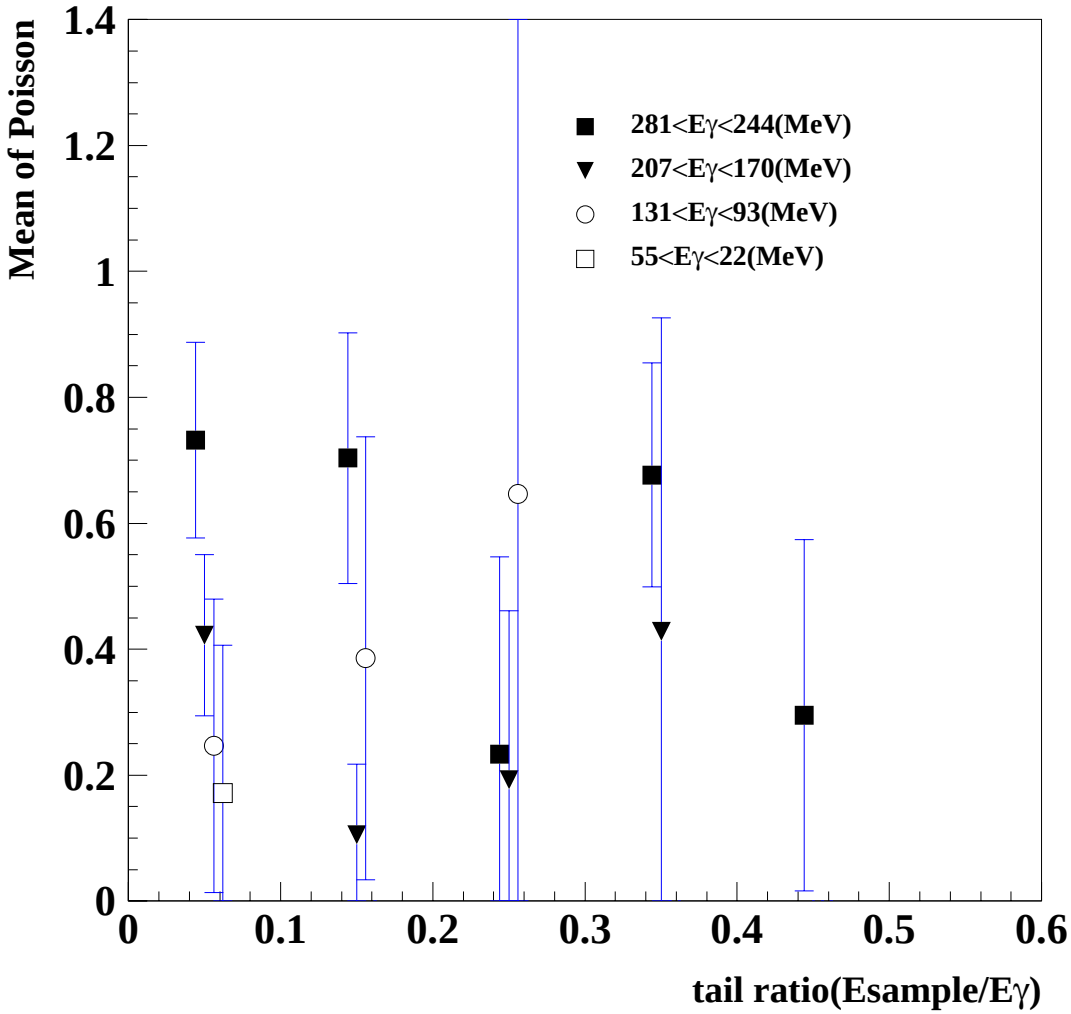

Figure 26: The E_{sample}/E_{γ} dependence of the mean value of a Poisson distribution with the $m_{LS} \geq 2$ for the 1mm-Pb/3mm-Scinti calorimeter in the 430 MeV run.

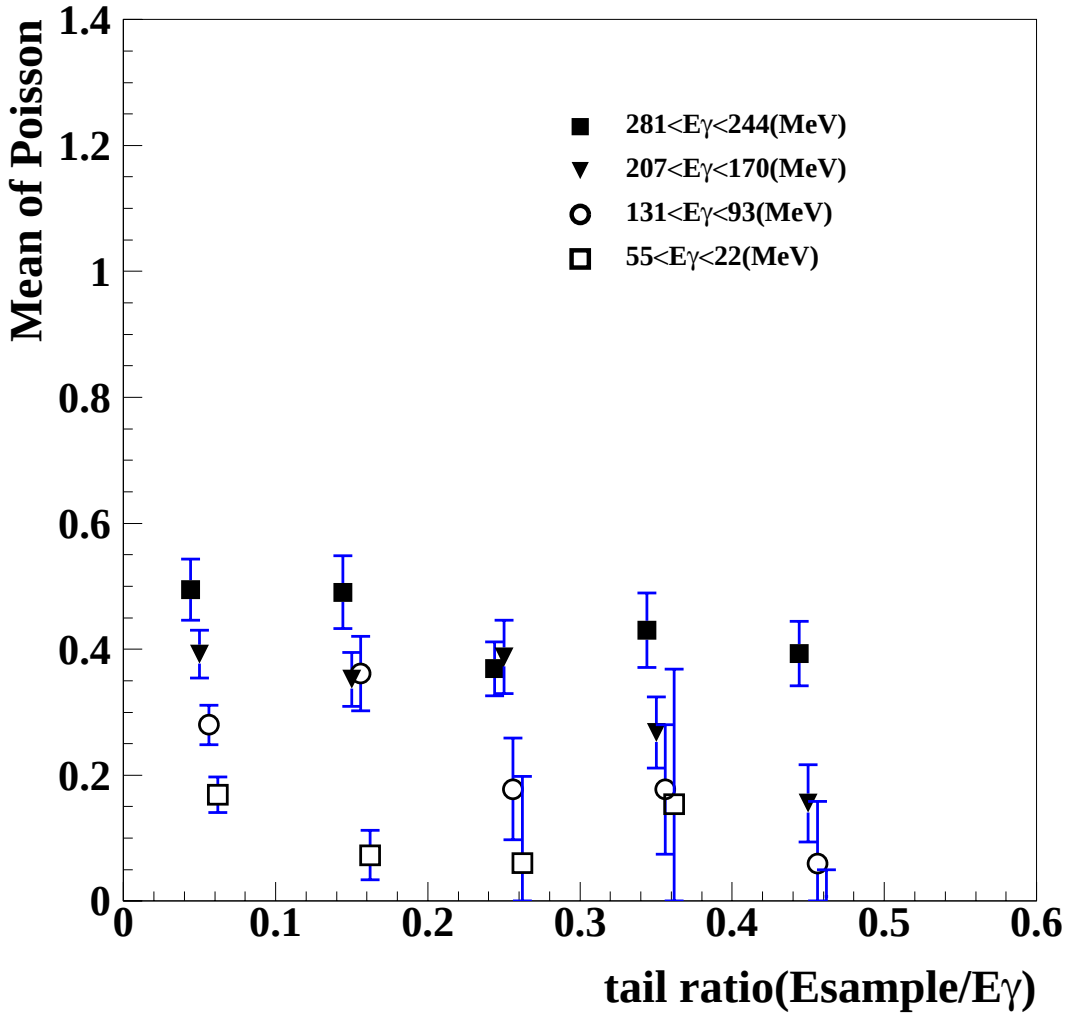

Figure 27: The E_{sample}/E_{γ} dependence of the mean value of a Poisson distribution with the $m_{LS} \geq 1$ for the 1mm-Pb/3mm-Scinti calorimeter in the 430 MeV run.

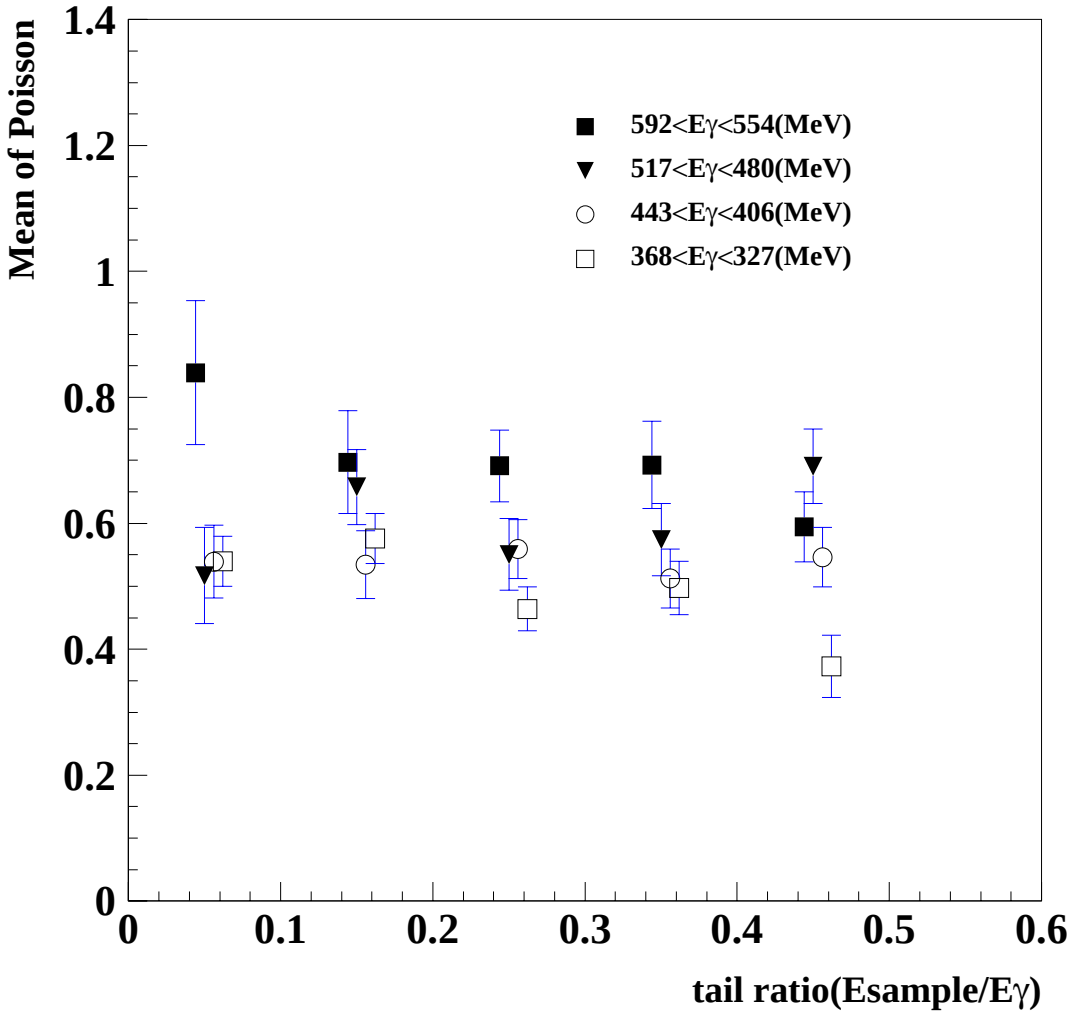

Figure 28: The E_{sample}/E_{γ} dependence of the mean value of a Poisson distribution with the $m_{LS} \geq 2$ for the 1mm-Pb/3mm-Scinti calorimeter in the 750 MeV run.

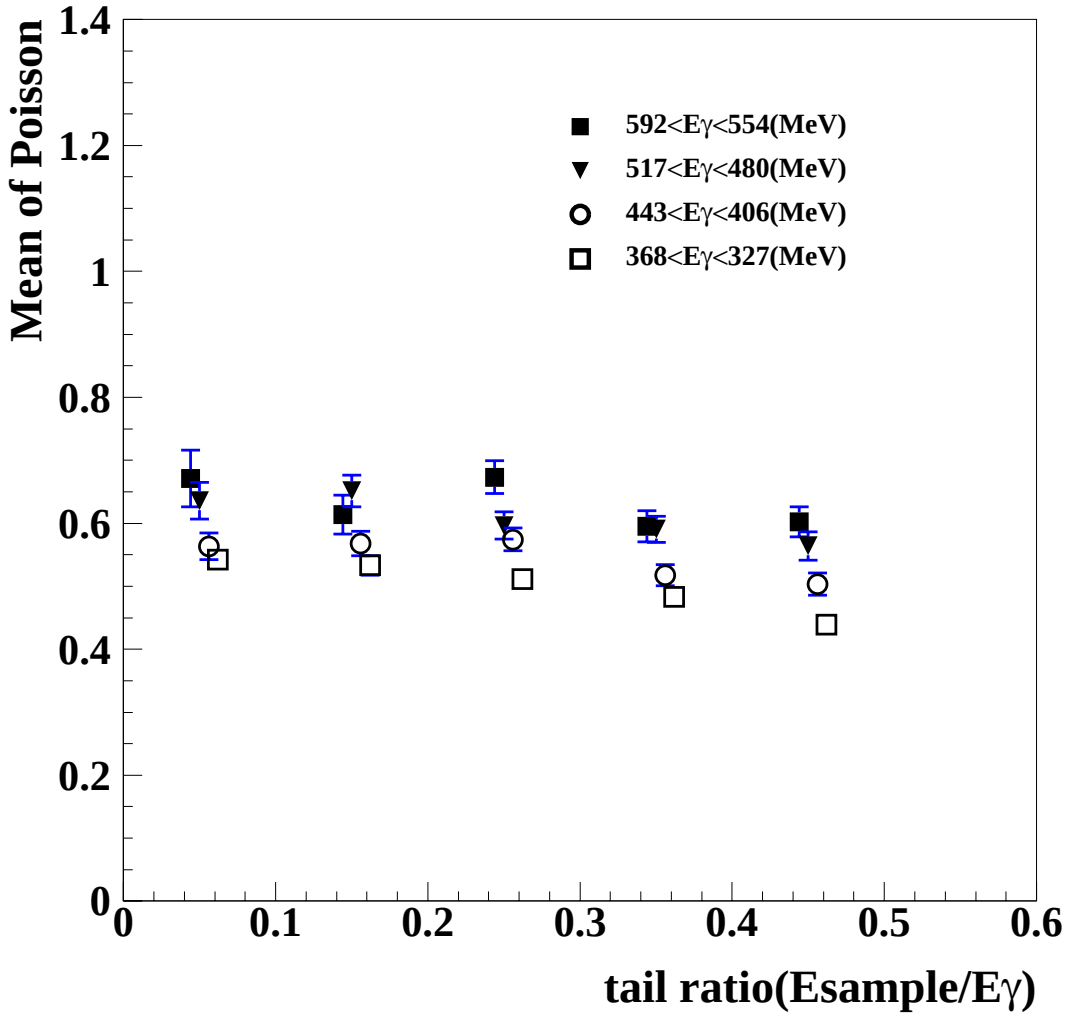

Figure 29: The E_{sample}/E_{γ} dependence of the mean value of a Poisson distribution with the $m_{LS} \geq 1$ for the 1mm-Pb/3mm-Scinti calorimeter in the 750 MeV run.

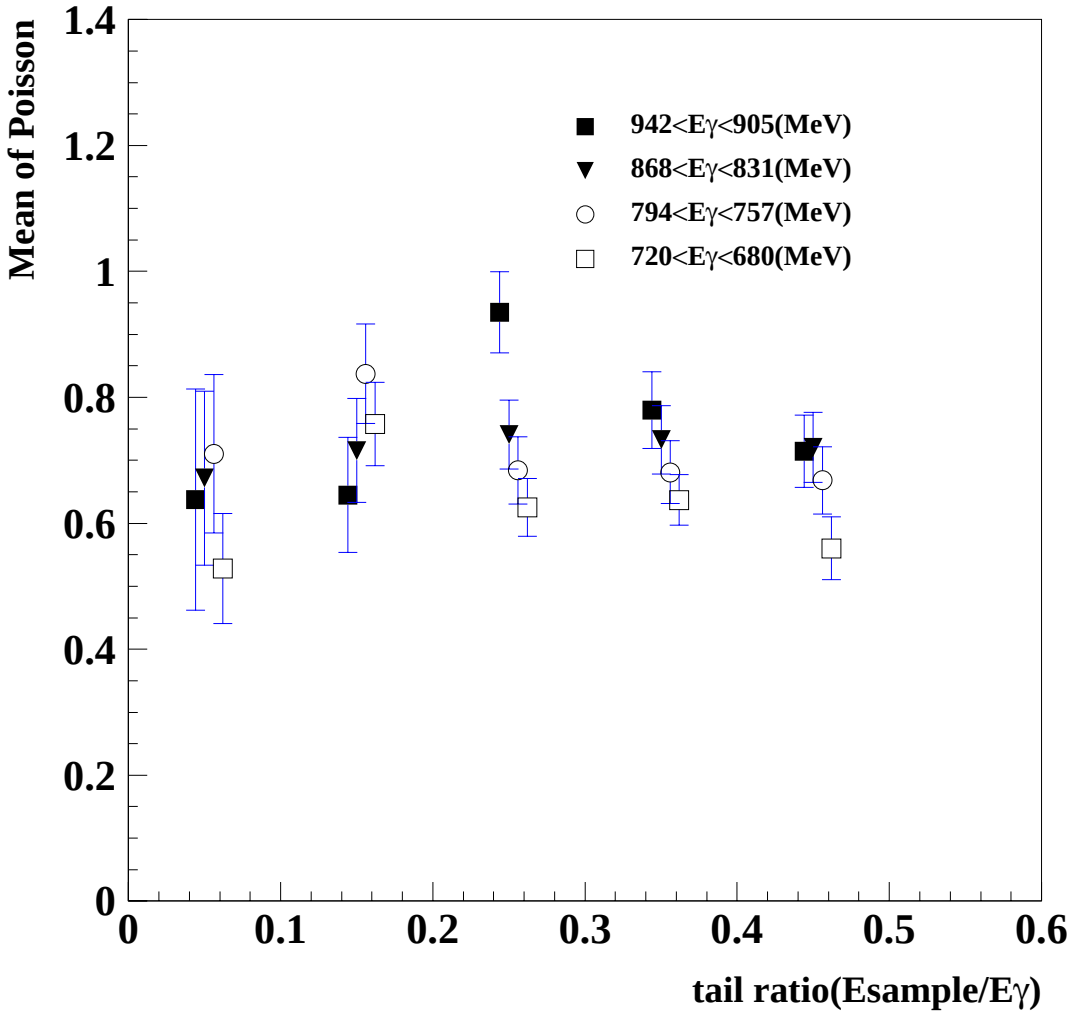

Figure 30: The E_{sample}/E_{γ} dependence of the mean value of a Poisson distribution with the $m_{LS} \geq 2$ for the 1mm-Pb/3mm-Scinti calorimeter in the 1100 MeV run.

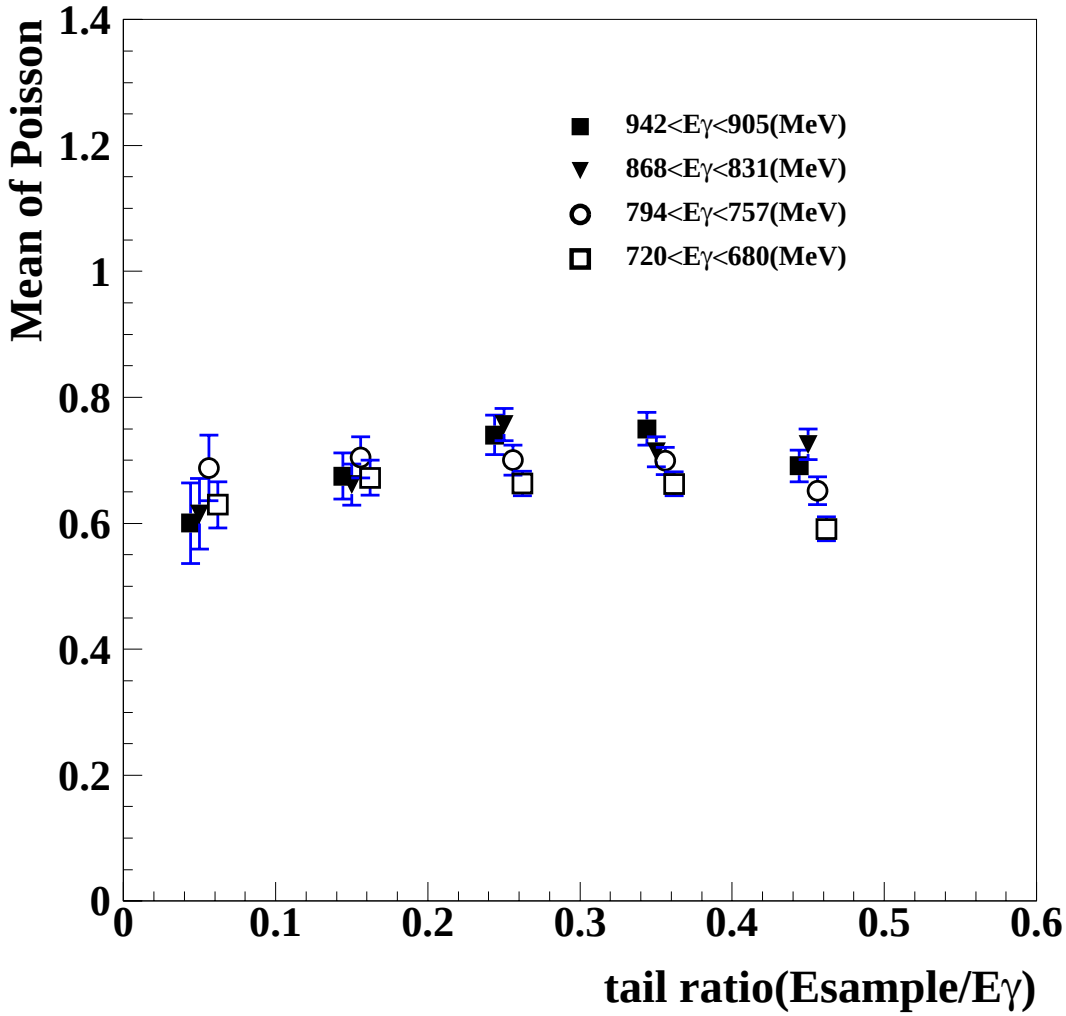

Figure 31: The E_{sample}/E_{γ} dependence of the mean value of a Poisson distribution with the $m_{LS} \geq 1$ for the 1mm-Pb/3mm-Scinti calorimeter in the 1100 MeV run.

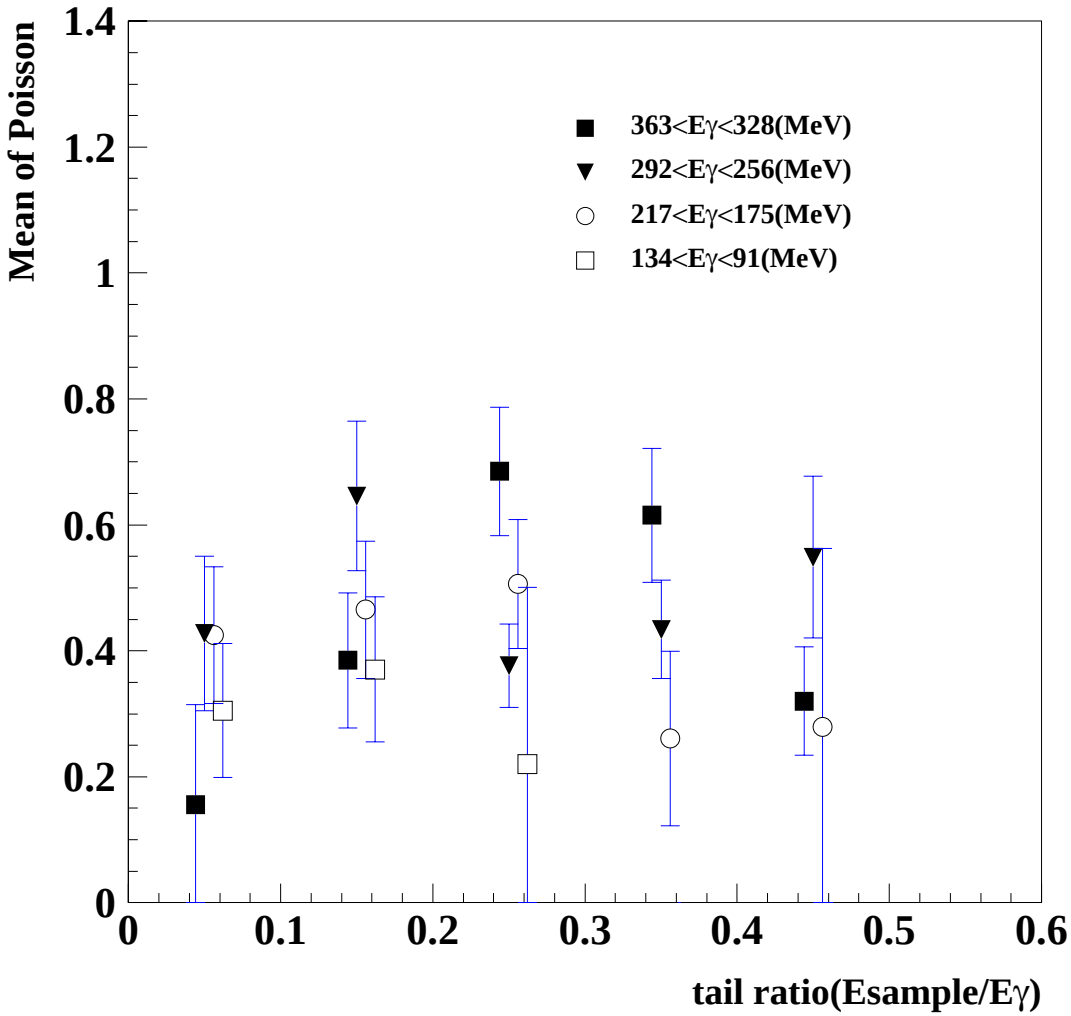

Figure 32: The E_{sample}/E_{γ} dependence of the mean value of a Poisson distribution with the $m_{LS} \geq 2$ for the KEK-CsI calorimeter in the 500 MeV run.

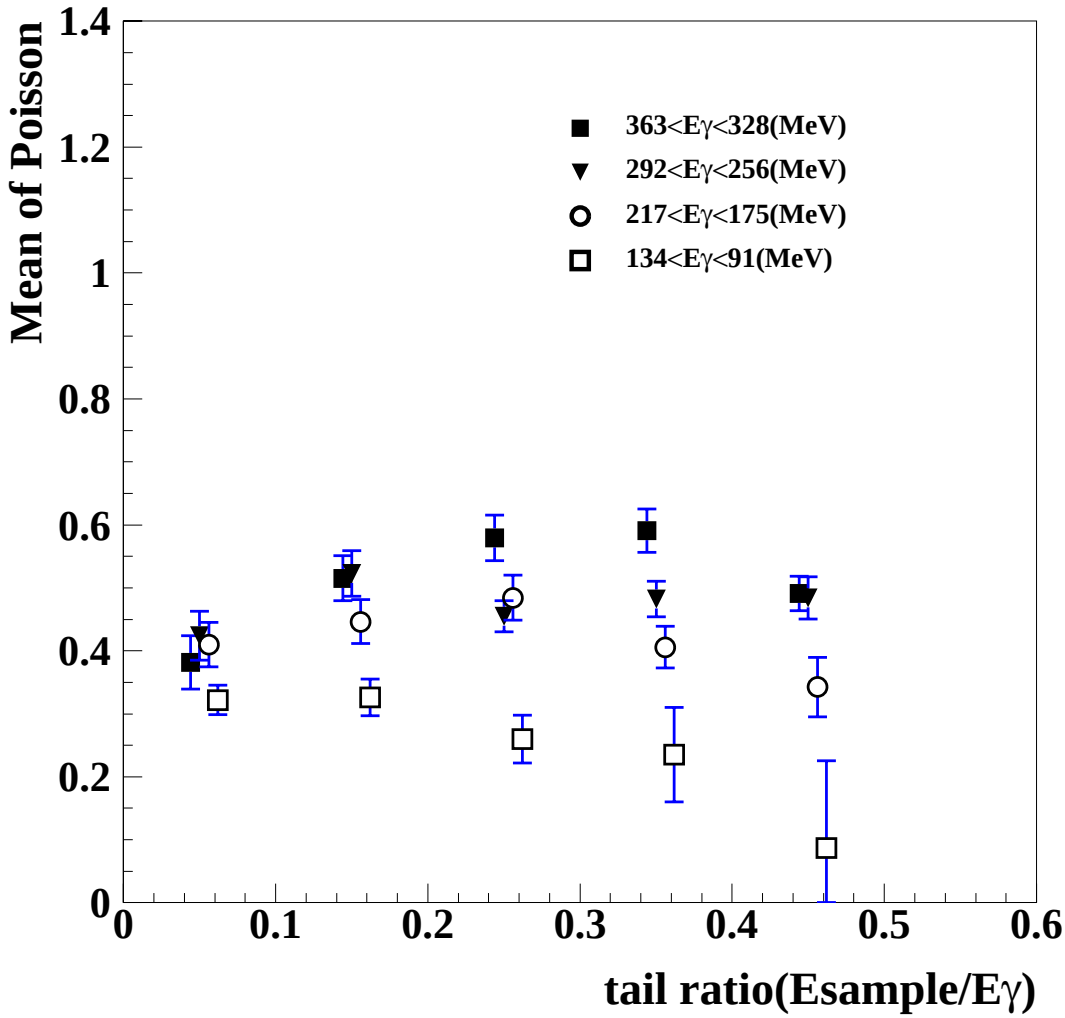

Figure 33: The E_{sample}/E_{γ} dependence of the mean value of a Poisson distribution with the $m_{LS} \geq 1$ for the KEK-CsI calorimeter in the 500 MeV run.

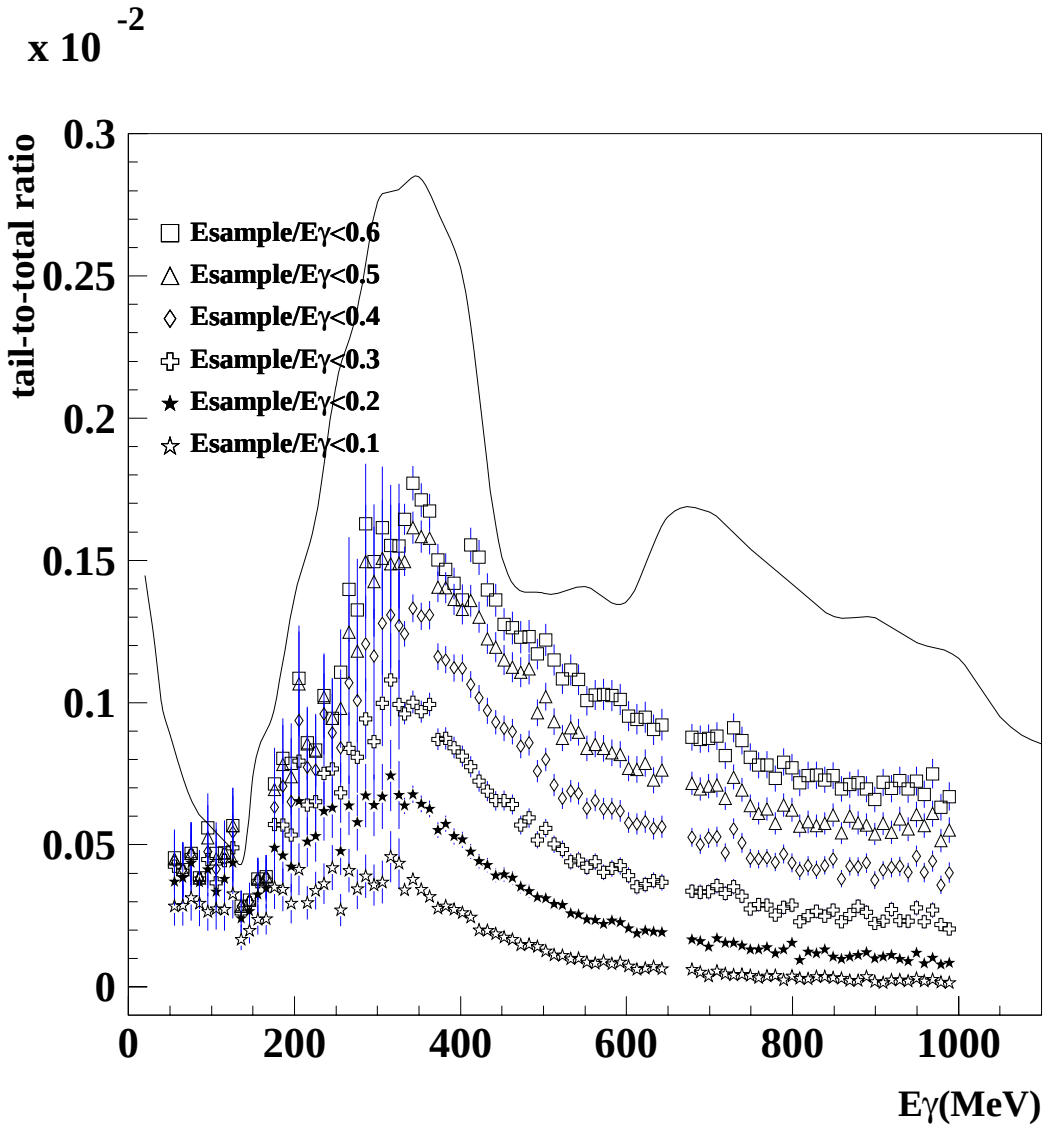

Figure 34: The comparison a tail-to-total ration for the 1mm-Pb/3mm-Scinti calorimter with the ratio of cross sections between the photonuclear and electromagnetic cascasd shower. It notes that the number of tail events(tail$\geq$ 0.4) in region below 230 MeV is suppressed by a trigger as shown in Figures 40, 41 and 42.

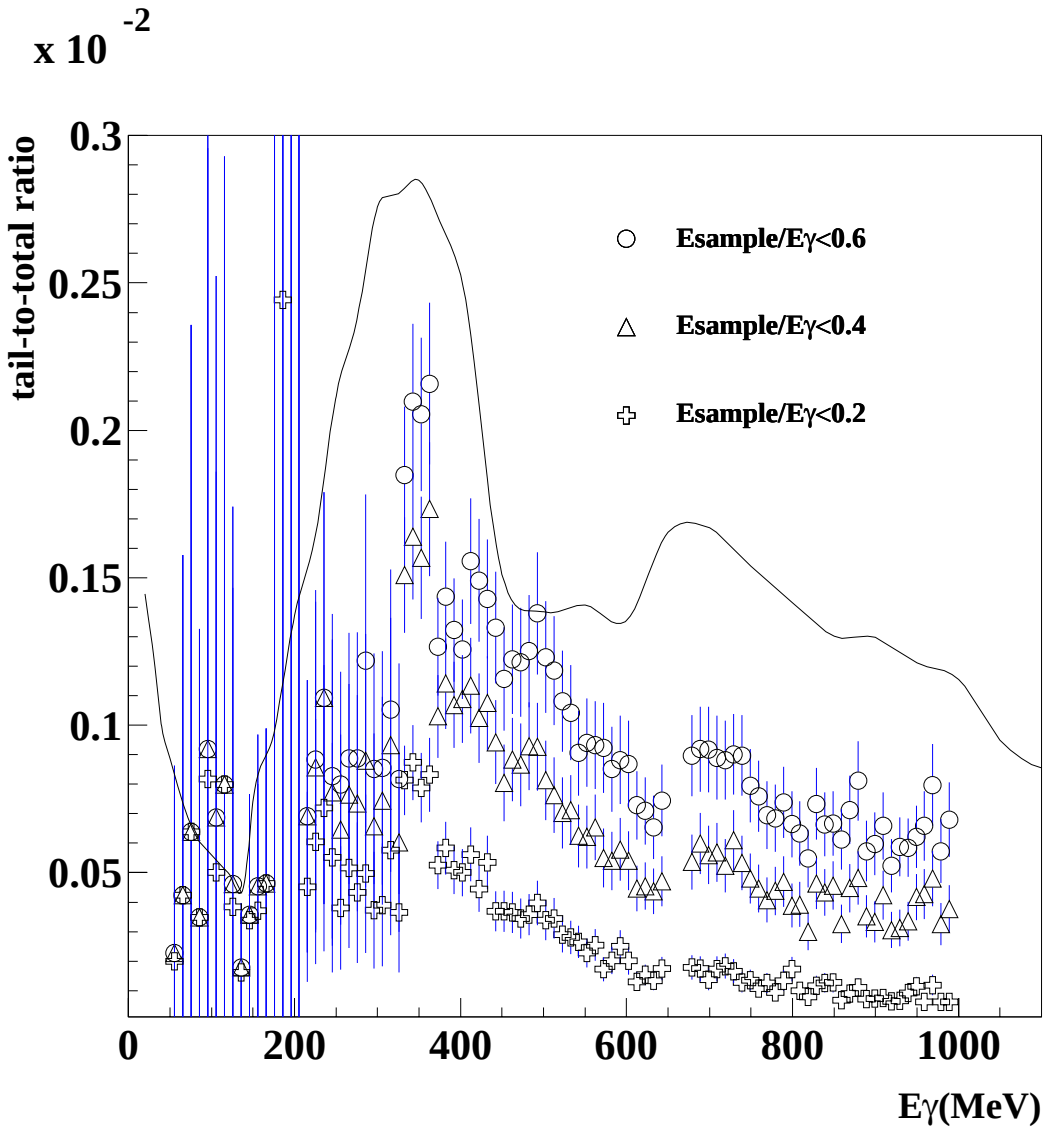

Figure 35: The comparison tail-to-total ratio for the $m_{LS} \geq 2$ with a cross section ratio for the 1mm-Pb/3mm-Scinti calorimeter.

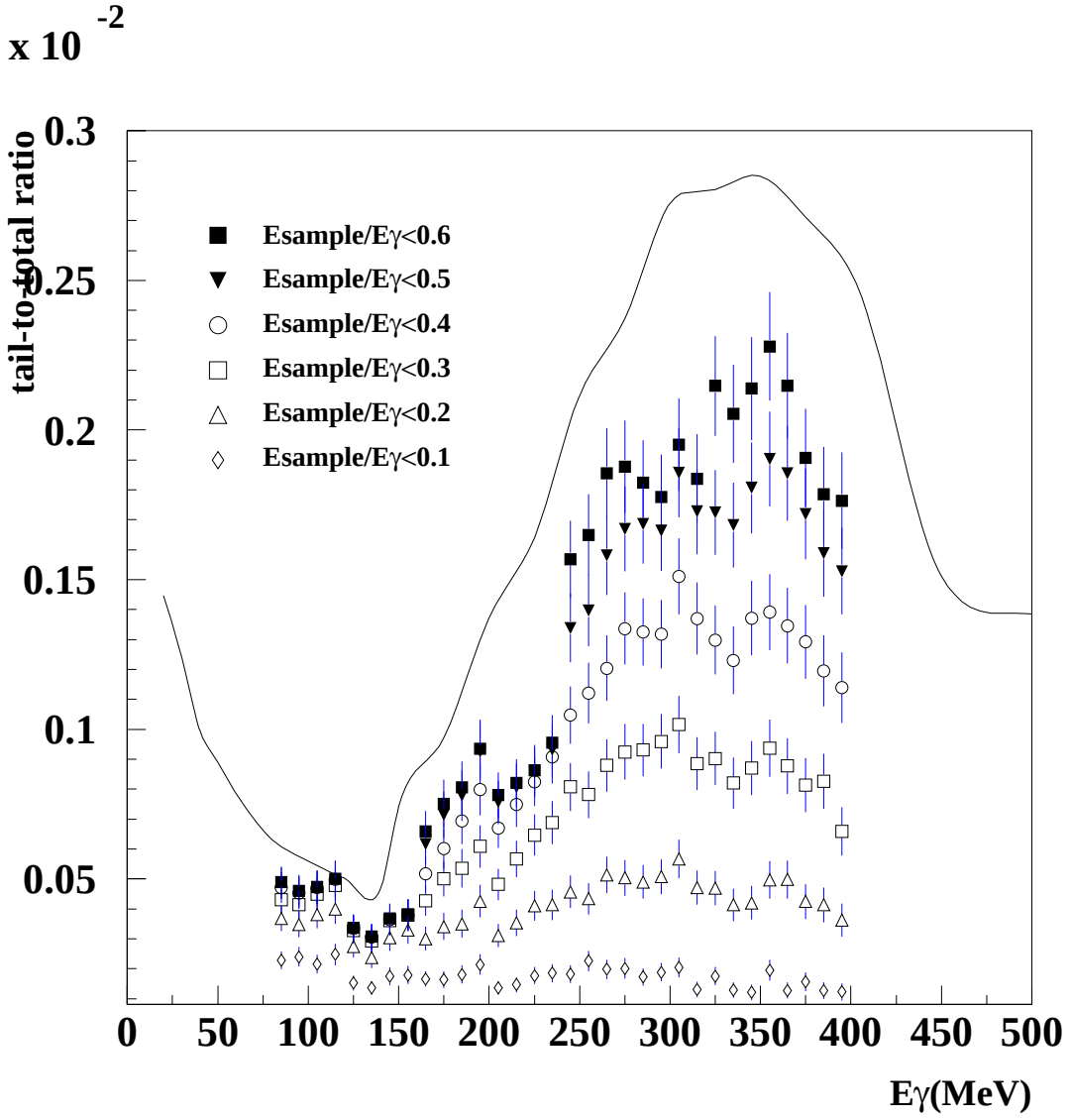

Figure 36: The comparison a tail-to-total ratio with a cross section ratio for the KEK-CsI calorimeter. It notes that the number of tail events(tail$\geq$ 0.4) in region below 250 MeV is suppressed by a trigger as shown in Figure 43.

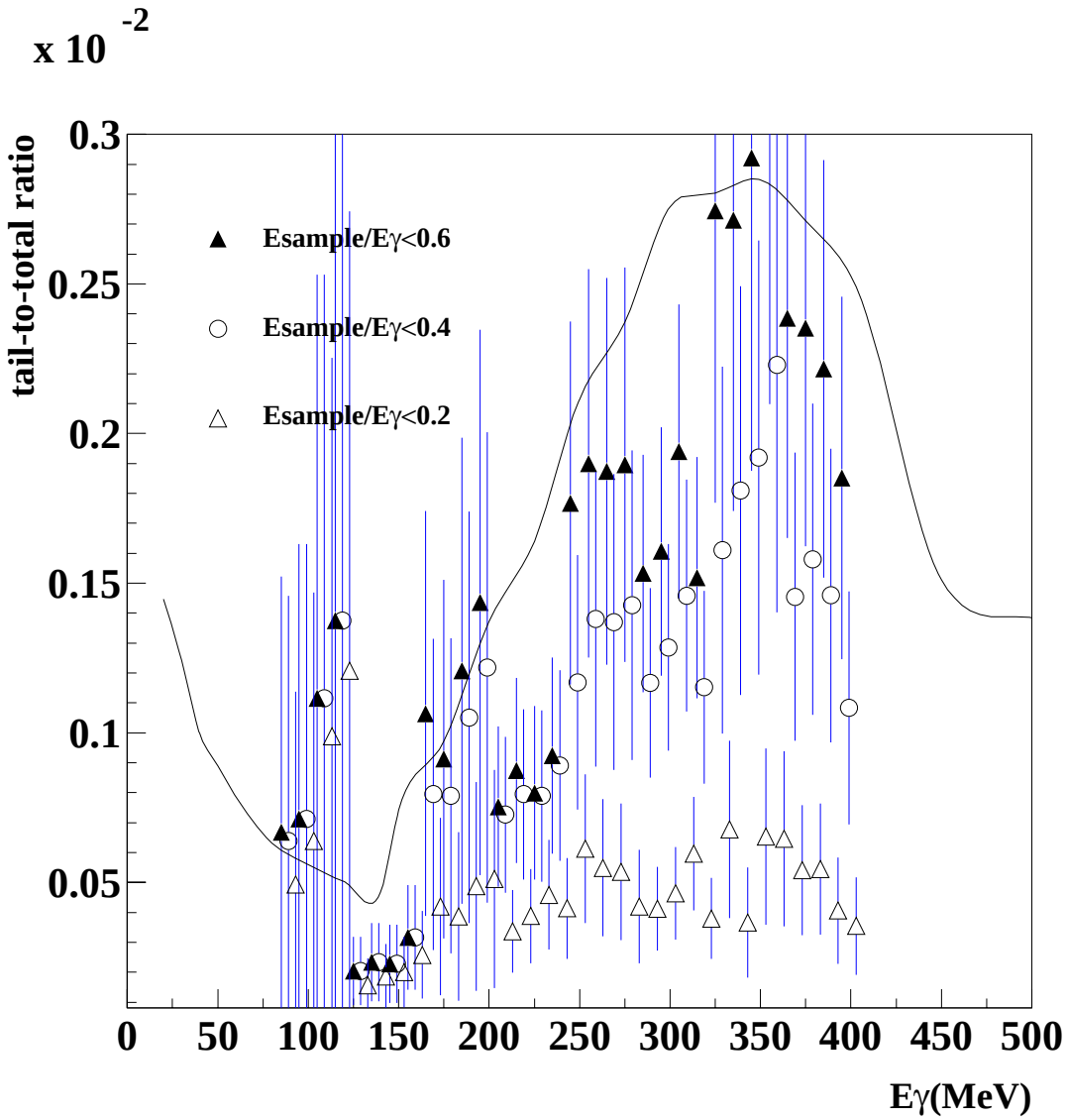

Figure 37: The comparison tail-to-total ratio for the $m_{LS} \geq 2$ with a cross section ratio for the 1mm-Pb/3mm-Scinti calorimeter.

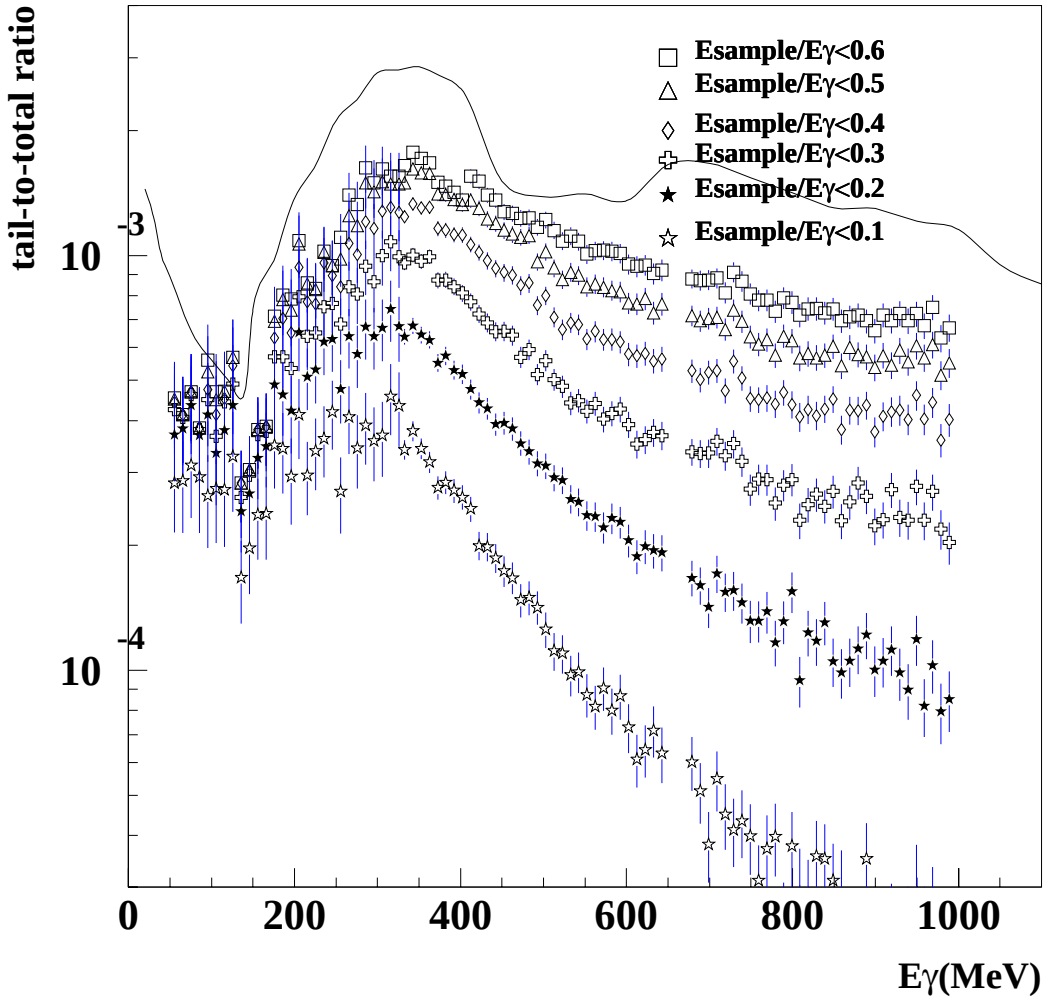

Figure 38: The tail-to-total ration in log scale. The conditions are same as Figure 34.

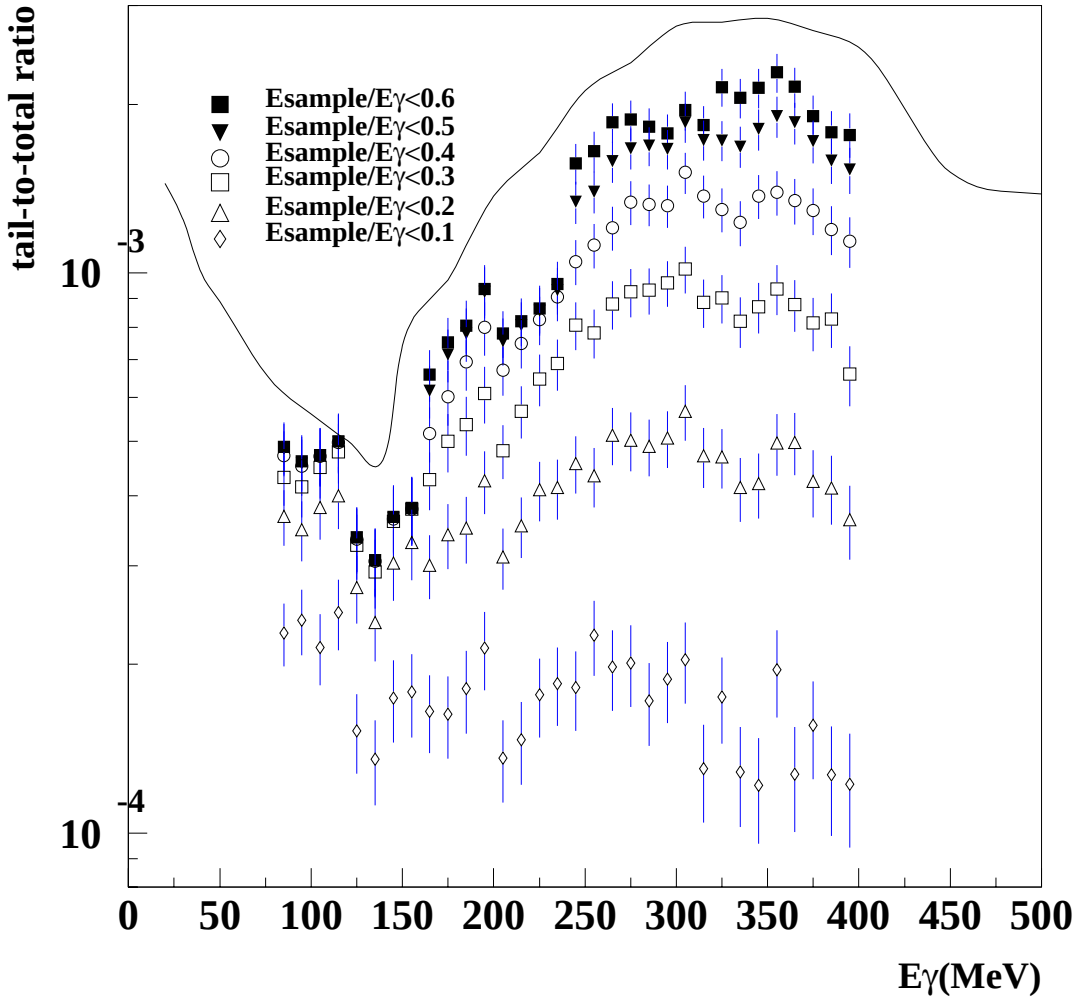

Figure 39: The tail-to-total ration in log scale. The conditions are same as Figure 36.

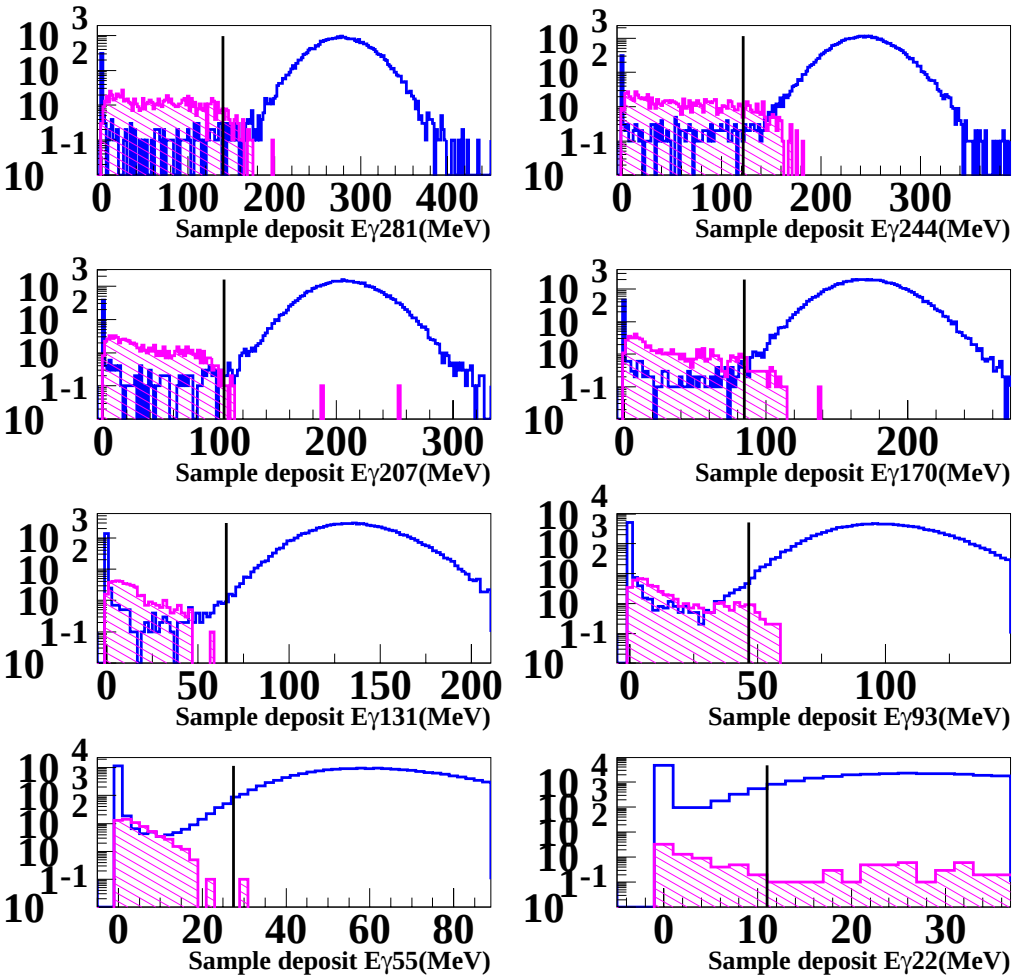

Figure 40: The distribution of the sample energy deposit for the 1mm-Pb/3mm-Scinti 430 MeV-run in both conditions of the Tag-Σ trigger and $\overline{EG}trigger$(diagonal histogram). The line indicates a boundary of $E_{sample}/E_{\gamma} = 0.5$.

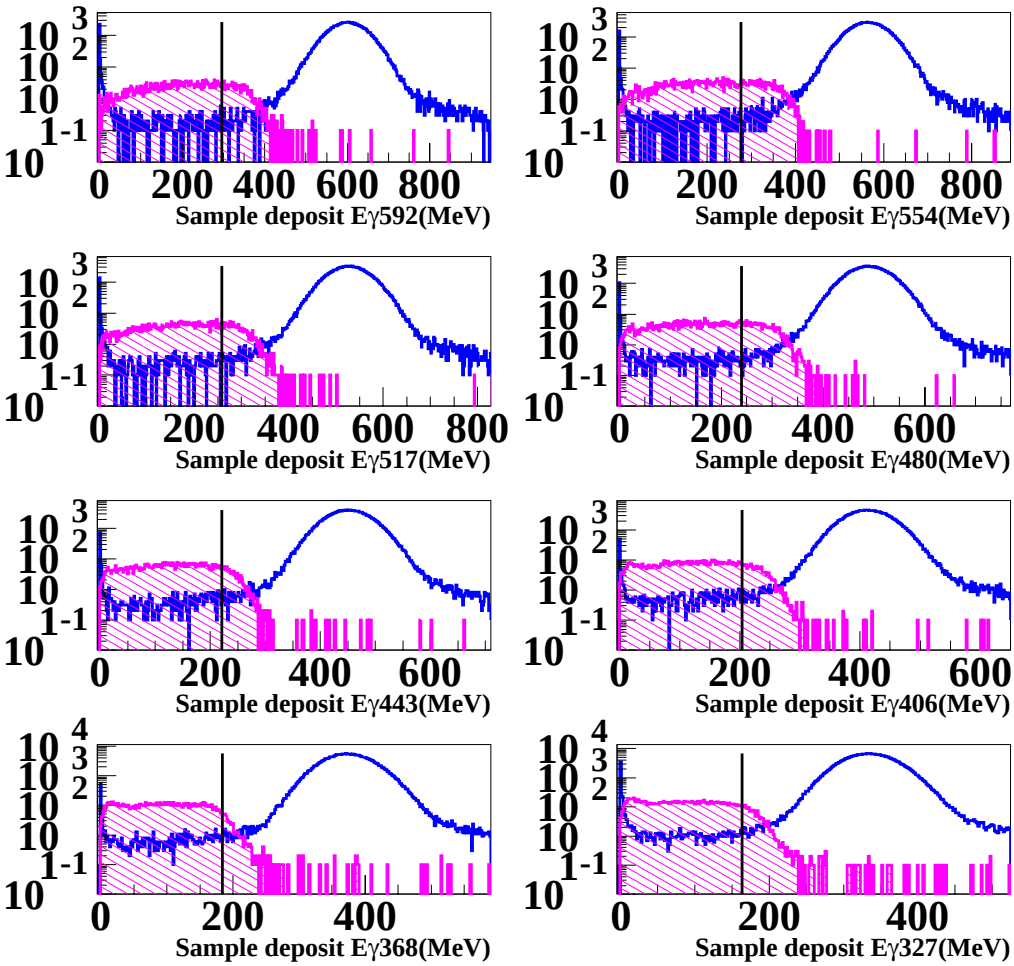

Figure 41: The distribution of the sample energy deposit for the 1mm-Pb/3mm-Scinti 750 MeV-run in both conditions of the Tag-Σ trigger and $\overline{EG}trigger$(diagonal histogram). The line indicates a boundary of $E_{sample}/E_{\gamma} = 0.5$.

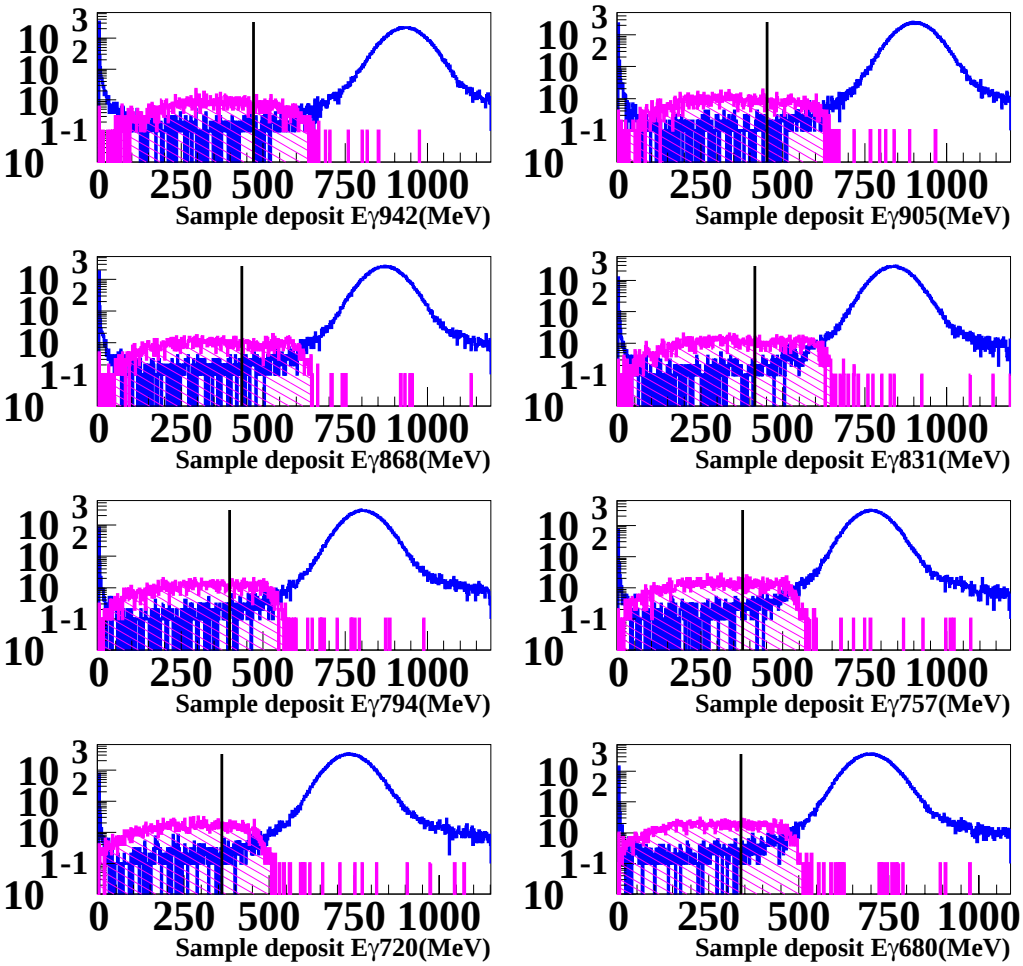

Figure 42: The distribution of the sample energy deposit for the 1mm-Pb/3mm-Scinti 1100 MeV-run in both conditions of the Tag-Σ trigger and $\overline{EG}trigger$(diagonal histogram). The line indicates a boundary of $E_{sample}/E_{\gamma} = 0.5$.

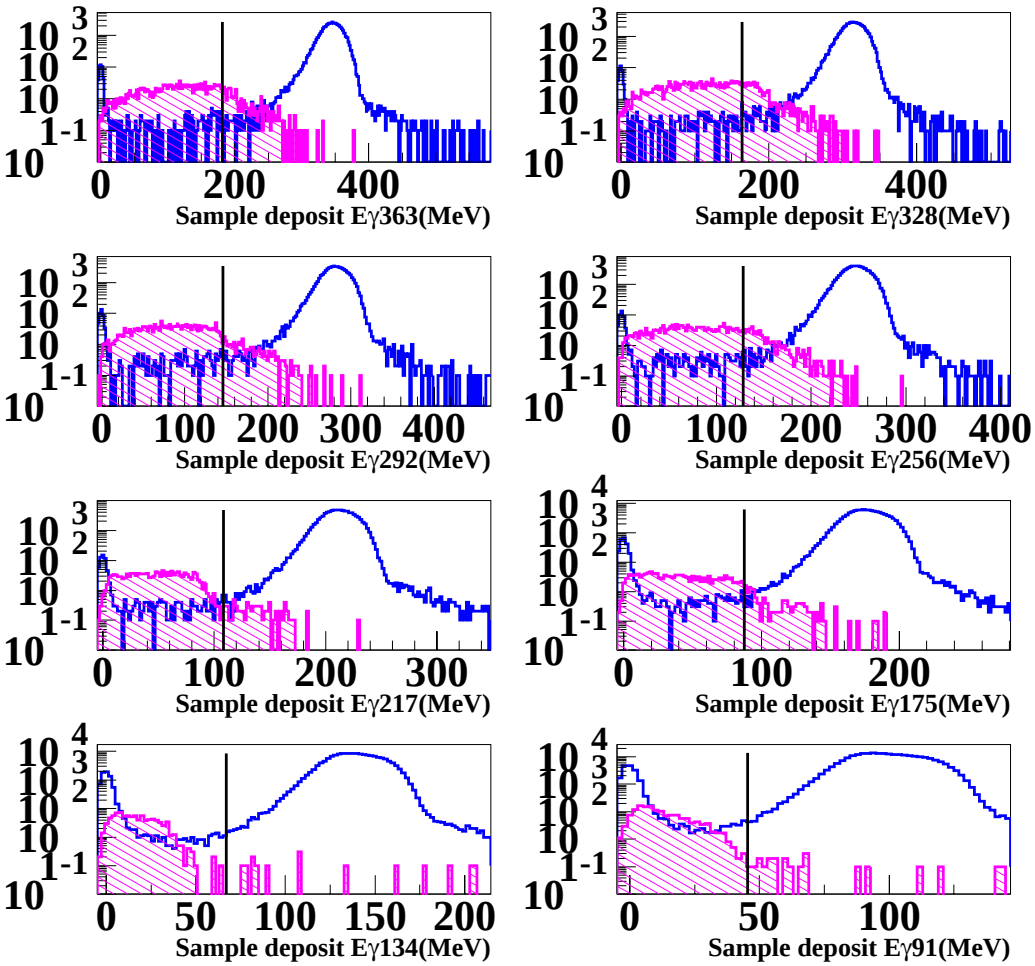

Figure 43: The distribution of the sample energy deposit for the KEK-CsI calorimeter in both conditions of the Tag-Σ trigger and $\overline{EG}trigger$(diagonal histogram). The line indicates a boundary of $E_{sample}/E_{\gamma} = 0.5$.

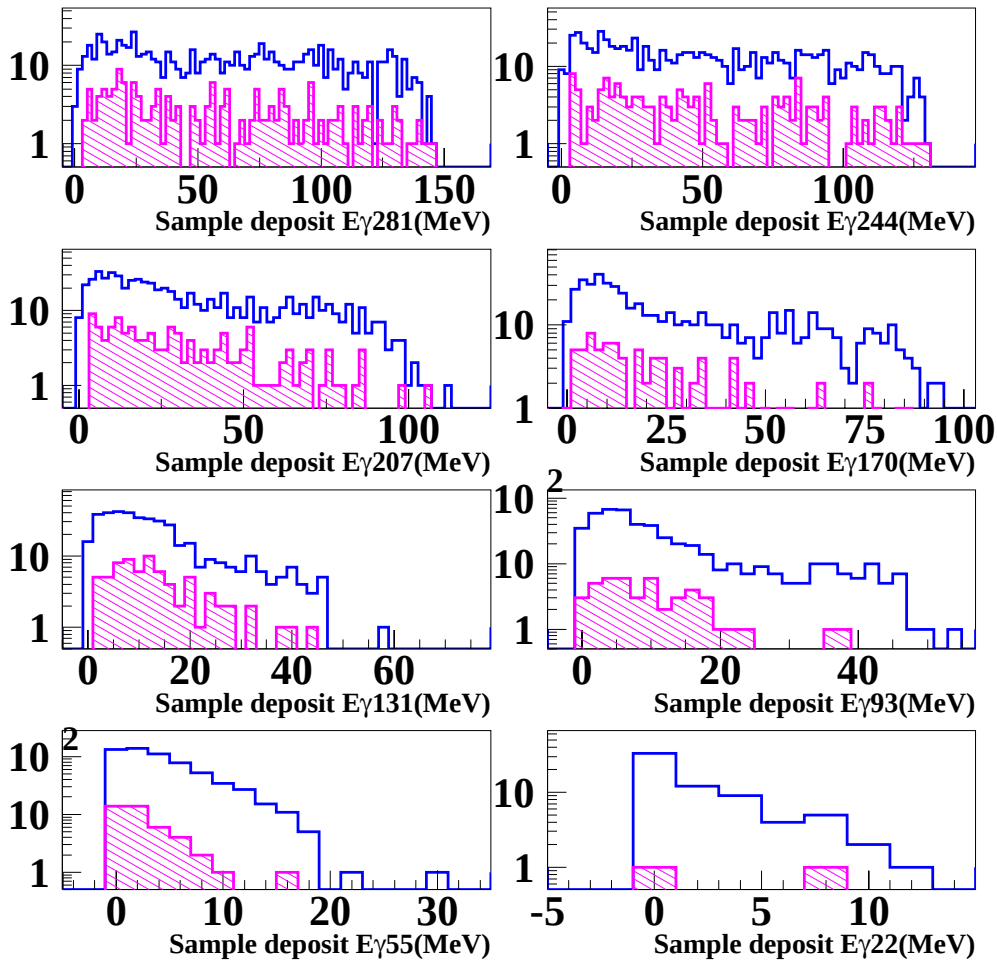

Figure 44: The distribution of the sample energy deposit with a requirement of $m_{LS} \geq 2$(diagonal histogram) and that of $m_{LS} \geq 1$ for the 1mm-Pb/3mm-Scinti calorimeter in the 430 MeV run.

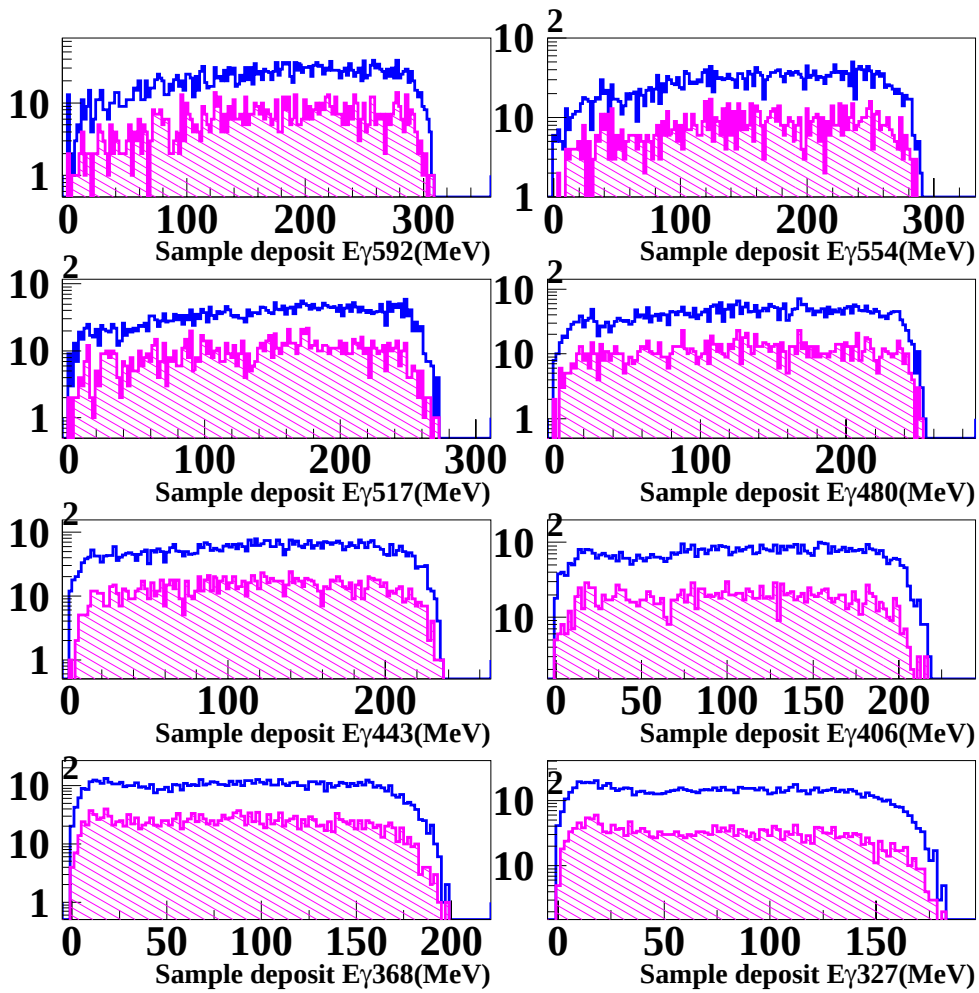

Figure 45: The distribution of the sample energy deposit with a requirement $m_{LS} \geq 2$(diagonal histogram) and that of $m_{LS} \geq 1$ for the 1mm-Pb/3mm-Scinti calorimeter in the 750 MeV run.

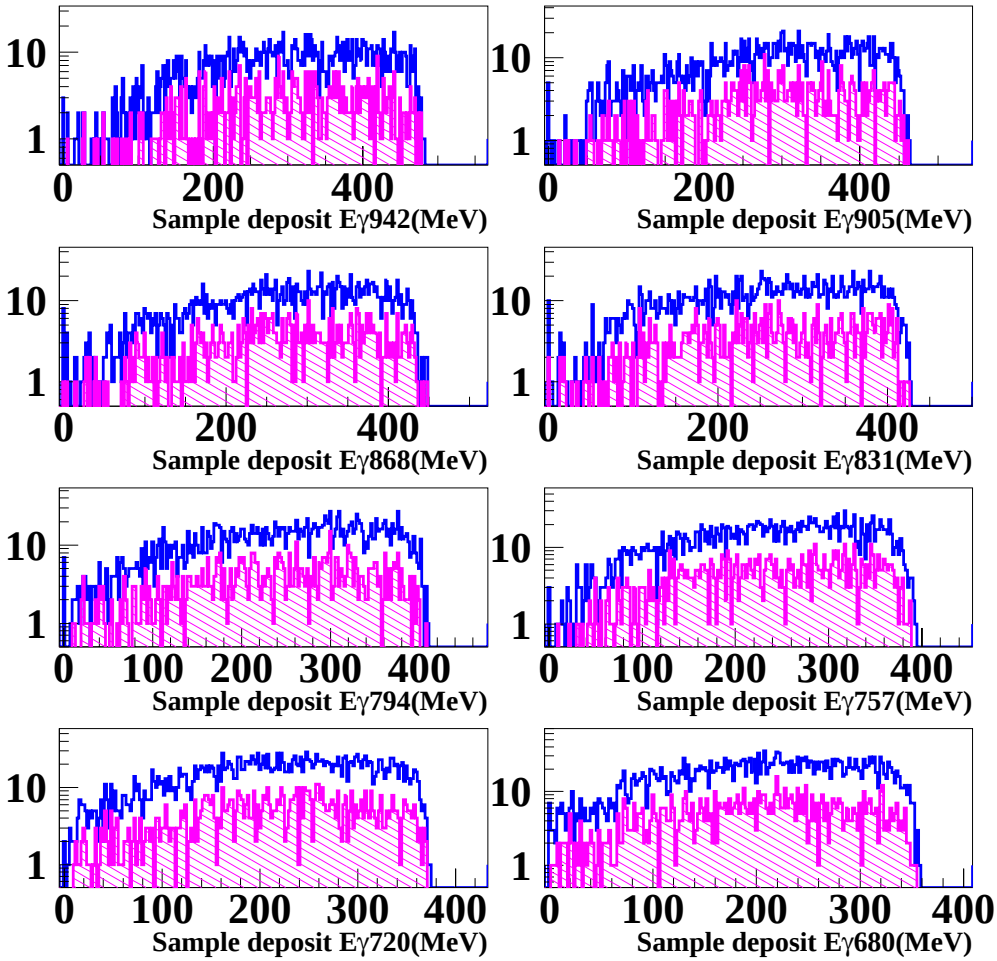

Figure 46: The distribution of the sample energy deposit with a requirement of $m_{LS} \geq 2$(diagonal histogram) and that of $m_{LS} \geq 1$ for the 1mm-Pb/3mm-Scinti calorimeter in the 1100 MeV run.

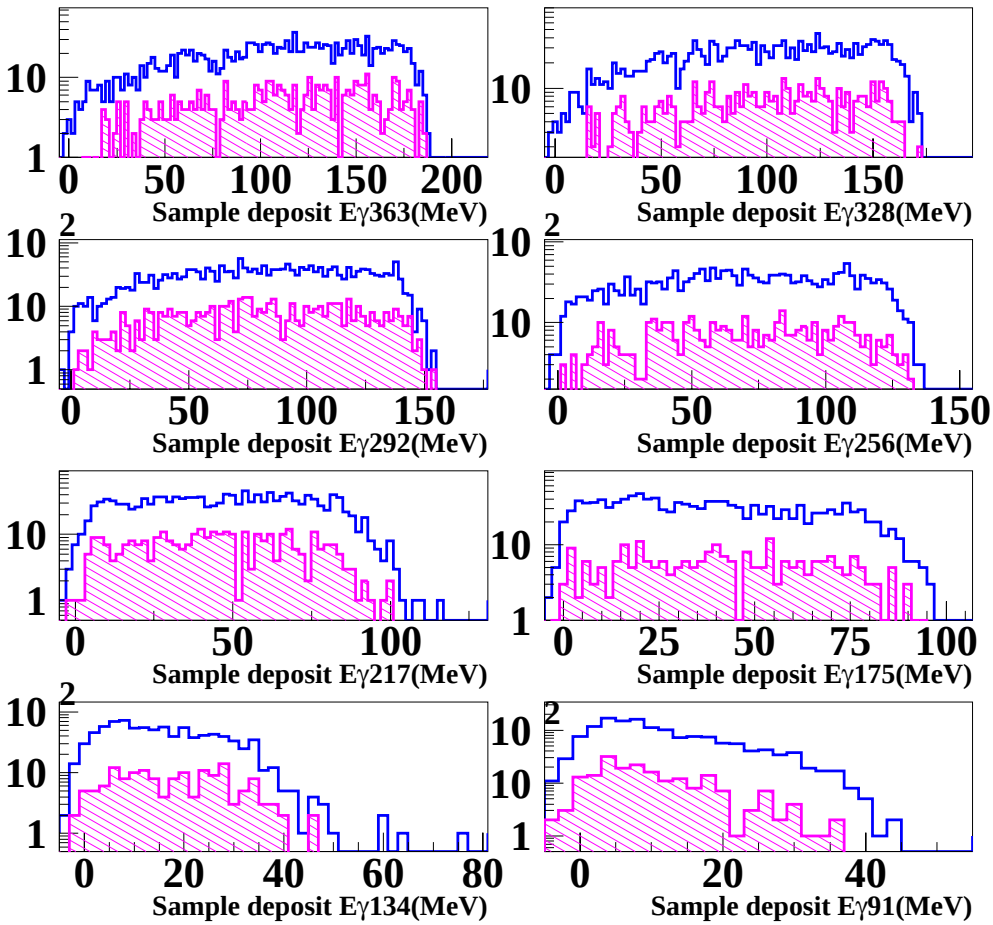

Figure 47: The distribution of sample energy deposit with a requirement of $m_{LS} \geq 2$(diagonal histogram) and that of $m_{LS} \geq 1$ for the KEK-CsI calorimeter in the 500 MeV run.

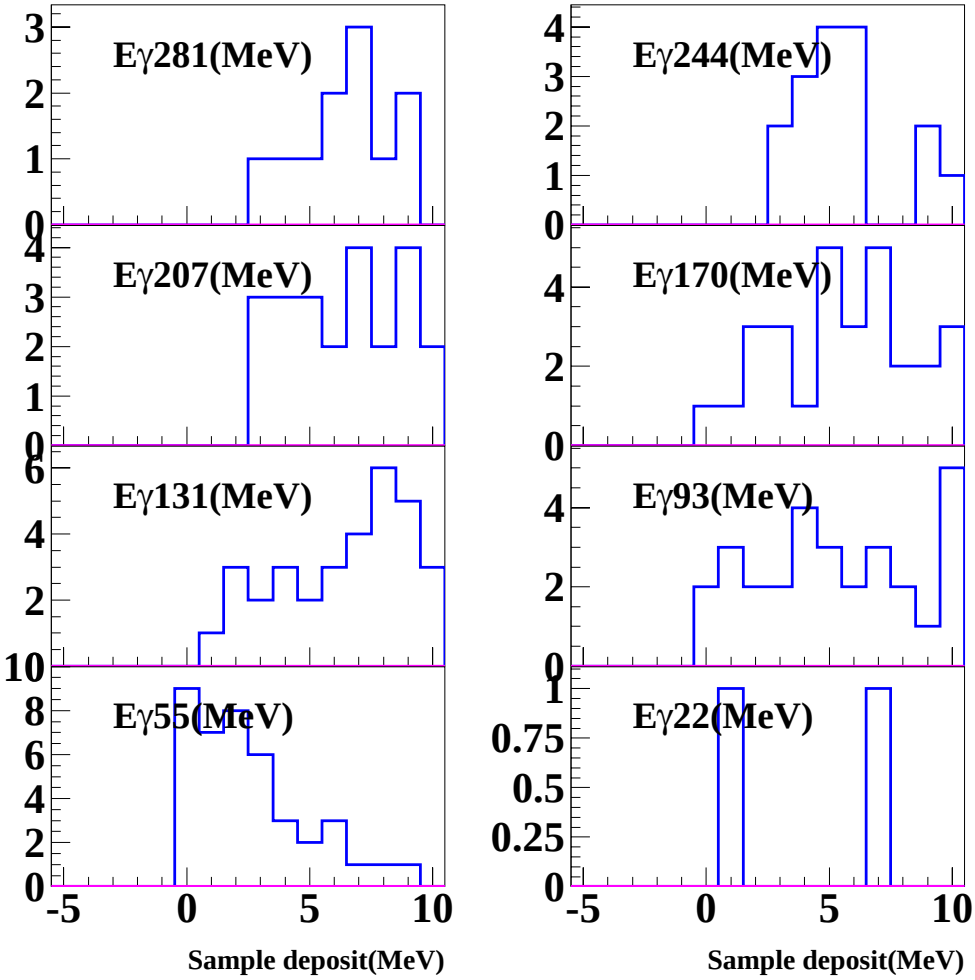

Figure 48: The distribution of the sample energy deposit with a requirement of $m_{LS} \geq 2$ below 10 MeV for the 1mm-Pb/3mm-Scinti calorimeter in the 430 MeV run. A diagonal histogram is the event of off-timing.

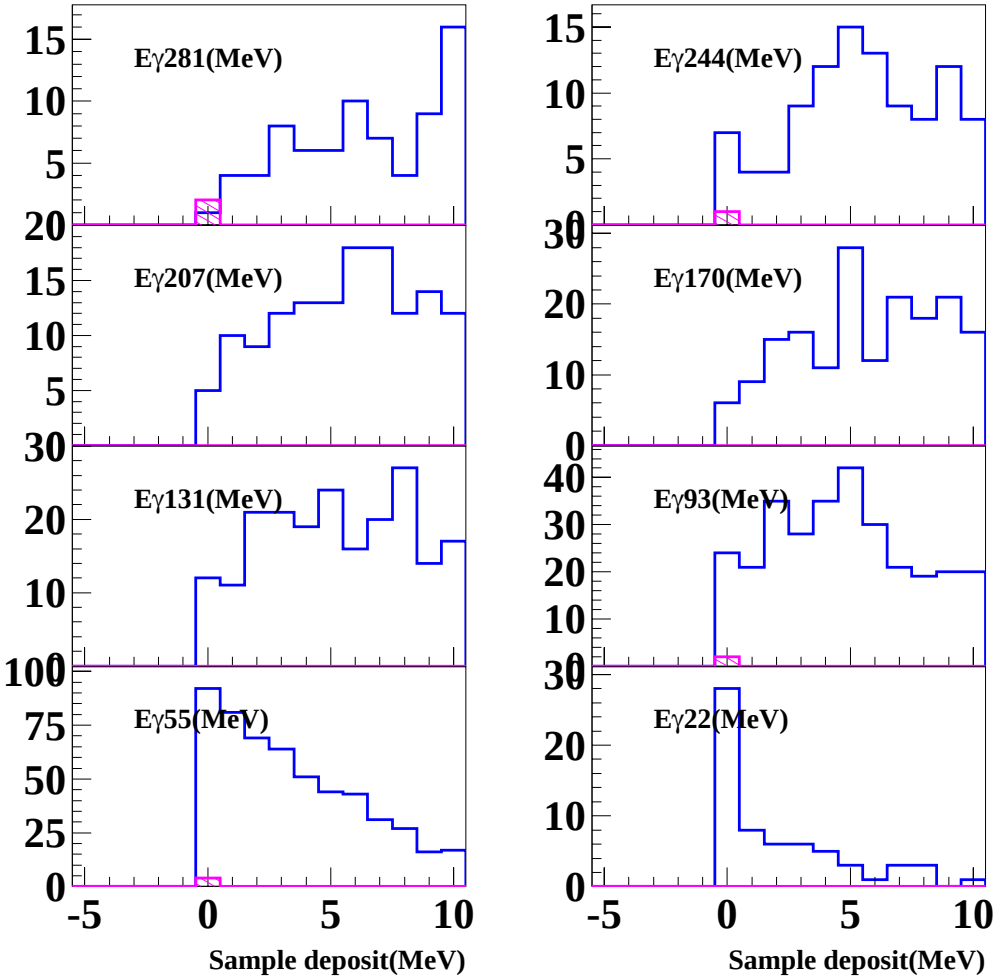

Figure 49: The distribution of the sample energy deposit with a requirement of $m_{LS} \geq 1$ below 10 MeV for the 1mm-Pb/3mm-Scinti calorimeter in the 430 MeV run. A diagonal histogram is the event of off-timing.

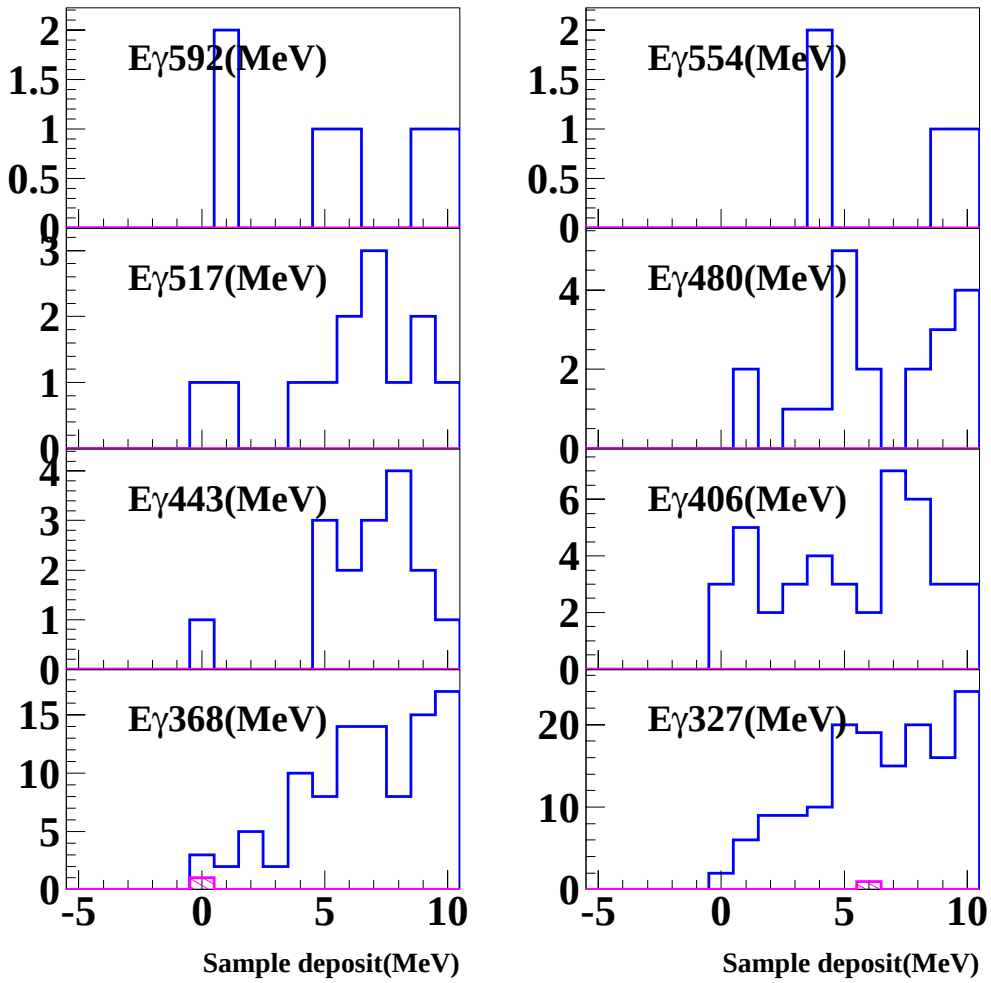

Figure 50: The distribution of the sample energy deposit with a requirement of $m_{LS} \geq 2$ below 10 MeV for the 1mm-Pb/3mm-Scinti calorimeter in the 750 MeV run. A diagonal histogram is the event of off-timing.

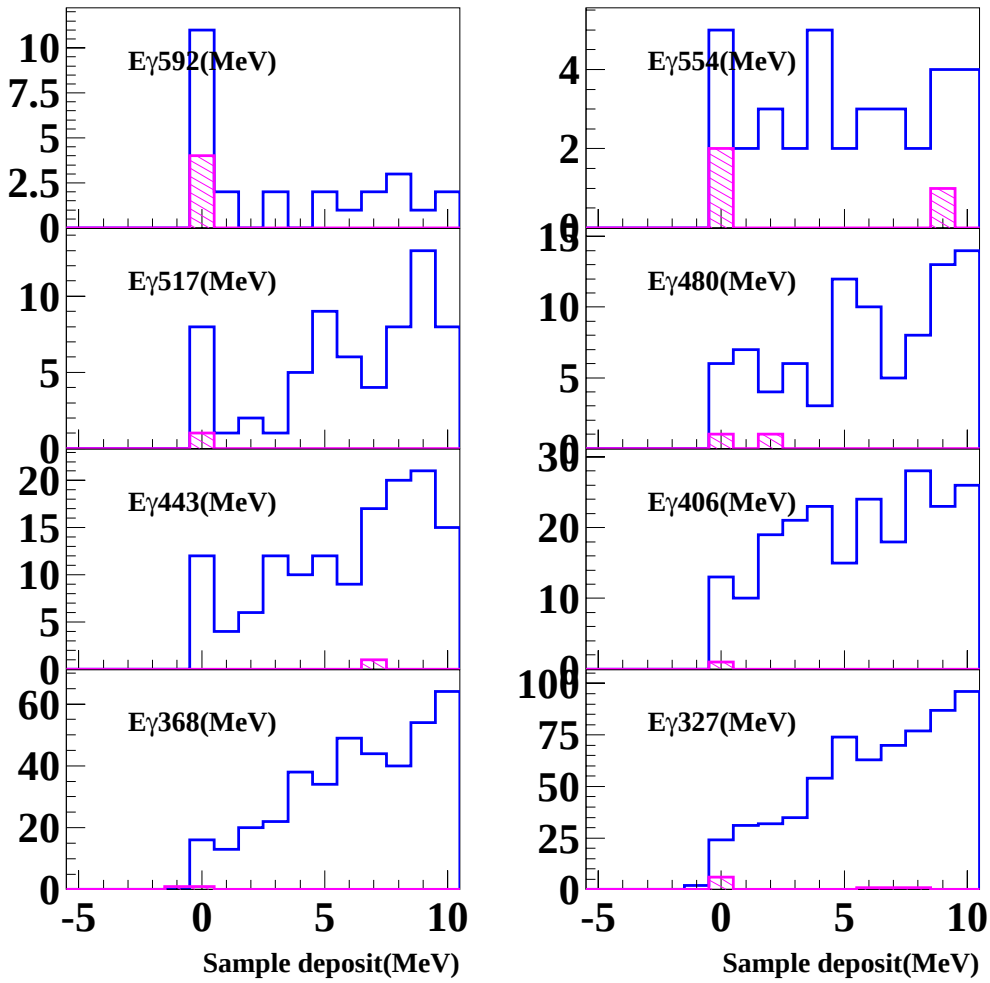

Figure 51: The distribution of the sample energy deposit with a requirement of $m_{LS} \geq 1$ below 10 MeV for the 1mm-Pb/3mm-Scinti calorimeter in the 750 MeV run. A diagonal histogram is the event of off-timing.

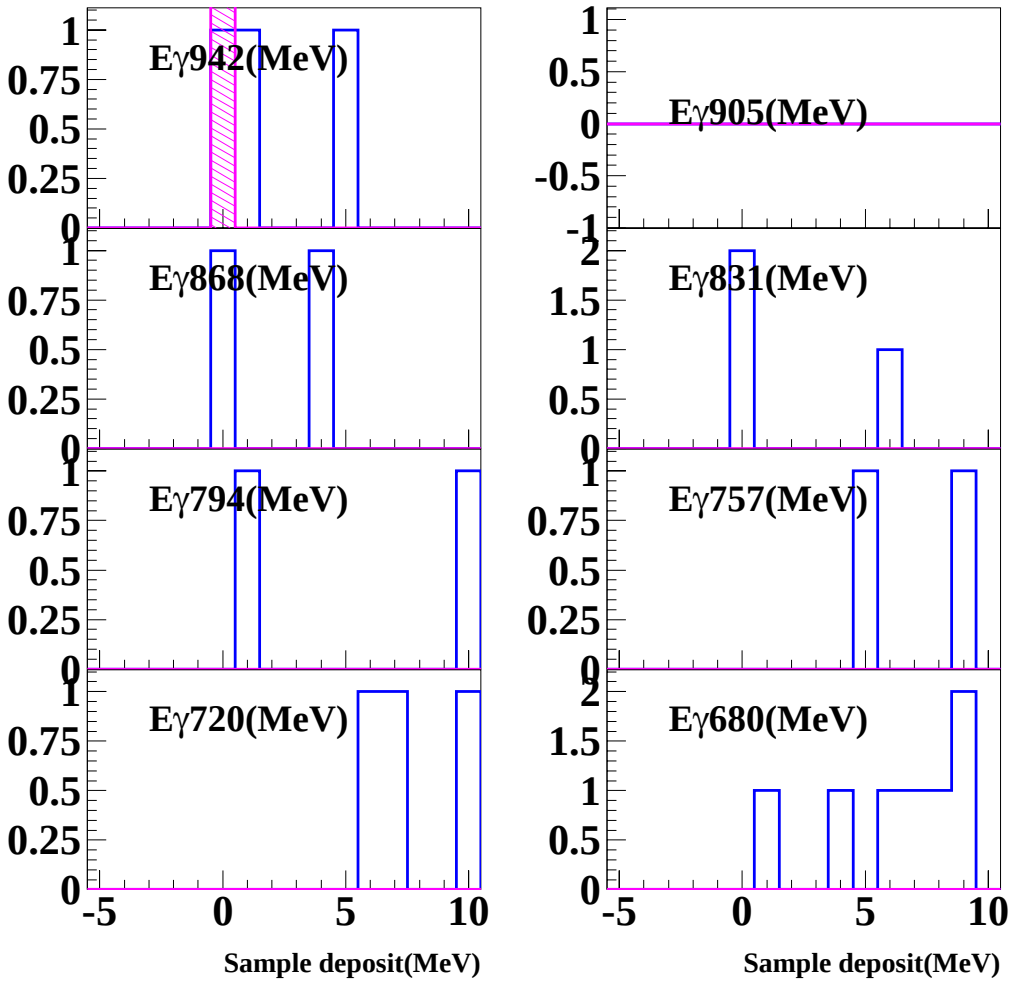

Figure 52: The distribution of the sample energy deposit with a requirement of $m_{LS} \geq 2$ below 10 MeV for the 1mm-Pb/3mm-Scinti calorimeter in the 1100 MeV run. A diagonal histogram is the event of off-timing.

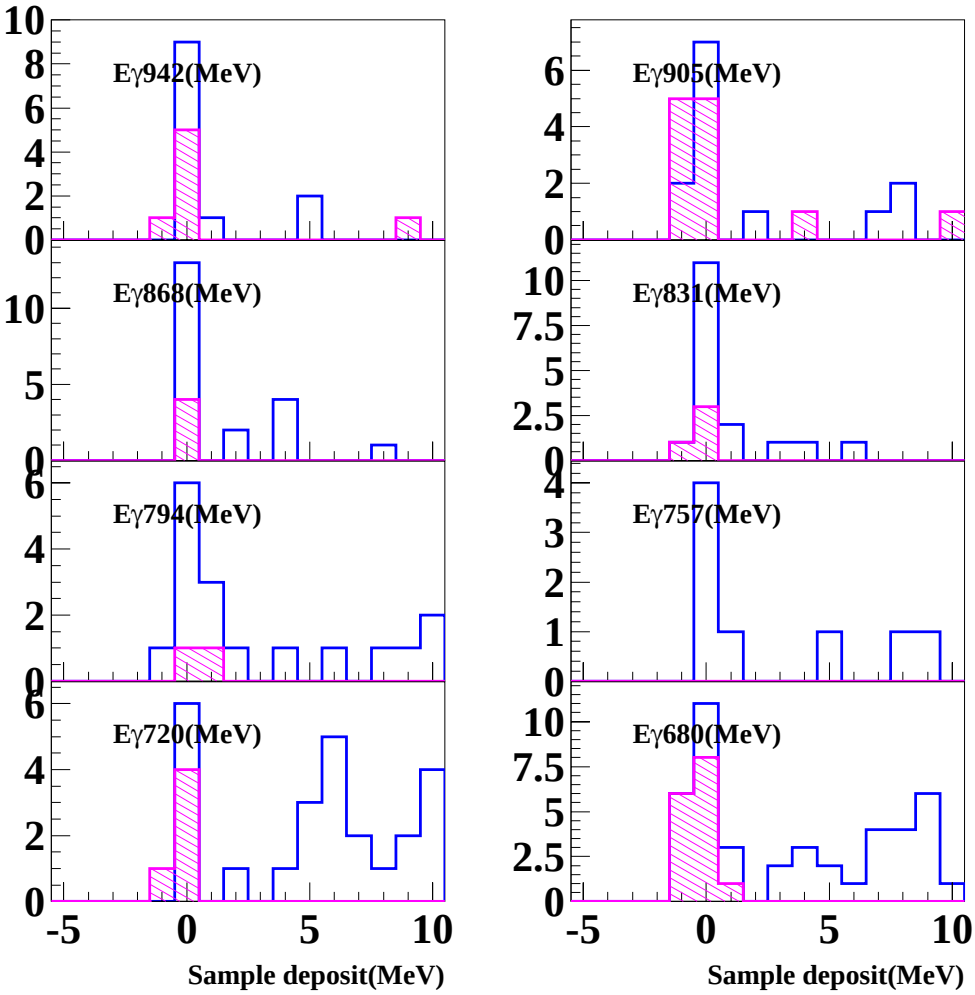

Figure 53: The distribution of the sample energy deposit with a requirement of $m_{LS} \geq 1$ below 10 MeV for the 1mm-Pb/3mm-Scinti calorimeter in the 1100 MeV run. It has the enhancement at 0 MeV clearly. A diagonal histogram is the event of off-timing.

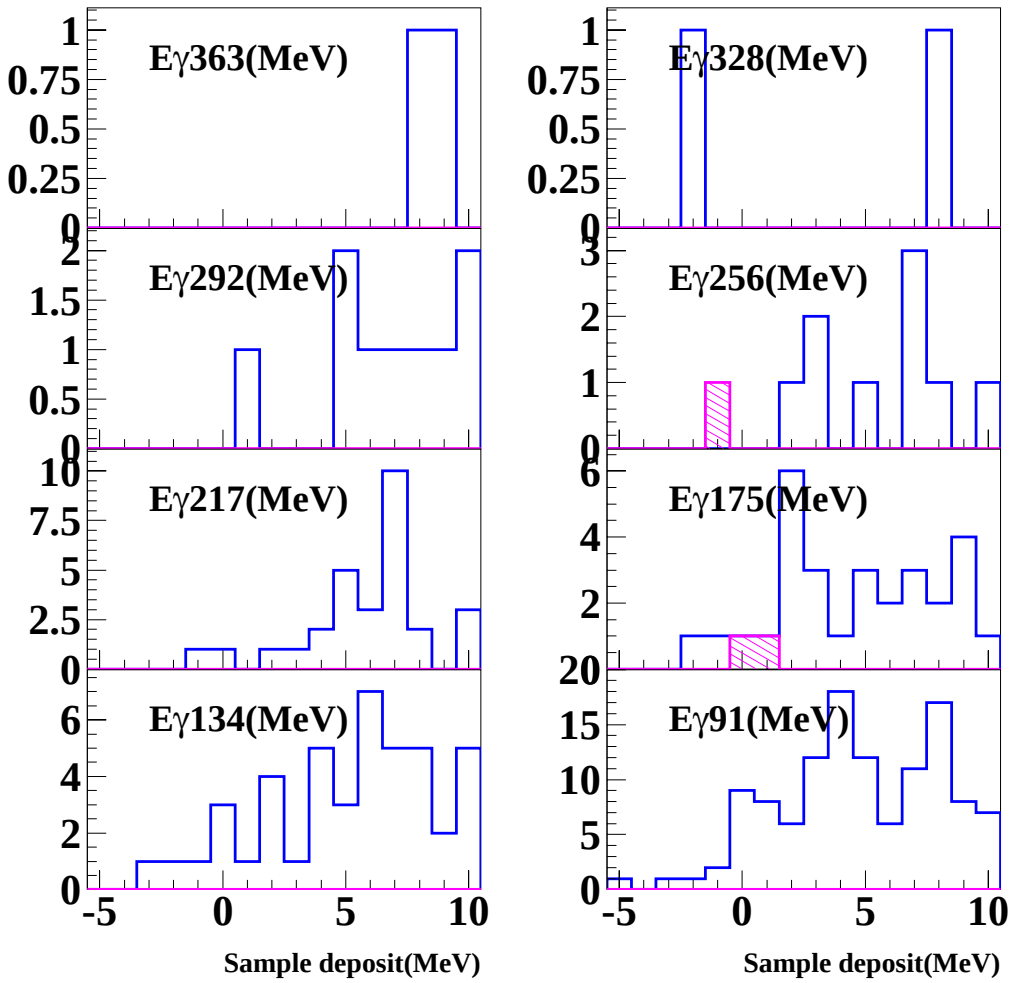

Figure 54: The distribution of the sample energy deposit with a requirement of $m_{LS} \geq 2$ below 10 MeV for the KEK-CsI calorimeter in the 500 MeV run. A diagonal histogram is the event of off-timing.

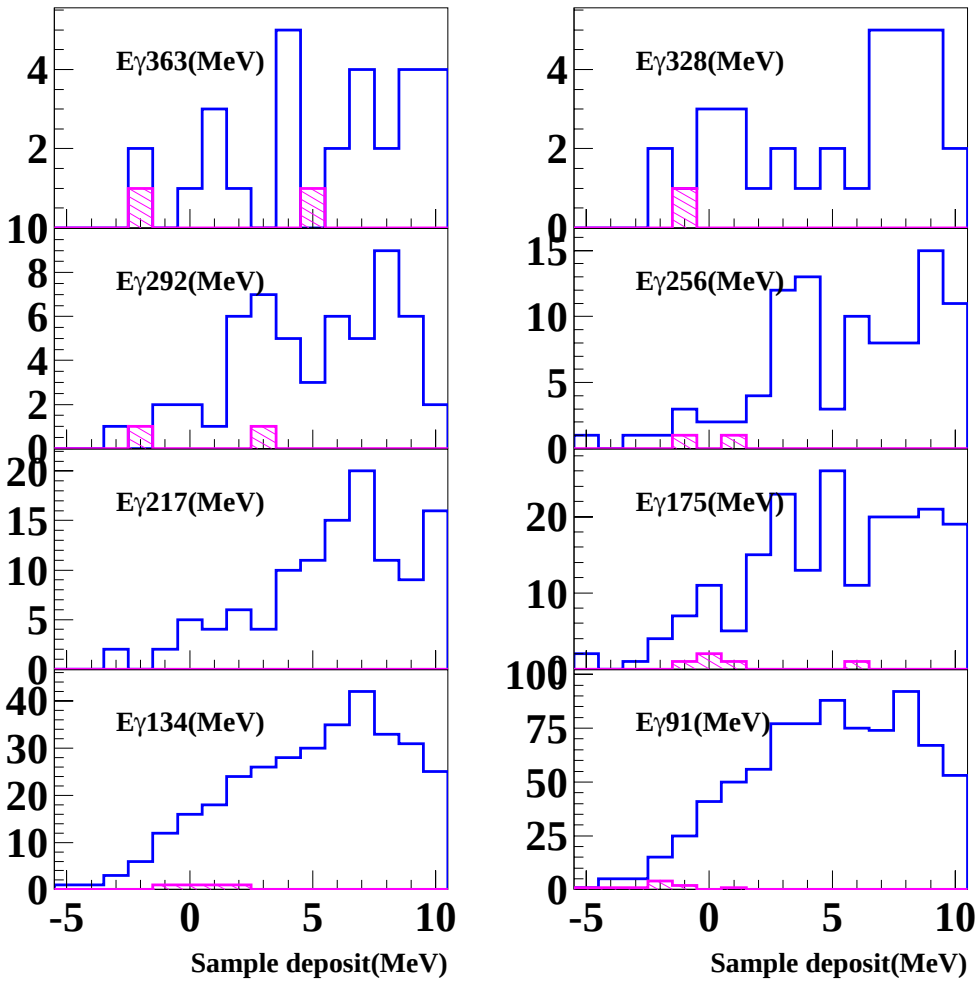

Figure 55: The distribution of the sample energy deposit with a requirement of $m_{LS} \geq 2$ below 10 MeV for the KEK-CsI calorimeter in the 500 MeV run. A diagonal histogram is the event of off-timing.

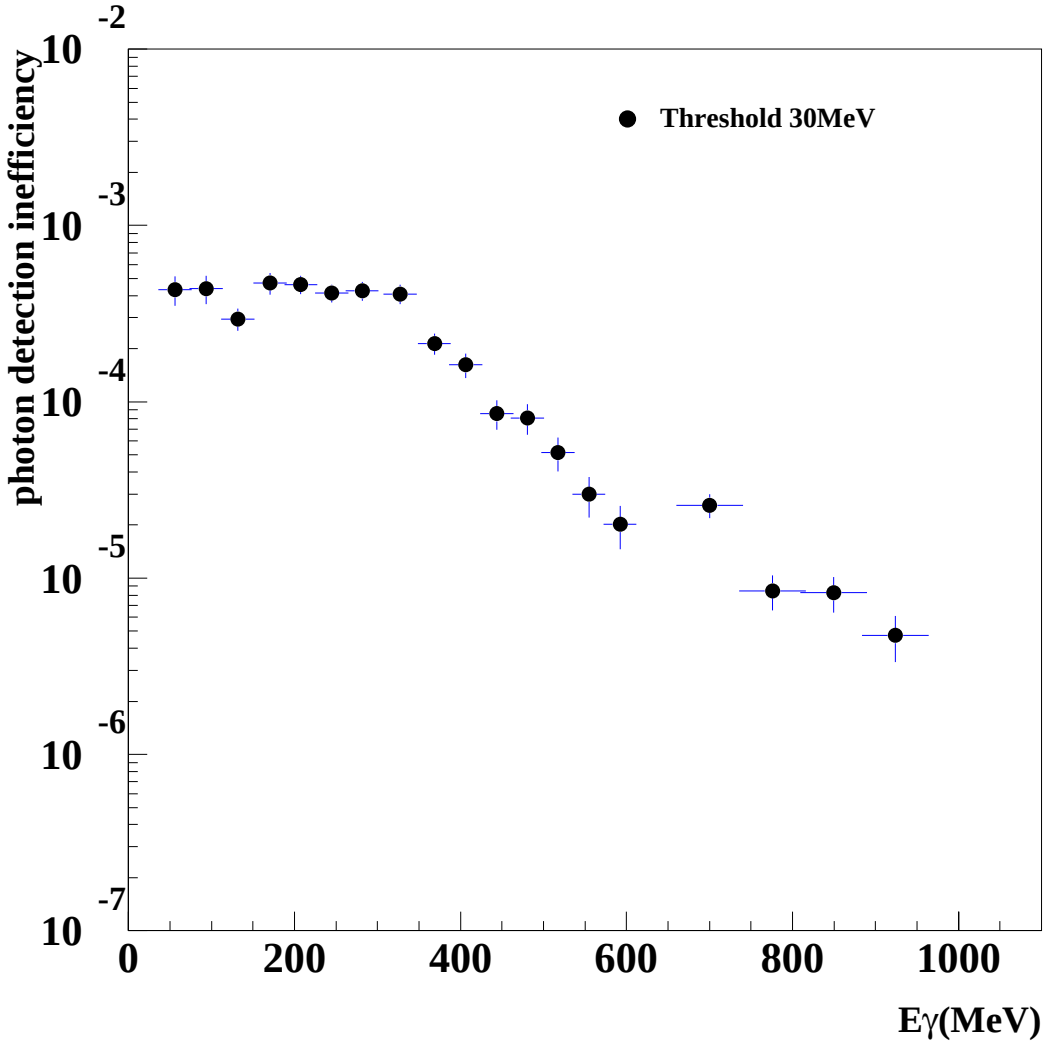

Figure 56: The detection inefficiency due to photonuclear interaction for the 1mm-Pb/3mm-Scinti calorimeter with the principle of the recommendation 1 for the 30 MeV threshold.

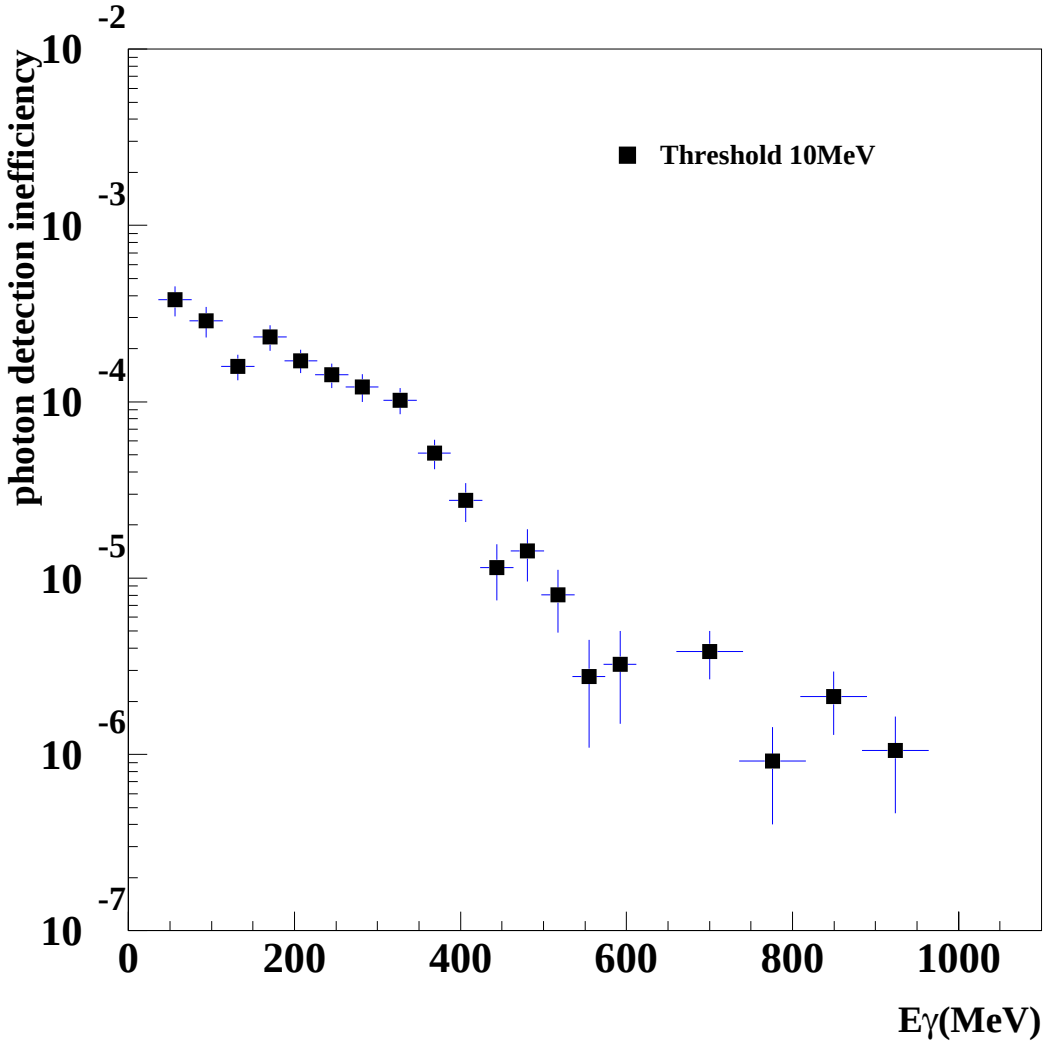

Figure 57: The detection inefficiency due to photonuclear interaction for the 1mm-Pb/3mm-Scinti calorimeter with the principle of the recommendation 1 for the 10 MeV threshold.

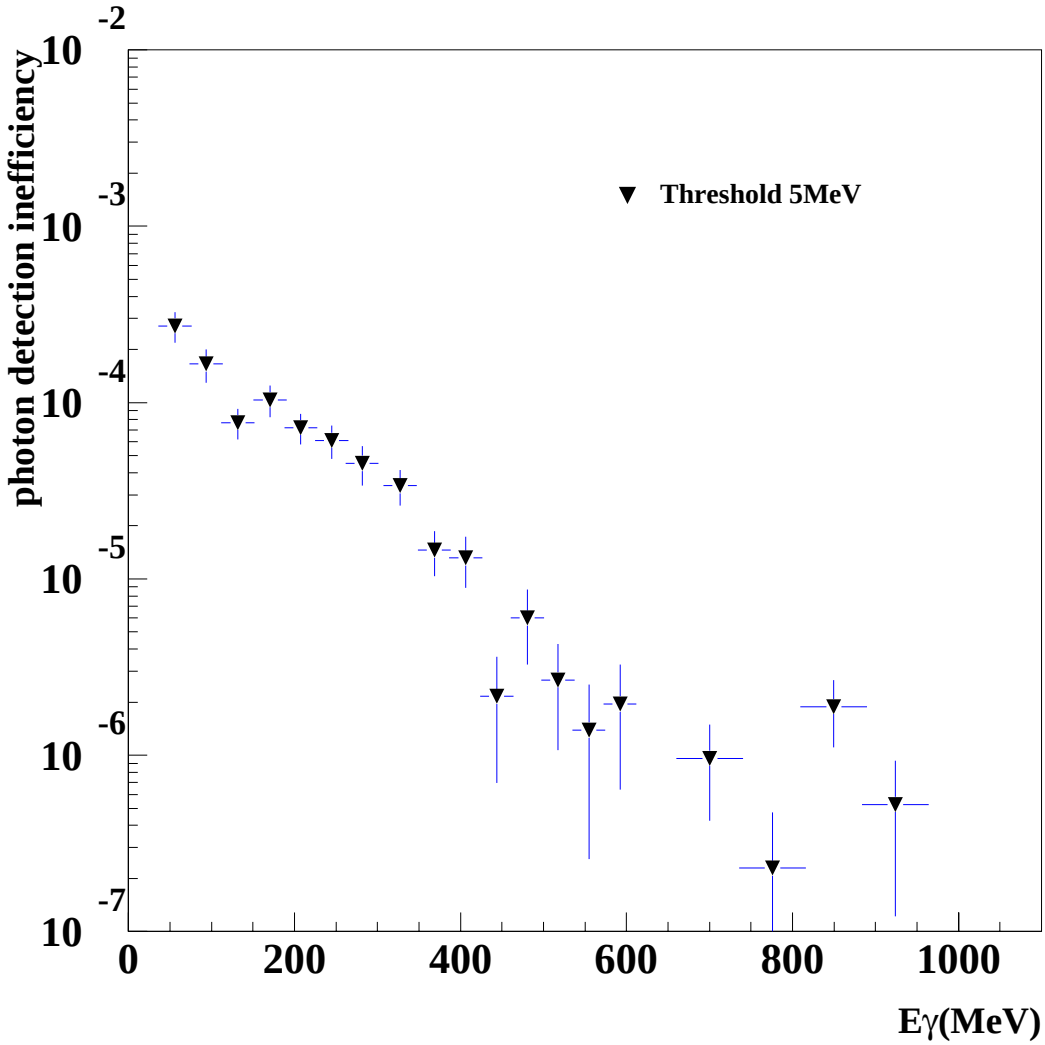

Figure 58: The detection inefficiency due to photonuclear interaction for the 1mm-Pb/3mm-Scinti calorimeter with the principle of the recommendation 1 for the 5 MeV threshold. The arrow indicates the upper limit at the 90% confidence level.

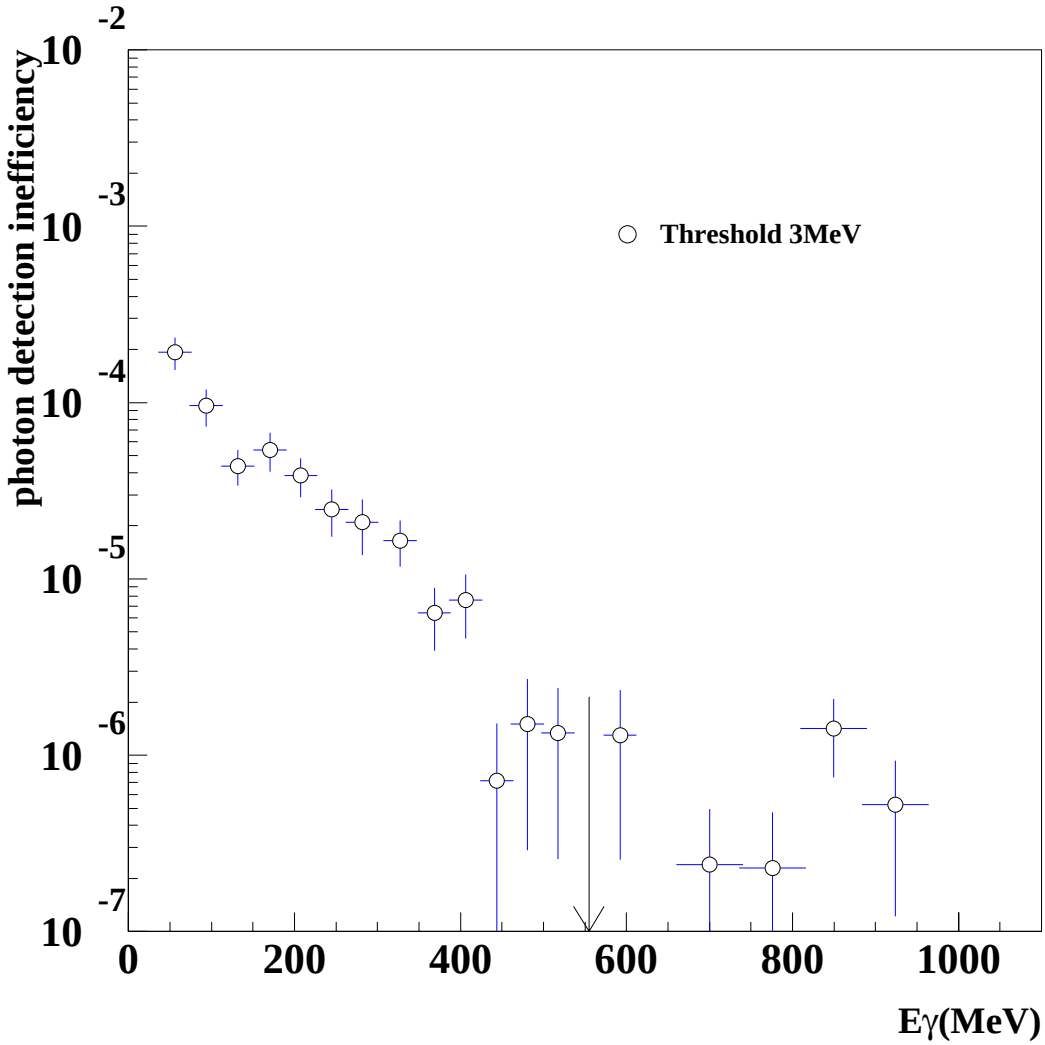

Figure 59: The detection inefficiency due to photonuclear interaction for the 1mm-Pb/3mm-Scinti calorimeter with the principle of the recommendation 1 for the 3 MeV threshold. The arrow indicates the upper limit at the 90% confidence level.

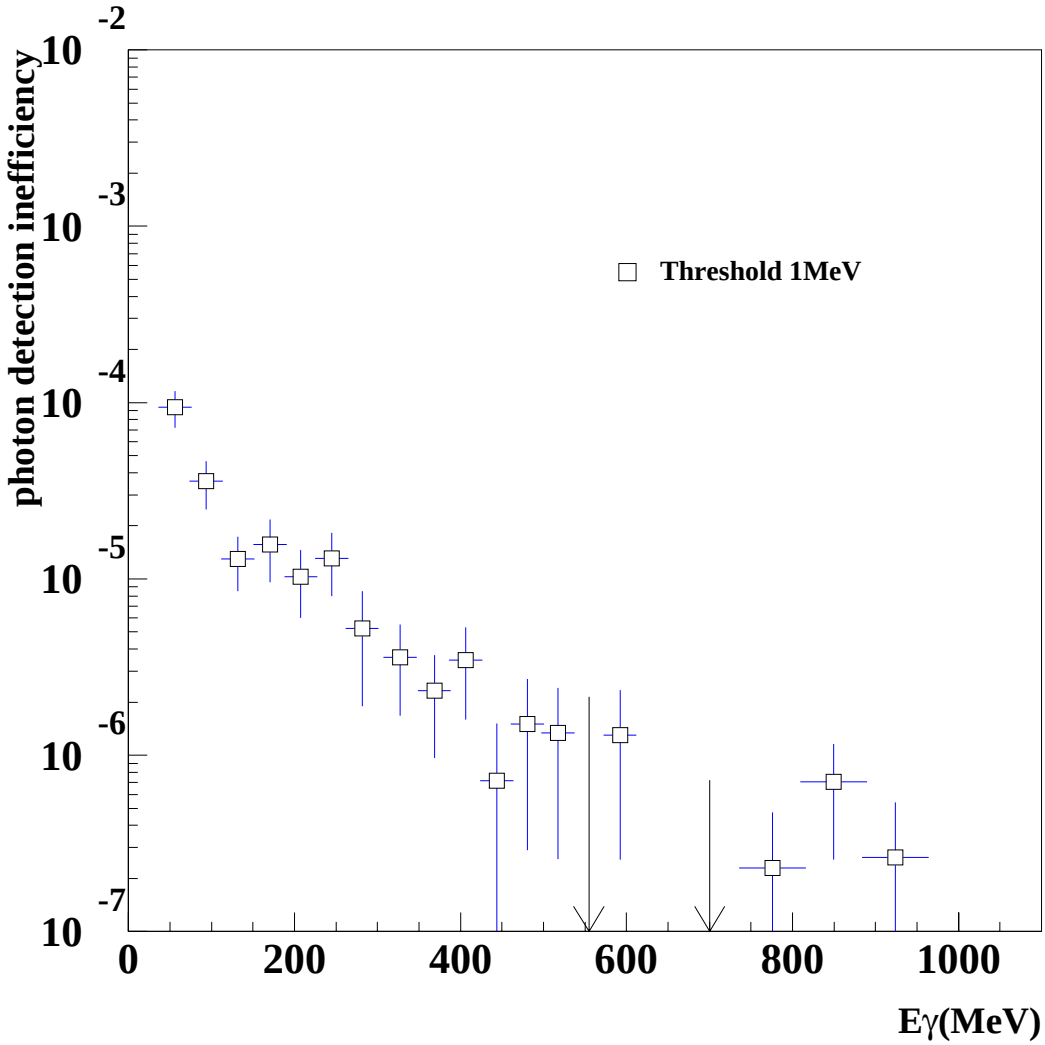

Figure 60: The detection inefficiency due to photonuclear interaction for the 1mm-Pb/3mm-Scinti calorimeter with the principle of the recommendation 1 for the 1 MeV threshold. The arrow indicates the upper limit at the 90% confidence level.

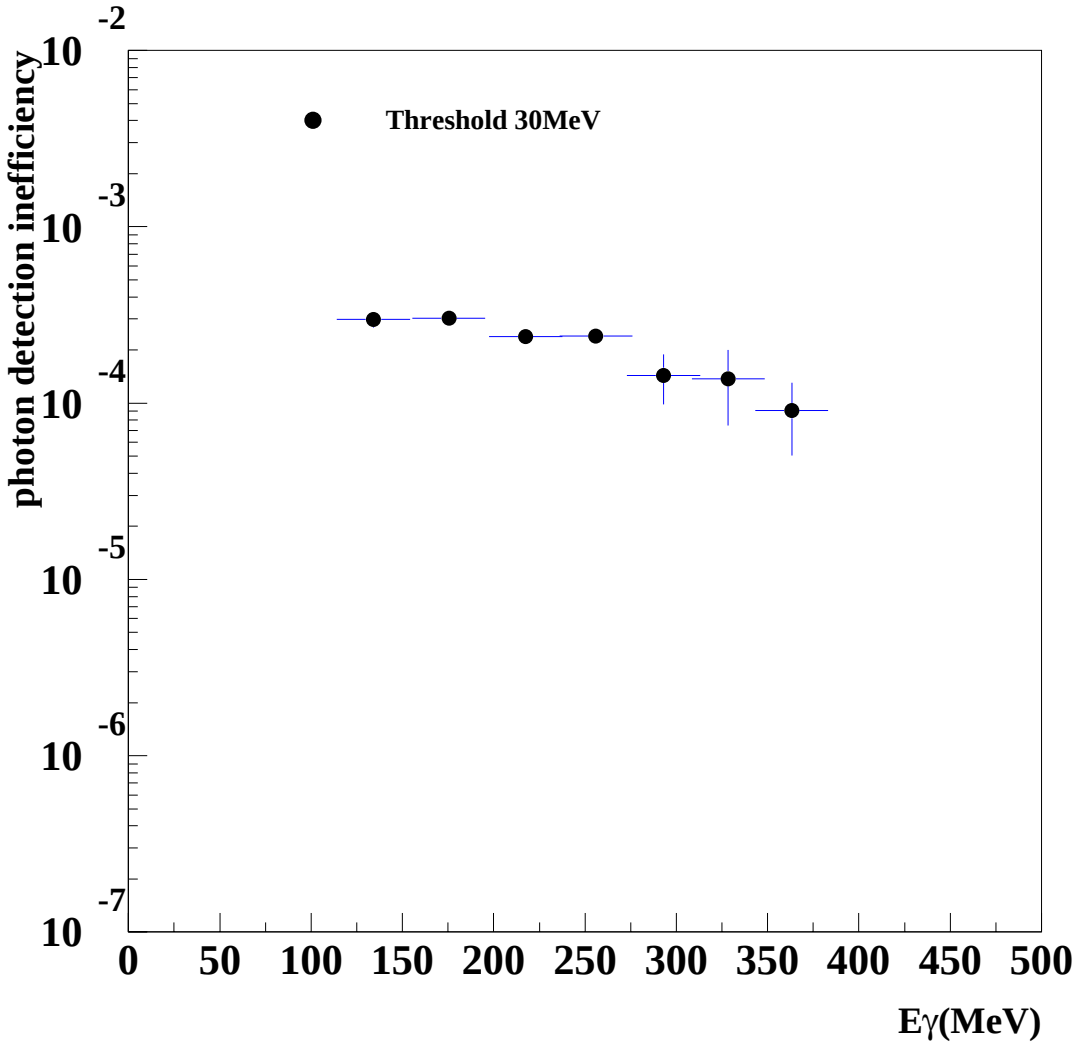

Figure 61: The detection inefficiency due to photonuclear interaction for the KEK-CsI calorimeter with the principle of the recommendation 1 for the 30 MeV threshold.

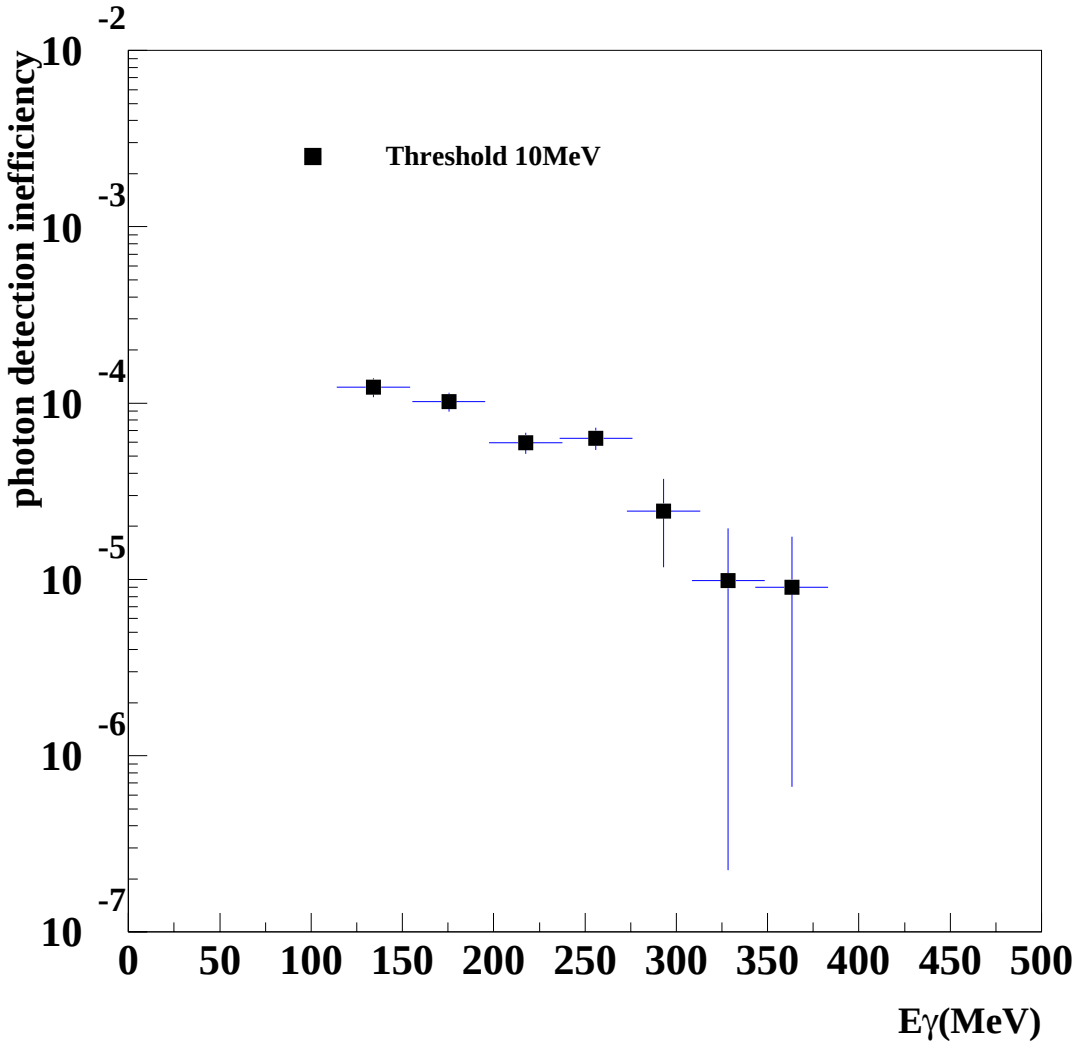

Figure 62: The detection inefficiency due to photonuclear interaction for the KEK-CsI calorimeter with the principle of the recommendation 1 for the 10 MeV threshold.

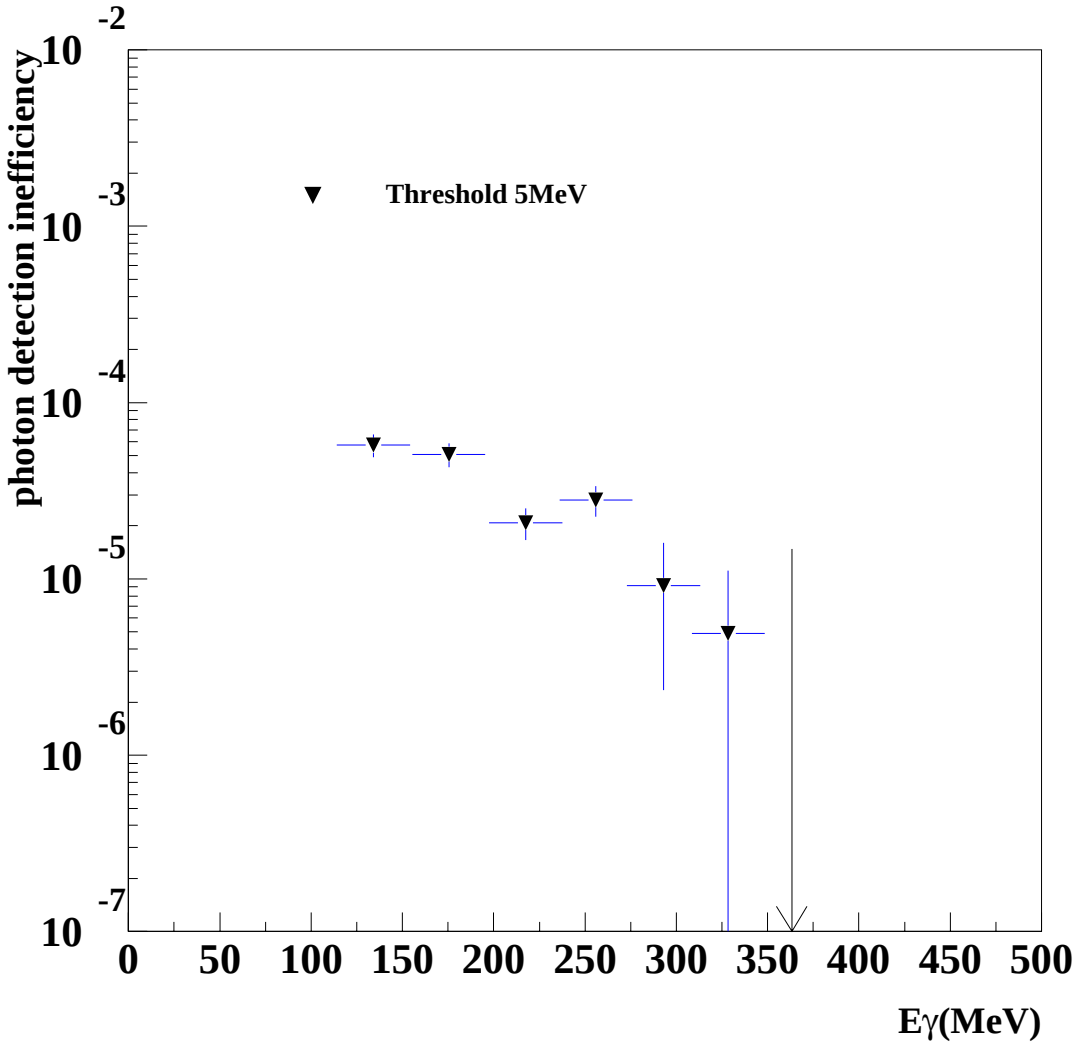

Figure 63: The detection inefficiency due to photonuclear interaction for the KEK-CsI calorimeter with the principle of the recommendation 1 for the 5 MeV threshold. The arrow indicates the upper limit at the 90% confidence level.

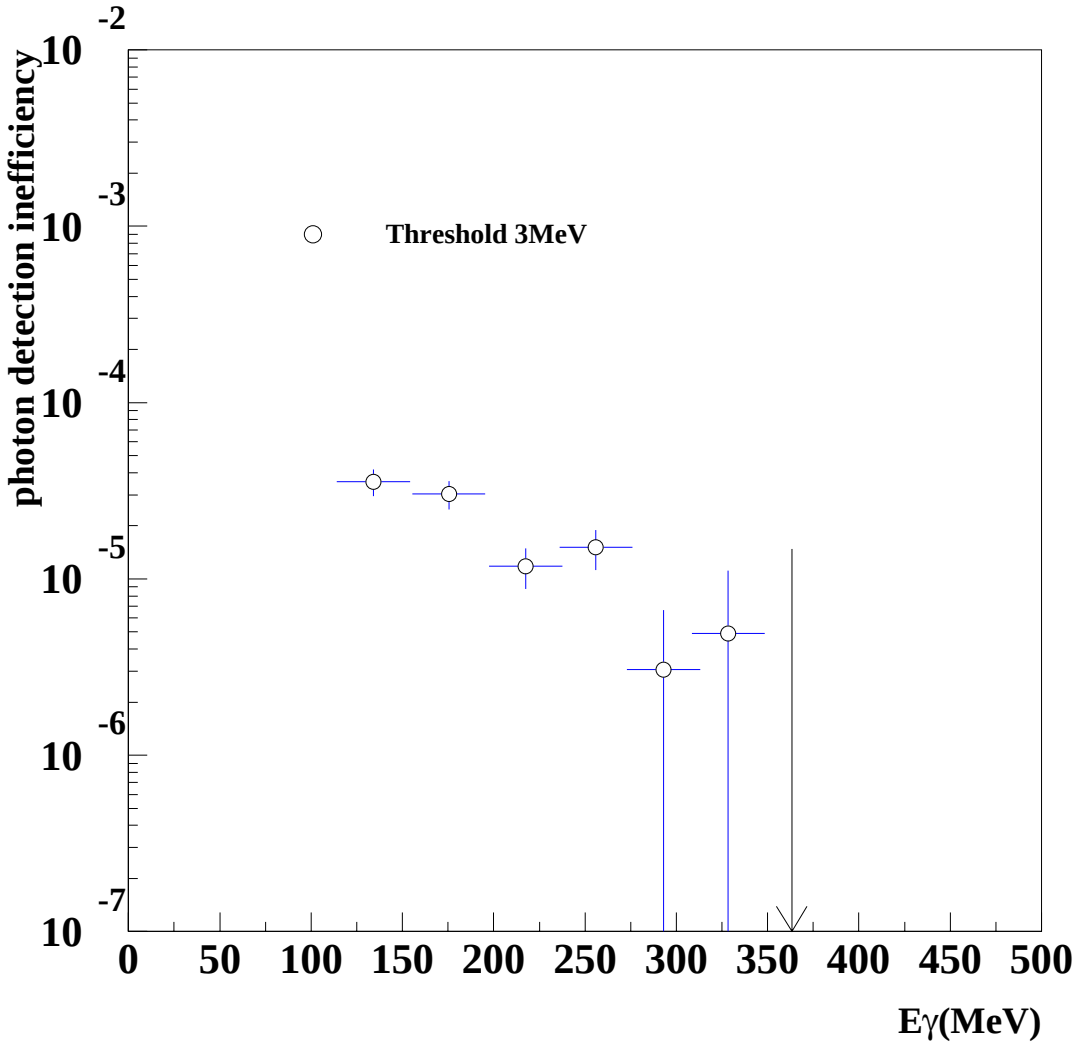

Figure 64: The detection inefficiency due to photonuclear interaction for the KEK-CsI calorimeter with the principle of the recommendation 1 for the 3 MeV threshold. The arrow indicates the upper limit at the 90% confidence level.

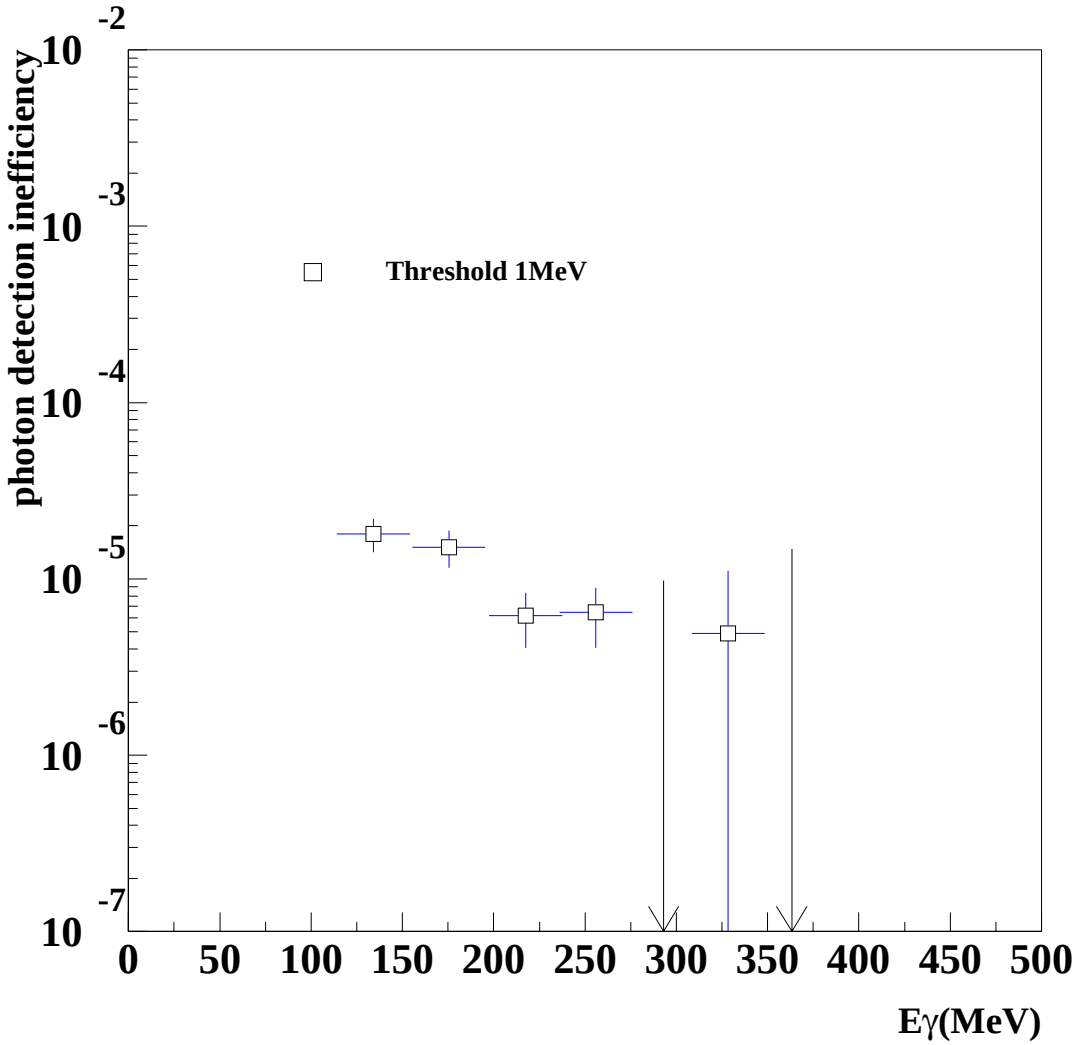

Figure 65: The detection inefficiency due to photonuclear interaction for the KEK-CsI calorimeter with the principle of the recommendation 1 for the 1 MeV threshold. The arrow indicates the upper limit at the 90% confidence level.